The Dissertation Committee for Alexey Vladimirovich Arefiev
certifies that this is the approved version of the following dissertation:

Theoretical Studies of the VASIMR Plasma Propulsion Concept

Committee:

Roger Bengtson, Supervisor

Boris Breizman

Richard Hazeltine

Wendell Horton

Paul Shapiro

Theoretical Studies
of the VASIMR
Plasma Propulsion Concept

by

Alexey Vladimirovich Arefiev, B.S.

DISSERTATION

Presented to the Faculty of the Graduate School of

The University of Texas at Austin

in Partial Fulfillment

of the Requirements

for the Degree of

DOCTOR OF PHILOSOPHY

THE UNIVERSITY OF TEXAS AT AUSTIN

August 2002

Acknowledgments

This work would not have been possible without the guidance and initiative of my supervisor and mentor, Dr. Boris Breizman. His passion and dedication to the science of physics have been inspirational, and a compass in the sometimes disorientating world of theoretical physics. Likewise, I am indebted to Dr. Roger Bengtson for his insight and mastery of the experimental aspects involved in helicon plasma sources, and the actual working of the VASIMR device. For this, I must also thank my colleagues Jason Gibson and Martin Panevsky. They have enriched my understanding of VASIMR and have been a source of stimulating conversations during our weekly project meetings. Much credit must go to Dr. Franklin Chang-Diaz who envisioned the VASIMR concept and now directs the research team at ASPL and guides the collaborating efforts of academic institutions and National Laboratories involved with the project. This research has also been aided by Dr. Andrew Ilin (ASPL) and Dr. Mark Carter (ORNL). I am thankful for their input concerning the numerical modelling of helicon plasma sources and ICRH. I thank Dr. Jarred Squire for providing us with experimental data from the VX-10 helicon plasma source. This acknowledgement section is certainly not exhaustive, as there are many other people without whom this work would not be possible. Lest I forget to mention such a person, I shall simply thank the whole ASPL, IFS, and FRC team for making my three and a half years here at the University of Texas at Austin so enjoyable and academically nurturing. Finally, I owe a great deal to my wife Katharine, my parents Vladimir and Valentina, and my sister Maria. Their encouragement and unrelenting support have made my path much easier to tread. Thank you.

Theoretical Studies
of the VASIMR
Plasma Propulsion Concept

Publication No. ________________

Alexey Vladimirovich Arefiev, Ph.D.
The University of Texas at Austin, 2002

Supervisor: Roger Bengtson

This dissertation was motivated by the Variable Specific Impulse Magnetoplasma Rocket (VASIMR) project. The VASIMR device has a magnetic mirror configuration and consists of three main components: a low energy helicon plasma source, which creates cold plasma via rf-discharge; an ion cyclotron-resonance heating (ICRH) section, which is used to deposit rf-power into the plasma; and a magnetic nozzle, which forms highly directed superalfvenic outgoing plasma flow. The dissertation is focused on fundamental physics issues of the helicon source operation and ICRH.

A first-principle theory for helicon sources with a self-consistent treatment of the particle balance, power balance, and rf-field structure has been developed. The problem of particle balance reduces to kinetic ion transport under the effect of the ambipolar electric field and ion-neutral collisions. Power balance involves electron heating by rf-field, heat conduction, and radiation. The rf-power deposition is associated with the excitation of radially localized helicon modes by an external antenna. The radial density gradient in a plasma forms a potential well for the modes, with the resulting mode frequency being significantly lower than that for a uniform plasma.

This explains the high efficiency of the source at low frequencies. The three key physics ingredients have been combined into a 1D numerical model for a source with predominantly radial flow. The code calculates the evolution of the plasma density, electron temperature, and the rf-fields. These calculations specify the parameter range for a stable steady-state operation of the helicon discharge.

The ICRH concept in VASIMR has two distinct features: 1) each ion passes the resonance only once and 2) the ion motion is collisionless. The ion response to the rf-field during single-pass ICRH can be essentially nonlinear. A self-consistent nonlinear model for the deposition of rf-power in the ion cyclotron frequency range into a steady-state plasma flow has been developed. The one-dimensional fluid-type simulations confirm the theoretical picture of the near-resonance behavior and wave energy conversion into the energy of the directed ion flow.

The regimes relevant to the VASIMR experiment are discussed and issues such as the transition of plasma profiles and the increase in gas pressure due to plasma production observed in the experiment are addressed.

Table of Contents

List of Figures

Chapter 1

Introduction

This work has been motivated by the Variable Specific Impulse Magnetoplasma Rocket (VASIMR) project [1–3], one of the prospective plasma-based space propulsion systems [4]. The VASIMR concept originated in the early 1980's and in 1995 Dr. Franklin Chang-Diaz established the Advanced Space Propulsion Laboratory (ASPL) at NASA Johnson Space Center in order to develop a working prototype of the thruster. A research group at the University of Texas at Austin headed by Dr. Roger Bengtson and Dr. Boris Breizman is currently working in collaboration with the VASIMR development team in an attempt to understand the fundamental plasma physics phenomena involved.

As mankind prepares to take another step in human space exploration — a manned mission to Mars, the question arises as to what technology is needed to make such a mission possible. A human interplanetary spaceship must be *fast* and it should have reasonable *abort options* for crew safety. The travel time must be minimized in order to reduce the crew's exposure to radiation and weightlessness. These requirements can be met by using a propulsion system with a *continuous thrust.*

A conventional chemical rocket accelerates in a short burst in the beginning of the journey and then it follows a ballistic trajectory to the point of final destination. In contrast with this, a spacecraft with a continuous thrust would spend roughly half of the travel time accelerating and the other half slowing down. Such a spacecraft is not constrained to a ballistic trajectory, so that its trajectory can be optimized in order to decrease the travel time. It is essential that continuous thrust gives the option of aborting the mission and returning back from early in the cruise.

It is generally desirable to have a thruster with *low propellant consumption* in order to cut down on propellant weight and increase useful payload. It follows directly from the momentum conservation law that a rocket ejecting propellant of mass m with exhaust velocity (relative to the rocket) u gains momentum mu. Therefore, by increasing the exhaust velocity, a propulsion system can be made more propellant-efficient without sacrificing the momentum gain. In a chemical rocket, the exhaust velocity is related to the combustion temperature, which is typically around half an electron volt. The combustion temperature cannot be significantly increased because it is limited by the energy stored in the chemical bonds of the reactants, which does not exceed few electron volts. A significant increase in the exhaust velocity would require at least 10 eV per particle. At these energies ionization occurs, so that one has to consider *plasma as a propellant*.

The most favorable energy range per particle for *plasma-based propulsion systems* is probably in a range of hundreds of electron volts. Plasma production alone requires roughly 30 eV per ion, which is higher than the ionization potential because the ionization is accompanied by excitation and line radiation that introduces additional energy losses. Clearly, the energy of the ions in the exhaust should be significantly above 30 eV, since only in this case the major part of the energy will go into ion acceleration rather than into plasma production.

Plasma-based propulsion systems provide not only continuous thrust, but they also allow one to vary the exhaust velocity. A system with a variable velocity (variable specific impulse) can handle both the cruise phase of the journey and the maneuvering near the origin and destination planets [3]. This characteristic makes plasma-based systems even more attractive.

It is important to point out that low propellant consumption of plasma-based

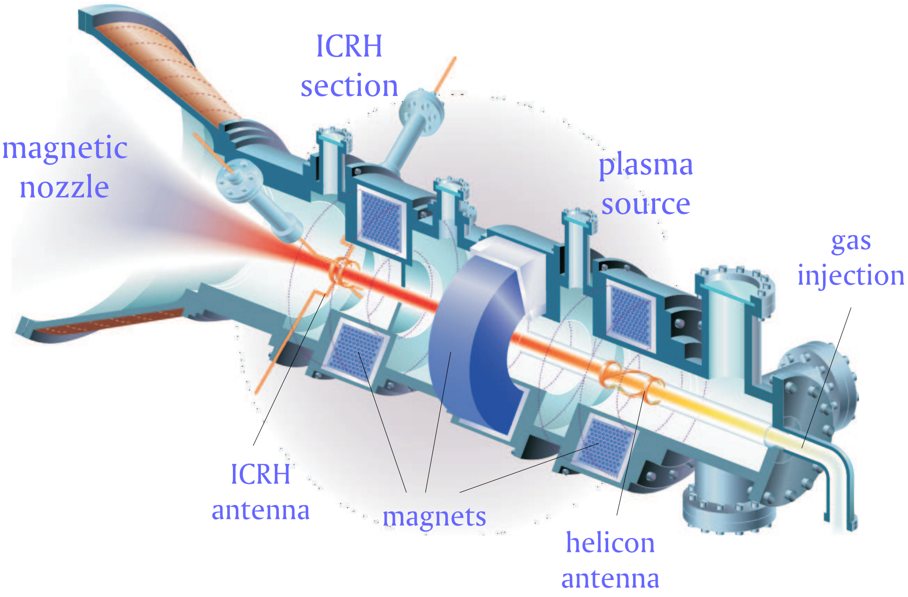

Figure 1.1: The schematic layout of VASIMR.

systems leads to their high energy consumption. An energy source that can release more than a hundred electron volts per fuel particle is needed. Otherwise, the mass of the energy source alone is going to be higher than the propellant mass. The only way to release this amount of energy is through a nuclear reaction. For this reason, a nuclear reactor would be a relevant energy source for plasma-based thrusters.

NASA is currently investigating several new plasma-based propulsion concepts offering a continuous thrust and high propellant efficiency. A distinctive feature of VASIMR is that it employs radio frequency electromagnetic waves to deliver power to the propellant. Electrodes are not used in VASIMR for plasma production or ion acceleration, so that the thruster lifetime is not limited by electrode erosion that affects other electric propulsion systems.

The schematic layout of VASIMR and its magnetic configuration are shown in Figs. 1.1 and 1.2 respectively. The device consists of three main components: the low energy plasma source, ion cyclotron-resonance heating (ICRH) section, and magnetic nozzle. The helicon source creates a cold plasma ionizing the injected gas via rf-discharge. This plasma then flows along the field lines, down the magnetic field gradient, towards the ICRH section. The VASIMR concept employs ICRH as the mechanism for rf-power deposition in the plasma. In the ICRH section, the ion gyro-frequency ω_{ci} matches the ICRH antenna frequency ω to ensure wave energy conversion into the ion gyro-motion. Following the magnetic field lines, the ions leave the ICRH section and enter the magnetic nozzle. At the nozzle entrance, the energy stored in the ion gyro-motion ($K_\perp = m_i v_\perp^2/2$) significantly exceeds the energy of the ion motion along the field lines $\left(K_\parallel = m_i v_\parallel^2/2\right)$. The magnetic field lines in the nozzle gradually diverge, so that the magnetic field B decreases along the field lines. Since the ion magnetic moment $\mu = m_i v_\perp^2/2B$ and total ion kinetic energy $K_i = K_\parallel + K_\perp$ are conserved, the nozzle transforms the ion rotational motion into the longitudinal motion (see Fig. 1.2). In addition to the energy conversion, magnetic nozzle must ensure plasma detachment from the rocket. The detachment occurs when the energy density of the magnetic field ($B^2/8\pi$) drops below the kinetic energy density of the plasma flow ($n_i K_\parallel$). Then the plasma breaks free, carrying a small amount of the field. This regime can be achieved in the magnetic nozzle with straight divergent field lines. Indeed, it follows from the conservation of the magnetic flux that the magnetic field scales as $1/S$, where S is the nozzle cross section. Ion flux conservation requires that $n_i v_\parallel S$ stays constant. Also, $v_\parallel$ is constant when the ion energy is mostly in the parallel motion. Therefore, the kinetic energy density of the plasma flow ($n_i K_\parallel$) decreases as $1/S$, while the energy density of the magnetic field ($B^2/8\pi$) decreases as $1/S^2$ and thus eventually becomes smaller than $n_i K_\parallel$.

The VASIMR concept is still on a very early stage of its development. There is a wide range of engineering, experimental, and theoretical issues that are yet to be understood. Working as a part of the group based at the University of Texas at Austin, I focused my research on the theoretical plasma physics aspects of the VASIMR concept. I joined the project in January of 1999 when the theoretical re-

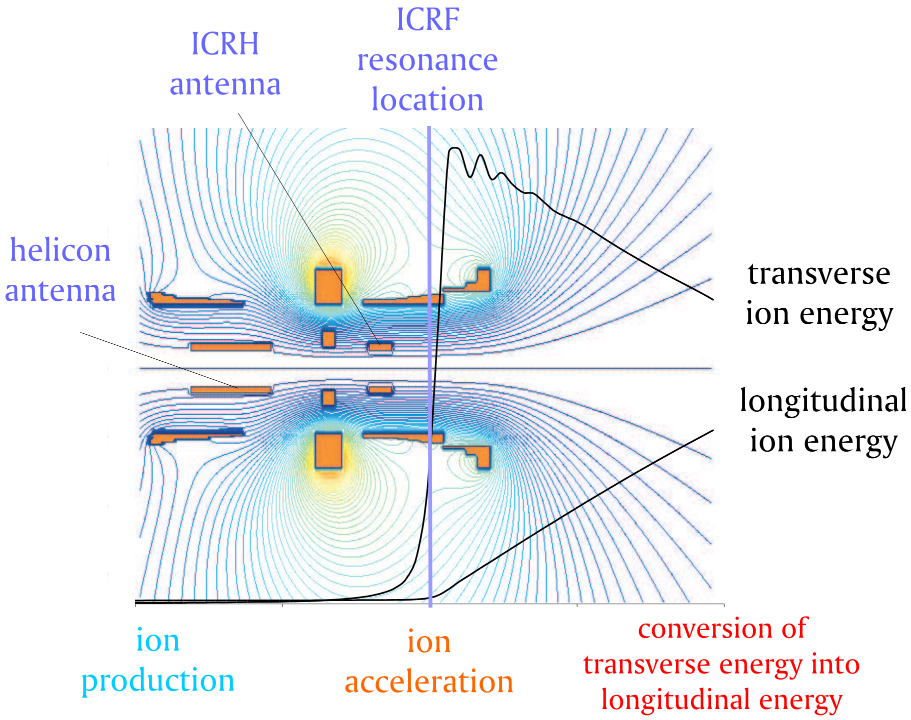

Figure 1.2: The schematic magnetic field configuration in VASIMR together with plots of ion energy stored in transverse motion (gyro-motion) and longitudinal motion. The ion energy plots demonstrate the ion-cyclotron resonant heating and the subsequent transformation of the ion gyro-motion into their fast motion along the magnetic field lines.

search of the concept had just started. Consequently, the main goal of my research became the development of physics basis of the VASIMR components. In the course of our regular discussions and meetings with VASIMR experimental team, we determined the most crucial physics issues that had to be addressed. An attempt has been made to single out problems of general interest that can have applications beyond VASIMR. The specific problems solved in this work should be ultimately incorporated into an integrated model that describes all elements of VASIMR self-consistently.

The thesis consists of five chapters including the Introduction (Chapter 1) and Summary (Chapter 5). Each of the Chapters 2, 3, and 4 presents a separate stand-alone problem motivated by the VASIMR project.

In Chapter 2, Ion Cyclotron Resonance Heating (ICRH) is discussed in the context of the VASIMR project. A distinctive feature of ICRH in VASIMR is that each ion pases the resonance only once, gaining an energy that is much greater than the initial energy. Therefore, the ion response to the rf-field is essentially nonlinear. Chapter 2 presents a self-consistent theory of the rf-wave propagation and ion motion through the resonance. An important ingredient of the problem is the ion flow along the magnetic field. The flow velocity limits the time the ions spend at the resonance, which in turn limits the ion energy gain. A feature that makes the problem nonlinear is that the flow accelerates under the effect of the ∇B force and rf-pressure. This acceleration is shown to produce a steep decrease in the plasma density at the resonance, resulting in partial reflection of the incident wave.

In Chapters 3 and 4, the focus is on the physics of the helicon plasma sources. In Chapter 3, we discuss radially localized helicon modes in nonuniform plasma. It may be possible to explain the high efficiency of the helicon sources at unusually low frequencies with the help of these modes. Chapter 4 presents a self-consistent model of a helicon plasma source working on light gases, such as He and H.

Helicon waves (or whistlers) are widely known for their important role in magnetized plasmas, ranging from space plasma to rf-discharges used in plasma processing [24–26]. A remarkably high efficiency of helicon plasma sources [5, 6] has motivated further theoretical studies of these waves in recent years [9, 17, 27, 28]. Other strong motivations for studying helicon waves include magnetized plasma opening switches, intense-beam plasma interactions, and ionospheric research. One might therefore expect the theory of helicon waves, especially the linear theory, to have been developed in great detail, which is largely true. Still, there appears to be room for new observations in this well-established area. One such observation is discussed in Chapter 3. It turns out that the radial nonuniformity of the plasma has a surprisingly strong effect on the structure of the helicon modes with nonzero values of the azimuthal mode number m. As a result, the corresponding mode frequency is significantly lower than what one would expect from the dispersion relation for a uniform plasma.

Chapter 4 presents a first-principle theory for helicon sources with a self-consistent treatment of the particle balance, power balance, and rf-field structure. A separation of scales among the particle confinement time, the energy confinement time, and the wave period allows us to first consider all three constituents separately and then combine them into an integrated self-consistent description.

The problem of the particle balance reduces to kinetic ion transport. In light gases, the ion motion is controlled by the ambipolar electric field, ion-atom collisions, and equilibrium magnetic field. We derive a corresponding ion distribution function and find the dependence of the radial and longitudinal plasma fluxes on plasma parameters. We calculate plasma density profiles under the assumption that the electron temperature is constant throughout the discharge. This allows us to find the amount of gas, in case of longitudinal plasma flow, and the ionization rate, in case of radial plasma flow, necessary for steady-state discharge operation.

The power balance problem involves electron heating by the rf-field and line-radiation. In steady state, the radiation losses balance the rf-field heating establishing the equilibrium electron temperature. We combine the three key physics ingredients into a theory-based 1D numerical model for a source with predominantly radial ion flow. We assume that the rf-power deposition into the plasma is associated with the excitation of the radially localized helicon modes by the external antenna. The code calculates the evolution of the plasma density profile together with the electron temperature profile, and the rf-fields.

The key results of the thesis were published in Refs. [29–31] and presented at the following conferences: 41st, 42nd, and 43rd Annual Meetings of the Division of Plasma Physics of the American Physical Society [38–42]; 2001 and 2002 Sherwood Fusion Theory Conferences; 1999, 2000, and 2001 VASIMR Workshops organized by

ASPL at NASA Johnson Space Center.

Chapter 2

Single-Pass Ion Cyclotron Resonance Absorption

2.1 Introduction

The Ion Cyclotron Resonance Heating (ICRH) is the mechanism for rf-power deposition into the plasma in VASIMR. The ICRH in VASIMR has two distinct features. First, each ion passes the resonance only once, gaining an energy that is much greater than the initial energy. Second, the ion motion is collisionless, i.e. the energy gain is limited not by collisions but by the time the ion spends at the resonance while moving along the field lines. Therefore, the ion final energy, as well as the rf-power absorption efficiency, should depend on the incident-flow velocity. If the flow is sufficiently fast, its velocity will not change significantly at the resonance. As a result, the ion density will also be nearly constant throughout the resonance. In this regime, ion flux through the resonance turns out to be sufficient to absorb all the rf-power. Technically, the description of the fast flow case is a linear problem. In contrast with the fast incoming flow, the slow flow case is essentially nonlinear. Slow ions can be significantly accelerated along the magnetic field even before they reach their full rotational energy. The driving forces responsible for their acceleration are the ∇B force and rf-pressure. Depending on plasma parameters and incident rf-power, the acceleration distance can either extend over many wavelengths or be as short as a fraction of wavelength. In both limits, the nonlinear problem allows approximate analytical solutions. In the limit of long acceleration distance, our solution involves WKB approximation. In the opposite limit, we exploit the narrowness of the resonance.

There are several important common elements between this work and the earlier studies of the Electron Cyclotron Resonance Heating (ECRH) [18–21]. The technical similarity between the ECRH and ICRH problems is very straightforward in the linear regime. However, this similarity does not fully extend to the nonlinear case. The key reason for the difference is that the ambipolar electric field generally prevents electrons from leaving the system after a single pass through the electron cyclotron resonance. It is therefore rather difficult to implement the single-pass regime in the ECRH problem. In contrast with this, the ICRH problem with a supersonic incident ion flow is intrinsically a single-pass problem. This feature also simplifies the nonlinear treatment of the ICRH case, which allows us to develop a compact self-consistent nonlinear model.

The chapter is organized in the following way. In Sec. 2.2, we introduce a basic set of nonlinear fluid-type equations for the electromagnetic field of a circular polarized wave and the steady-state ion flow through the resonance. In Sec. 2.3, we present a linear theory of wave energy conversion into ion rotational energy. This section is very closely related to the well-known linear magnetic beach problem [22] that exhibits 100% conversion efficiency. An interesting new element of Sec. 2.3 is the WKB-type conversion mechanism. The corresponding solution indicates that this type of conversion can be described as a propagation of a properly chosen WKB mode in an inhomogeneous medium without any mode coupling effects. In Sec. 2.4, we analyze the nonlinear regimes of ion-cyclotron absorption. We find that the absorption efficiency is still 100%, as long as the WKB approximation is applicable. We also describe the nonlinear absorption in the anti-WKB (narrow resonance) limit, in which case we predict a steep density drop at the resonance and substantial reflection of the rf-power. In Sec. 2.5, we present a numerical model that reproduces our analytical results and allows us to quantitatively extend the description to a broader range of parameters. In particular, this model quantifies the effect of nonlinear reflection.

Finally, in Sec. 2.6, we summarize the results.

2.2 Basic Equations Near the Resonance

We consider collisionless plasma with *cold ions* in an equilibrium axisymmetric mirror magnetic field $\mathbf{B}_0 = (B_{0r}; 0; B_{0z})$, where z is the axis of symmetry. We assume that B_{0z} is positive, with $B_{0z} \gg B_{0r}$, and that B_{0z} decreases monotonically along z.

We consider a wave that is launched nearly parallel to the magnetic field lines, so that one can neglect the dependence of the wave fields on the perpendicular coordinates. We will use the term "resonance" to refer to the spatial point where the ion gyro-frequency equals the incident wave frequency ω. This is, to lowest order, the location of the energy conversion layer. The width of the layer is assumed to be small compared to the characteristic scale-length L of the equilibrium magnetic field. We choose the resonance to be at $z = 0$, and we use the following approximation for the ion gyro-frequency $\omega_{ci} = eB_0/m_i c$ near the resonance:

$$\omega_{ci} = \omega(1 - z/L). \tag{2.1}$$

We do not try to resolve a small Doppler correction to the resonance location at this point. However, it should be pointed out that Doppler effect will be properly treated in our analysis. It is represented by the convective term $V_z \partial V_+ / \partial z$ in Eq. (2.21) below.

The electric and magnetic fields of the wave are determined by Maxwell's equations:

$$curl\mathbf{E} = -\frac{1}{c}\frac{\partial \mathbf{B}}{\partial t}, \tag{2.2}$$

$$curl\mathbf{B} = \frac{4\pi}{c}\mathbf{j}, \tag{2.3}$$

where $\mathbf{j}$ is the plasma current. We have neglected the displacement current in

Eq. (2.3), which is justified when

$$\omega_{pi} \gg \omega_{ci}, \tag{2.4}$$

where $\omega_{pi} = \sqrt{4\pi n e^2/m_i}$ is the ion plasma frequency. High electron conductivity eliminates E_z in our problem, which allows us to replace the z-component of Eq. (2.3) by

$$E_z = 0. \tag{2.5}$$

Since the x and y derivatives of the fields are small near the resonance, the transverse components of Maxwell's equations reduce to

$$\frac{\partial E_y}{\partial z} = \frac{1}{c}\frac{\partial B_x}{\partial t}, \qquad \frac{\partial E_x}{\partial z} = -\frac{1}{c}\frac{\partial B_y}{\partial t}, \tag{2.6}$$

$$\frac{\partial B_y}{\partial z} = -\frac{4\pi}{c} j_x, \qquad \frac{\partial B_x}{\partial z} = \frac{4\pi}{c} j_y. \tag{2.7}$$

Here, j_x and j_y are the components of the ion current given by

$$j_x = enV_x \qquad j_y = enV_y, \tag{2.8}$$

where n is the ion density and V_x and V_y are the ion velocity components. The electron current is not included in Eq. (2.7), since its transverse components are smaller than the ion current near the resonance by the factor $|\omega - \omega_{ci}|/\omega_{ci}$.

In order to find V_x and V_y, we use the corresponding components of the ion momentum balance equation together with Eq. (2.1) for ω_{ci}:

$$\frac{\partial V_x}{\partial t} + V_z \frac{\partial V_x}{\partial z} = \frac{eE_x}{m_i} + \omega(1 - z/L)V_y, \tag{2.9}$$

$$\frac{\partial V_y}{\partial t} + V_z \frac{\partial V_y}{\partial z} = \frac{eE_y}{m_i} - \omega(1 - z/L)V_x, \tag{2.10}$$

where V_z is the parallel component of the ion velocity.

We assume a steady-state ion flow through the resonance, so that

$$nV_z = const. \tag{2.11}$$

The quantities n and V_z are time-independent, whereas the transverse components of all vectors oscillate at the wave frequency.

The spatial dependence of V_z is determined by the longitudinal momentum balance equation

$$m_i V_z \frac{\partial V_z}{\partial z} = -m_i \frac{\left\langle V_x^2 + V_y^2 \right\rangle}{2B_{0z}} \frac{\partial B_{0z}}{\partial z} + \frac{e}{c} \left\langle V_x B_y - V_y B_x \right\rangle - m_i \frac{c_s^2}{n} \frac{\partial n}{\partial z}, \tag{2.12}$$

with a convective term on the left-hand side and three longitudinal forces on the right-hand side. The angular brackets in this equation, as well as in the subsequent equations, stand for time averaging over the wave period.

Equation (2.12) is similar to the one discussed in Ref. [18] for the ECRH problem. However, Ref. [18] is limited to the study of particle motion in a given electromagnetic wave, whereas this chapter presents a self-consistent analysis of the wave field and the particle flow.

The three forces in Eq. (2.12) are:

- The ∇B_0-force

$$-\mu \frac{\partial B_{0z}}{\partial z}, \tag{2.13}$$

which is associated with the ion magnetic moment [1] $\mu = m_i \left\langle V_x^2 + V_y^2 \right\rangle / 2B_{0z}$.

- The time averaged Lorentz force from the wave

$$\frac{e}{c} \left\langle (\mathbf{V} \times \mathbf{B})_z \right\rangle = \frac{e}{c} \left\langle V_x B_y - V_y B_x \right\rangle. \tag{2.14}$$

- The force associated with the ambipolar electric field:

$$-m_i \frac{c_s^2}{n} \frac{\partial n}{\partial z}, \tag{2.15}$$

where $c_s = \sqrt{T_e/m_i}$ is the ion acoustic velocity and T_e is the electron temperature.

---

[1] Although the term "magnetic moment" is used in this chapter, the magnetic moment is not assumed to be conserved. Instead, the gain in the magnetic moment is actually calculated as the ion passes the resonance area. This applies to both the linear and the nonlinear analysis.

The time averaging procedure in Eq. (2.12) requires that the ions complete many cycles over their gyro-orbit while they move through the resonance, i.e.

$$\tau_r \omega_{ci} \gg 1, \tag{2.16}$$

where τ_r is the time ion spends in the resonance area.

We limit our consideration to a circular polarized wave that rotates in the "ion" direction. The electric field of this wave has the form:

$$E_x = \frac{1}{2}\left[E_+(z)\mathrm{e}^{-i\omega t} + c.c.\right], \tag{2.17}$$

$$E_y = \frac{1}{2}\left[E_+(z)\mathrm{e}^{-i\omega t - i\pi/2} + c.c.\right], \tag{2.18}$$

where $E_+(z)$ is a complex amplitude. The magnetic field and the ion velocity components also have the form of Eqs. (2.17) and (2.18) with B_+ and V_+ the corresponding amplitudes.

The polarization constraints, given by Eqs. (2.17) and (2.18), allow us to reduce Eqs. (2.6)-(2.12) to a closed set of equations for E_+, B_+, V_+, V_z, and n. The equations read

$$\frac{\partial E_+}{\partial z} = \frac{\omega}{c} B_+, \tag{2.19}$$

$$\frac{\partial B_+}{\partial z} = -\frac{4\pi i}{c} n e V_+, \tag{2.20}$$

$$V_z \frac{\partial V_+}{\partial z} = \frac{e}{m_i} E_+ + i\omega \frac{z}{L} V_+, \tag{2.21}$$

$$j \equiv n V_z = const, \tag{2.22}$$

$$V_z \frac{\partial V_z}{\partial z} = \frac{|V_+|^2}{2L} - \frac{1}{8\pi m_i n}\frac{\partial |B_+|^2}{\partial z} - \frac{c_s^2}{n}\frac{\partial n}{\partial z}. \tag{2.23}$$

The boundary conditions for this set of equations are

$$V_+(-\infty) = 0 \tag{2.24}$$

(absence of the ion gyro motion at $z = -\infty$) and

$$E_+(+\infty) = 0, \qquad B_+(+\infty) = 0 \tag{2.25}$$

(evanescent wave fields downstream).

In addition we must specify the power flux in the incident wave, the incident ion flux, and the ion flow velocity at $z \to -\infty$. It should be noted that the ion flow must be supersonic to justify this formulation of the problem.

The key quantities to be determined from Eqs. (2.19)-(2.23) are the ion energy gain and the reflection coefficient for the wave.

We start our analysis of Eqs. (2.19)-(2.23) from the limiting case of fast incoming flow, which means that V_z and n can be treated as constants in the resonance area. This simplification "linearizes" the problem. The linear analysis (Sec. 2.3) will then be followed by the analysis of slow flow regime (Sec. 2.4) that is essentially nonlinear.

2.3 Linear Theory

The fast flow assumption of nearly constant V_z decouples Eqs. (2.19)-(2.21) from Eqs. (2.22) and (2.23). We can thus combine Eqs. (2.19)-(2.21) into a single linear equation for E_+:

$$i\gamma \frac{\partial^3 E_+}{\partial s^3} + s \frac{\partial^2 E_+}{\partial s^2} - E_+ = 0, \tag{2.26}$$

where

$$s \equiv \frac{L\omega_{pi}^2}{c^2} z, \qquad \gamma \equiv \frac{V_z}{L\omega} \left(\frac{L\omega_{pi}}{c} \right)^4 > 0. \tag{2.27}$$

A similar equation appears in the ECRH problem with a fast electron flow. Naturally, the analysis of Eq. (2.26) is largely similar to that of Ref. [19]. There is, however, a new element in our analysis: the discussion of the WKB-type energy conversion regime (see below).

It should be noted that this equation differs from the "Standard Equation" discussed in Ref. [23]. Unlike the "Standard Equation" which only contains the even derivatives of the field, Eq. (2.26) contains an odd derivative $\partial^3 E_+ / \partial s^3$. This difference in symmetry is due to the directed ion flow along the field lines. The flow is more important in our problem than the ion thermal motion since we assume that the flow is supersonic.

All independent solutions of Eq. (2.26) can be written in the form of a contour integral in the complex k-plane

$$E_+(s) = \int_C E(k) e^{iks} dk, \tag{2.28}$$

where $E(k)$ is the Laplace-image of $E_+(s)$ and contour C has to be specified for each solution. Substitution of Eq. (2.28) into Eq. (2.26) with subsequent integration by parts gives

$$\int_C \left[\gamma k^3 E - i\frac{d}{dk}(k^2 E) - E \right] dk = 0, \tag{2.29}$$

provided that

$$k^2 E e^{iks} \big|_a^b = 0 \tag{2.30}$$

for all real values of s. We use notations a and b for the end points of the contour C. It follows from Eq. (2.29) that

$$E(k) = \frac{E_*}{k^2} e^{-i/k - i\gamma k^2/2}, \tag{2.31}$$

where E_* is an arbitrary constant.

We now use Eqs. (2.19), (2.20), (2.28), and (2.31) to find V_+:

$$V_+ = -i\frac{e}{m_i}\left(\frac{\omega_{pi} L}{c}\right)^2 \frac{E_*}{\omega} \int_C dk e^{\varphi}, \tag{2.32}$$

where

$$\varphi \equiv iks - i/k - i\gamma k^2/2. \tag{2.33}$$

In order to satisfy Eq. (2.30), the end points of the contour C must be either at infinity (in the sectors where the products $\mathrm{Re}(a)\mathrm{Im}(a)$ and $\mathrm{Re}(b)\mathrm{Im}(b)$ are negative), or at the origin. In the latter case, the contour must approach the origin from the

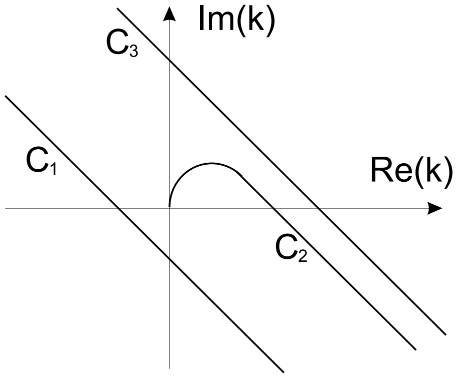

Figure 2.1: Independent contours for Eq. (2.26) in the k-plane.

upper half-plane. The contours that give three independent solutions of Eq. (2.26) are shown in Fig. 2.1.

Of the three contours shown in Fig. 2.1, C_2 is the only one that meets the boundary conditions (2.24) and (2.25). In order to demonstrate this, we will consider the asymptotic behavior of the solution (2.28), (2.31), and (2.32) for $C = C_2$.

In the asymptotic regime, integrals (2.28) and (2.32) can be evaluated by choosing the integration contour C_2 to go through the stationary phase points (saddle points) in which

$$\frac{d\varphi}{dk} = 0, \tag{2.34}$$

or, equivalently,

$$\gamma k^3 - sk^2 - 1 = 0. \tag{2.35}$$

For very large negative values of s, the only accessible saddle point for C_2 is $k_1 = 1/\sqrt{-s}$. The line of the steepest descent crosses the real axis at an angle of $-\pi/4$. The contribution to Eq. (2.28) from this point represents the incident wave propagating towards the resonance:

$$E_+ = E_* \sqrt{\pi}(-s)^{1/4} \mathrm{e}^{-2i\sqrt{-s} - i\pi/4}. \tag{2.36}$$

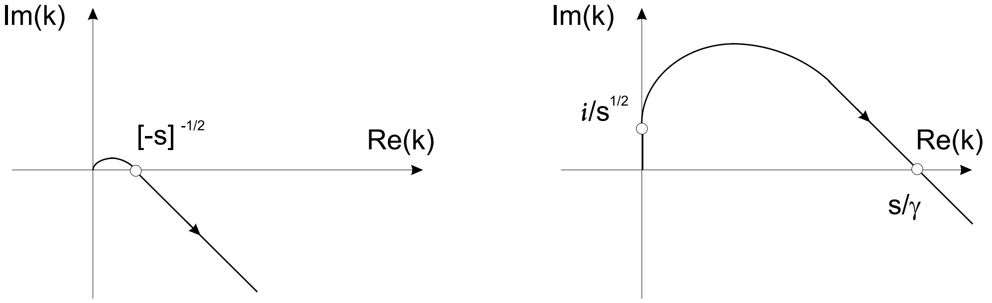

Figure 2.2: Saddle points (open circles) and contour C_2 for $s \to -\infty$ (left) and $s \to \infty$ (right). The contours start at the origin and go to $|k| \to \infty$. The arrows on the contours indicate the direction of the integration.

The corresponding expression for V_+ is

$$V_+ = -i\frac{e}{m_i}\left(\frac{\omega_{pi}L}{c}\right)^2 \frac{\sqrt{\pi}}{(-s)^{3/4}}\frac{E_*}{\omega}\mathrm{e}^{-2i\sqrt{-s}-i\pi/4}. \tag{2.37}$$

Note that $V_+ \to 0$ as $s \to -\infty$, in agreement with the boundary condition given by Eq. (2.24).

For very large positive values of s, the relevant saddle points are $k_2 = s/\gamma$ and $k_3 = i/\sqrt{s}$. The corresponding lines of the steepest descent cross the real axis at angles of $-\pi/4$ and $\pi/2$, respectively (see Fig. 2.2). The contribution from k_2 represents the ion gyro-velocity in the outgoing flow:

$$V_+ = -i\frac{e}{m_i}\left(\frac{\omega_{pi}L}{c}\right)^2 \frac{(2\pi)^{1/2}}{\gamma^{1/2}}\frac{E_*}{\omega}\mathrm{e}^{is^2/2\gamma-i\pi/4}. \tag{2.38}$$

This expression shows that the absolute value of V_+ is independent of s, which means that the particle has already left the resonance. Yet, it has not moved far enough into the low field area to convert its gyro-velocity into parallel velocity. This is consistent with the assumption that the width of the resonance is much smaller than the equilibrium magnetic field scale-length L.

The k_3 saddle point represents the evanescent wave field in the outgoing flow:

$$E_+ = -iE_*\sqrt{\pi}s^{1/4}\mathrm{e}^{-2\sqrt{s}}. \tag{2.39}$$

A remarkable feature of the solution described above is the absence of a reflected wave, which means 100% conversion of the incident rf-wave energy into the ion gyro-motion. The 100% conversion is consistent with the following conservation law

$$\gamma \left| \frac{\partial^2 E_+}{\partial s^2} \right|^2 + i \left(E_+ \frac{\partial E_+^*}{\partial s} - E_+^* \frac{\partial E_+}{\partial s} \right) = const, \tag{2.40}$$

a straightforward consequence of Eq. (2.26). Eqs. (2.19) and (2.20) allow us to rewrite this relationship as the energy flux conservation

$$m_i n V_z \frac{|V_+|^2}{2} + \frac{ic}{8\pi}(E_+ B_+^* - E_+^* B_+) = const, \tag{2.41}$$

where the first term on the left hand side is the energy flux carried by the rotating ions and the second term is the Poynting vector (power carried by the wave).

The outgoing solution (2.38) can be also interpreted as a wave with the dispersion relation $\omega = kV_z + \omega_{ci}$ (ion ballistic mode in the cold beam). However, even a small spread in the ion parallel velocities will eventually smear the short-wavelength spatial modulation in V_+ and thereby destroy the "modulated track" [21]. It is important that, regardless of interpretation, the outgoing energy flux is carried by the rotating ions rather than by the electromagnetic field.

A similar asymptotic analysis of the solutions represented by C_1 and C_3 shows that none of them meets the boundary conditions for our problem. The C_1 solution gives a diverging wave field at $s = +\infty$, and the C_3 solution gives a non-zero ion gyro-velocity at $s = -\infty$.

It should be noted that for large values of γ Eqs. (2.37) and (2.38) can be combined into a WKB-type solution for V_+, which is valid not just asymptotically, but for all s:

$$V_+ = -i \frac{e}{m_i} \left(\frac{\omega_{pi} L}{c} \right)^2 \sqrt{\frac{2\pi}{|\varphi''(k_*)|}} \frac{E_*}{\omega} \mathrm{e}^{\varphi(k_*)} \mathrm{e}^{-i\pi/4}. \tag{2.42}$$

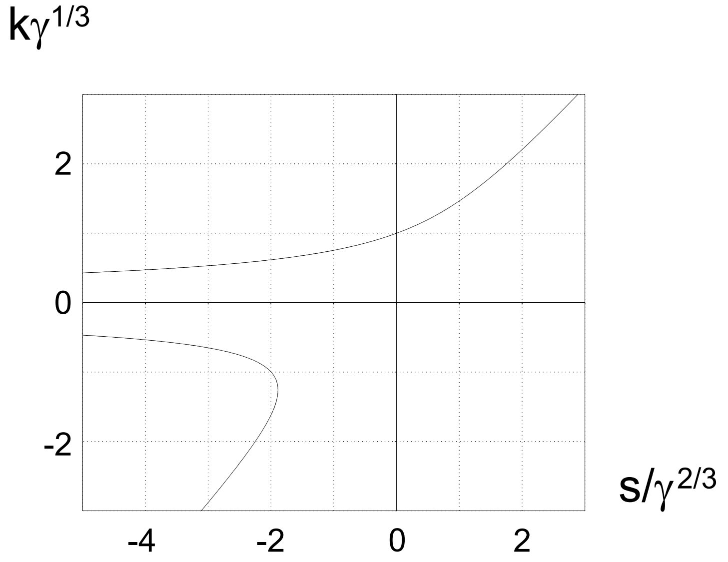

Figure 2.3: Real roots of Eq. (2.35). The upper curve shows $k_*(s)$, the relevant root for the WKB solution given by Eq. (2.42).

Here k_* is the positive real root of the cubic equation (2.35). Indeed, for large values of γ the function e^{φ} on the steepest descent line is localized in a close vicinity of the saddle point k_* regardless of s. This can be seen from the Taylor expansion of $\varphi = i(ks - 1/k - \gamma k^2/2)$ around the saddle point:

$$\varphi(k) = i(k_* s - 1/k_* - \gamma k_*^2/2) - i\frac{(k-k_*)^2}{2k_*^2}(\gamma k_*^2 + 2/k_*). \tag{2.43}$$

Equation (2.43) allows us to estimate the width of the localization interval $|k - k_*|$ as

$$|k - k_*| \sim k_*(\gamma k_*^2 + 2/k_*)^{-1/2} < k_*/\gamma^{1/6} \ll k_*. \tag{2.44}$$

Figure 2.3 shows that k_* increases continuously from 0 to $+\infty$ as s goes from $-\infty$ to $+\infty$. The existence of the global WKB-type solution (2.42) for large values of γ reflects the fact that the incident wave energy flux transforms into the energy flux of the rotating ions over many wave-lengths.

In order to estimate the spatial width of the transformation interval, δ, we use the condition that the energy flux transformation takes place in the area where the wave group-velocity is comparable to the ion flow velocity. An equivalent requirement is that all three terms on the left hand side of Eq. (2.35) are of the same order of magnitude. This requirement gives

$$\delta = \frac{c^2}{L\omega_{pi}^2}\gamma^{2/3}, \qquad \gamma \gg 1. \tag{2.45}$$

In the limiting case of $\gamma \ll 1$ (slow incoming ions), the width of the transformation interval becomes much smaller than the scale-length of the wave electric field near the resonance. The corresponding estimate for δ follows from the condition that the convective term on the left hand side of Eq. (2.21) is comparable to the second term on the right hand side. The result is

$$\delta = \frac{c^2}{L\omega_{pi}^2}\gamma^{1/2}, \qquad \gamma \ll 1. \tag{2.46}$$

It is convenient to combine Eqs. (2.45) and (2.46) into the following interpolation formula for δ:

$$\delta = \frac{c^2}{L\omega_{pi}^2}\left(\gamma^{2/3} + \gamma^{1/2}\right). \tag{2.47}$$

To conclude this section, we formulate the applicability condition for the linear theory. The constraint comes from the requirement that the relative change of the flow velocity, $\Delta V_z/V_z$, is small within the flux transformation interval. Equation (2.23) allows us to estimate $\Delta V_z/V_z$ as

$$\frac{\Delta V_z}{V_z} \sim \frac{\delta}{V_z^2}\frac{V_+^2}{L} \sim \frac{\delta}{V_z^3}\frac{P}{m_i n L}, \tag{2.48}$$

where

$$P = \frac{c^2|E_*|^2}{4\omega L}\left[\frac{\omega_{pi}L}{c}\right]^2 \tag{2.49}$$

is the incident power flux. Here we take into account that

$$nV_z\frac{m_i V_+^2}{2} \sim P \tag{2.50}$$

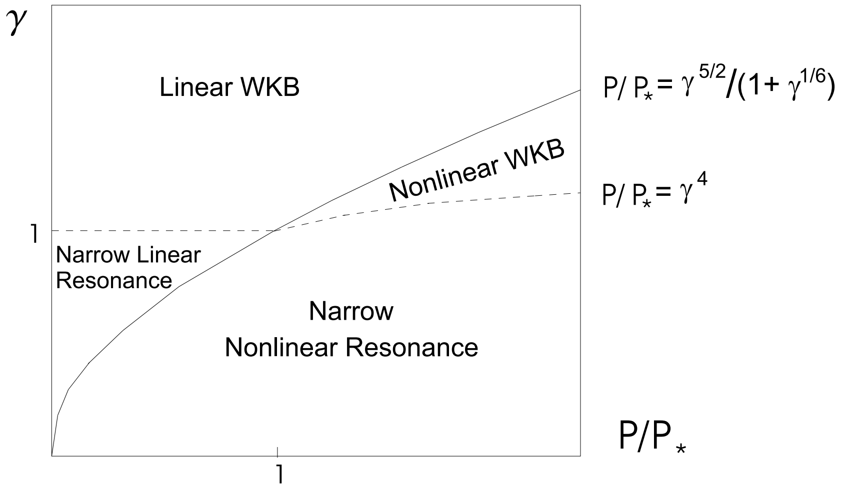

Figure 2.4: Map of absorption regimes in the (γ, P) plane. Solid curve marks the border between linear and nonlinear regimes. Dashed curve shows the applicability boundary for WKB-description. The Narrow Nonlinear Resonance area corresponds to significant reflection of the incident wave.

in the transformation area. It is easy to verify that the contribution from the $|B_+|^2$-term on the right hand side of Eq. (2.23) does not affect our estimate for $\Delta V_z/V_z$. The contribution from the c_s^2-term is insignificant as well, since we are only interested in the supersonic flow. We finally use Eq. (2.47) for δ and the relationship between V_z and γ, Eq. (2.27), to write the condition $\Delta V_z/V_z \ll 1$ in the form

$$P \ll P_* \frac{\gamma^{5/2}}{1+\gamma^{1/6}}, \tag{2.51}$$

where P_* is defined as

$$P_* \equiv m_i n c^3 \left(\frac{L\omega}{c}\right)^3 \left(\frac{c}{L\omega_{pi}}\right)^{10}. \tag{2.52}$$

Equation (2.51) gives the boundary between the linear and nonlinear regimes in the $(\gamma; P)$ plane. This boundary is shown in Fig. 2.4 by the solid curve with the linear regime above the curve and nonlinear regime below.

2.4 Nonlinear Resonance

We will start this section by generalizing the WKB solution to the nonlinear case. The idea behind this generalization is that the WKB approximation remains accurate at the boundary where the linear theory breaks down, provided that $P > P_*$. Therefore, for $P > P_*$, the WKB approach can be extended somewhat below the solid line in Fig.2.4. We will show that the corresponding area is bounded from below by the condition

$$P \ll P_* \gamma^4 \tag{2.53}$$

as indicated by the dashed curve in Fig. 2.4.

2.4.1 Nonlinear WKB Solution

In the WKB-solution, the quantities E_+, B_+, and V_+ are characterized by a fast exponential dependence on z

$$\mathrm{e}^{i \int^z k(\tilde{z}) d\tilde{z}}, \tag{2.54}$$

where k is a local wave number that is real for all z in our solution. We then seek V_+ in the form

$$V_+ = V(z) \mathrm{e}^{i \int^z k(\tilde{z}) d\tilde{z}}, \tag{2.55}$$

where $V(z)$ is a slowly varying amplitude.

We now use Eqs. (2.19) and (2.20) to lowest order to find

$$E_+ = i \frac{4\pi n e \omega}{k^2 c^2} V_+, \qquad B_+ = -\frac{4\pi n e}{kc} V_+, \tag{2.56}$$

and we substitute E_+ into Eq. (2.21) to obtain the local dispersion relation

$$k V_z = \frac{\omega \omega_{pi}^2}{k^2 c^2} + \omega \frac{z}{L}. \tag{2.57}$$

Next, we write down the energy balance equation (conservation of the energy flux), an exact consequence of Eqs. (2.19)-(2.22):

$$n V_z \frac{m_i |V|^2}{2} + \frac{ic}{8\pi} \left(E_+ B_+^* - E_+^* B_+ \right) = P = const. \tag{2.58}$$

We use this equation together with Eq. (2.56) to find $|V|^2$:

$$|V|^2 = P\frac{4\pi e^2}{m_i^2}\left[\frac{\omega_{pi}^2 V_z}{2} + \frac{\omega\omega_{pi}^4}{k^3c^2}\right]^{-1}. \tag{2.59}$$

When combined with the condition $V_z = const$, Eqs. (2.55)-(2.57) and (2.59) reproduce the WKB solution for the linear problem discussed in Sec. 2.3.

The difference between the nonlinear and the linear WKB-problems is that V_z and n are not constant anymore in the nonlinear case. The condition $V_z = const$ should now be replaced by the longitudinal momentum balance equation, Eq. (2.23), that reduces to

$$\frac{\partial}{\partial z}\left[\omega_{pi}^2 V_z^2 + \frac{\omega_{pi}^4}{2k^2c^2}|V|^2\right] = \omega_{pi}^2\frac{|V|^2}{2L}. \tag{2.60}$$

As before, we have neglected the c_s^2-term in this equation, as we assume the flow to be supersonic.

It follows from Eq. (2.57) that

$$1/L = \frac{\partial}{\partial z}\left[\frac{kV_z}{\omega} - \frac{\omega_{pi}^2}{k^2c^2}\right], \tag{2.61}$$

which allows us to rewrite Eq. (2.60) in the form

$$\frac{\partial}{\partial z}\left[\omega_{pi}^2 V_z^2 + \frac{\omega_{pi}^4}{2k^2c^2}|V|^2\right] = \omega_{pi}^2\frac{|V|^2}{2}\frac{\partial}{\partial z}\left[\frac{kV_z}{\omega} - \frac{\omega_{pi}^2}{k^2c^2}\right]. \tag{2.62}$$

A rescaling transformation from k, V_z, and z to new (dimensionless) variables $\tilde{k}$, $\tilde{V}_z$, and $\tilde{z}$ allows us to rewrite Eqs. (2.57) and (2.62) as follows:

$$\tilde{z} = \frac{\tilde{k}^3\tilde{V}_z^2 - 1}{\tilde{k}^2\tilde{V}_z}, \tag{2.63}$$

$$\frac{d\tilde{V}_z}{d\tilde{k}} = \tilde{V}_z\frac{\tilde{k}^6\tilde{V}_z^4 + 6\tilde{k}^3\tilde{V}_z^2 + 2}{2\tilde{V}_z(\tilde{k}^3\tilde{V}_z^2 + 2)^2 - \tilde{k}(\tilde{k}^6\tilde{V}_z^4 + 5\tilde{k}^3\tilde{V}_z^2 + 2)}. \tag{2.64}$$

Here

$$\tilde{k} = \frac{ck}{\omega}\left[\frac{m_i c\omega^2}{\pi e^2 j}\right]^{3/5}\left[\frac{\pi e^2 P}{m_i^2 c^3\omega^2}\right]^{2/5}, \tag{2.65}$$

$$\tilde{V}_z = \frac{V_z}{2c}\left[\frac{\pi e^2 j}{m_i c\omega^2}\right]^{2/5}\left[\frac{m_i^2 c^3\omega^2}{\pi e^2 P}\right]^{3/5}, \tag{2.66}$$

$$\tilde{z} = \frac{z}{2L}\left[\frac{m_i c\omega^2}{\pi e^2 j}\right]^{1/5}\left[\frac{m_i^2 c^3\omega^2}{\pi e^2 P}\right]^{1/5}. \tag{2.67}$$

The applicability condition for the WKB solution is

$$\frac{1}{k^2}\frac{dk}{dz} \ll 1. \tag{2.68}$$

In dimensionless variables, we have

$$\frac{c}{2\omega L}\left[\frac{\pi e^2 P}{m_i^2 c^3\omega^2}\right]^{1/5}\left[\frac{m_i c\omega^2}{\pi e^2 j}\right]^{4/5}\frac{1}{\tilde{k}^2}\frac{d\tilde{k}}{d\tilde{z}} \ll 1. \tag{2.69}$$

Since $\tilde{k}$ and $d\tilde{k}/d\tilde{z}$ are quantities of order unity at the transformation point, this constraint reduces to

$$\frac{c}{2\omega L}\left[\frac{\pi e^2 P}{m_i^2 c^3\omega^2}\right]^{1/5}\left[\frac{m_i c\omega^2}{\pi e^2 j}\right]^{4/5} \ll 1, \tag{2.70}$$

which is equivalent to Eq. (2.53).

Numerical solutions of Eqs. (2.63) and (2.64) for three different values of initial flow velocity are shown in Fig. 2.5. We find that $\tilde{V}_z$ and $\tilde{k}$ are monotonically increasing functions of $\tilde{z}$. Their asymptotic behavior for $\tilde{z} \to +\infty$ is given by

$$\tilde{k} = \tilde{V}_z = \sqrt{\tilde{z}}. \tag{2.71}$$

2.4.2 Narrow Nonlinear Resonance

In this subsection, we will consider the non-linear regime lying below the dashed curve in Fig. 2.4. We have shown that the dashed curve is where the WKB-approximation breaks down. One can thus conjecture that the width of the energy transformation layer should be smaller than the scale-length of the wave electric field if P and γ are below the dashed curve. In fact, we have already shown that the resonance is indeed narrow in the linear regime for $\gamma \ll 1$. We now extend the

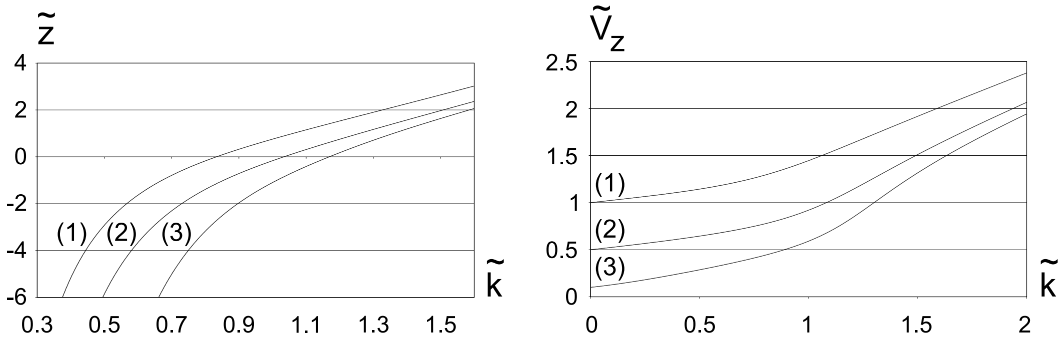

Figure 2.5: Solutions of Eqs. (2.63) and (2.64) for three different values of $\tilde{V}_z$ at $\tilde{z} \to -\infty$: (1) $\tilde{V}_z(-\infty) = 1$; (2) $\tilde{V}_z(-\infty) = 0.5$; (3) $\tilde{V}_z(-\infty) = 0.1$.

narrow-resonance approach to the nonlinear case. In other words, we make a verifiable assumption that the wave electric field is independent of z in the energy transformation layer. It can also be verified that the $|B_+|^2$-term, as well as the c_s^2-term, in Eq. (2.23) is negligibly small in the narrow-resonance case. As a result, Eqs. (2.21) and (2.23) can be simplified to:

$$V_z \frac{\partial V_+}{\partial z} = \frac{e}{m_i} E_0 + i\omega \frac{z}{L} V_+, \tag{2.72}$$

$$V_z \frac{\partial V_z}{\partial z} = \frac{|V_+|^2}{2L}, \tag{2.73}$$

where E_0 is the value of E_+ at $z = 0$. We solve Eqs. (2.72) and (2.73) with the boundary conditions:

$$V_+(z = -a) = i \frac{eL}{m_i a} E_0, \qquad\qquad V_z(z = -a) = u, \tag{2.74}$$

where u is the incident flow velocity and a is an outer boundary for the narrow layer solution. It should be noted that u is generally different from V_0 because the flow may accelerate between $z = -\infty$ and $z = -a$, i.e. before the ions enter the narrow transformation layer. The value of a needs to be chosen to satisfy the condition:

$$\delta \ll a \ll \delta_E, \tag{2.75}$$

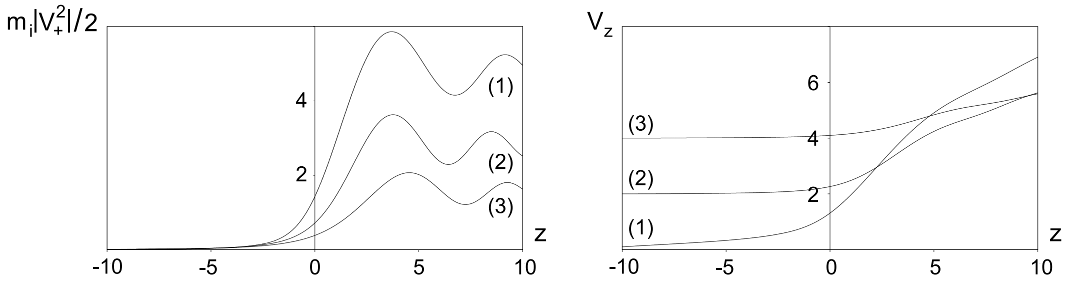

Figure 2.6: Solutions of Eqs. (2.72) and (2.73) for three different values of the incident flow velocity u: (1) $u = 0.1$; (2) $u = 2$; (3) $u = 4$. The flow velocity V_z is normalized to $L\omega \left[\frac{eE_0}{m_i L\omega^2}\right]^{4/5}$. The rotational energy $m_i|V_+|^2/2$ and distance from the resonance z are normalized to $\frac{m_i}{2}L^2\omega^2 \left[\frac{eE_0}{m_i L\omega^2}\right]^{6/5}$ and $L\left[\frac{eE_0}{m_i L\omega^2}\right]^{2/5}$ respectively.

where δ_E is the scale-length of the wave electric field and δ is the width of the transformation layer. This condition ensures that the physical results are insensitive to a.

Plots of $m_i|V_+|^2(z)/2$ and $V_z(z)$ for different values of u are shown in Fig. 2.6. Note that the change in V_z is relatively small for large values of u, which corresponds to the linear regime discussed in Sec. 2.3. The change in V_z becomes more significant as u decreases, so that the problem becomes essentially nonlinear. An important feature of the nonlinear regime is that the ion energy gain tends to a finite limit as u goes to zero. This means that the nonlinearity limits the particle energy gain. In the limit of small u, the energy gain per particle is roughly $m_i L^2\omega^2 \left[\frac{e|E_0|}{m_i L\omega^2}\right]^{6/5}$ as opposed to $m_i L^2\omega^2 \frac{L\omega}{V_z}\left[\frac{e|E_0|}{m_i L\omega^2}\right]^2$ in the linear regime. This shows that the total outgoing energy flux decreases when the particle motion becomes nonlinear. As the particles are now unable to carry away all of the incident wave energy, a significant part of the energy must go into a reflected wave. Another way to understand the reflection is to take into account that the ion density exhibits a steep drop in the nonlinear regime, which happens over a distance that is shorter than the wave-length. This can roughly be viewed as a discontinuity in a dielectric constant which usually causes partial reflection[2].

In order to find the reflection coefficient one would need to match the narrow resonance solution, described in this section, to the outer solution of Eqs. (2.19)-(2.23). This matching is straightforward when the linear approximation applies to the outer solution, so that the ion density does not change considerably over the interval from $z = -\infty$ to $z = -\delta_E$. Our estimates show that this requires $P/P_* < \gamma^2$. However, if P is greater than $P_*\gamma^2$, the outer solution itself is essentially nonlinear, which complicates the matching problem. One might think of using a WKB approximation to find the nonlinear outer solution, but the presence of a reflected wave will most likely preclude such an approach. The reason is that the interference between the incident and reflected waves will cause modulations of $|V_+|^2$, V_z, and n on a wave-length scale. This modulation can easily enhance the reflection or may even become the primary reflection mechanism. Because of its technical difficulty we will address the nonlinear reflection problem numerically rather than analytically. The corresponding calculations are described in the next section.

2.5 Global Picture

The set of Eqs. (2.19)-(2.23) derived in Sec. 2.2 is limited to a narrow region near the ion cyclotron resonance. In order to describe a broader spatial interval, we need to take into account:

a) the electron current,

b) deviation from the linear profile of the equilibrium magnetic field.

In the ion-cyclotron frequency range, the $\mathbf{E} \times \mathbf{B}$ drift gives rise to $x-$ and

---

[2] The possibility of the rf-power reflection due to the density drop at the resonance was mentioned earlier in Ref.[19] in connection with the ECRH problem.

$y-$components of the electron current,

$$j_\alpha^e = -e_{\alpha\beta\gamma} E_\beta \frac{B_{0\gamma}}{|B_0|} \frac{\omega_{pe}^2}{4\pi|\omega_{ce}|}, \tag{2.76}$$

where where $e_{\alpha\beta\gamma}$ is the completely antisymmetric unit tensor. This electron current is comparable to the ion current away from the resonance, which is why it becomes important in the global picture.

Generalization from the near-resonance expression, Eq. (2.1), to an arbitrary profile $B_{0z}(z)$ involves generalization of the quantities E_+, B_+, and V_+. In this section, we define E_+ as

$$E_+ \equiv \frac{E_x + iE_y}{\sqrt{B_{0z}/B_*}}, \tag{2.77}$$

where B_* is the value of the magnetic field at the point $\omega = \omega_{ci}$. The new expressions for B_+ and V_+ are similar to Eq. (2.77). It should be noted that these generalized definitions of E_+, B_+, and V_+ are fully consistent with the ones we used in the local description.

We will skip a straightforward derivation of the generalized set of equations and just present the modified equations in their final form:

$$\frac{\partial E_+}{\partial z} = \frac{\omega B_+}{c}, \tag{2.78}$$

$$\frac{\partial B_+}{\partial z} = \frac{\omega_{pi}^2}{\omega_{ci} c} E_+ - \frac{4\pi i}{c} neV_+, \tag{2.79}$$

$$V_z \frac{\partial V_+}{\partial z} = \frac{e}{m_i} E_+ + i(\omega - \omega_{ci})V_+, \tag{2.80}$$

$$V_z \frac{\partial V_z}{\partial z} = -\frac{1}{8\pi m_i n} \frac{B_{0z}}{B_*} \frac{\partial |B_+|^2}{\partial z} - \frac{|V_+|^2}{2B_*} \frac{\partial B_{0z}}{\partial z} - \frac{c_s^2}{n} \frac{\partial n}{\partial z}, \tag{2.81}$$

$$\frac{B_*}{B_{0z}} nV_z \equiv j = const. \tag{2.82}$$

This set of equations now describes both the resonant conversion of the incident wave energy into the ion rotational energy and the subsequent transformation of the ion rotation into their fast motion along the decreasing magnetic field.

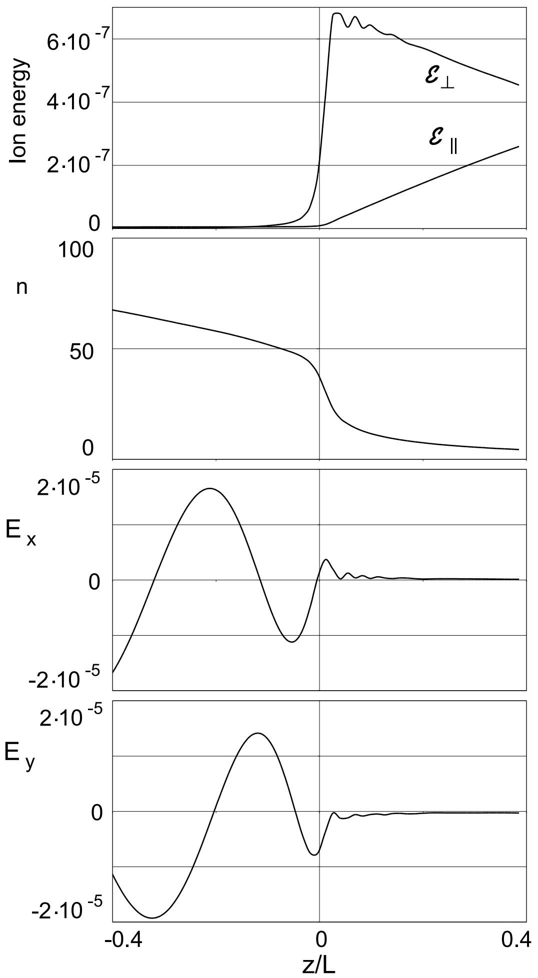

Figure 2.7: Solution of Eqs. (2.78)-(2.82) for $j = 5 \cdot 10^5(m_i\omega c^2)/(4\pi Le^2)$, $\bar{n} = 100 \cdot m_ic^2/4\pi e^2L^2$, and $|\bar{E}| = \sqrt{10} \cdot 10^{-5} \cdot m_iL\omega^2/e$. The quantities $\mathcal{E}_\perp \equiv m_i|V_+|^2B_{0z}/2B_*$ and $\mathcal{E}_\parallel \equiv m_iV_z^2/2$ are normalized to $m_iL^2\omega^2$. The ion density n and the electric field components E_x and E_y are normalized to $m_ic^2/4\pi e^2L^2$ and $m_iL\omega^2/e$ respectively.

We solve Eqs. (2.78)-(2.82) numerically for $s = 0$ and for a specific profile of the equilibrium magnetic field:

$$B_{0z} = B_*\left[1 - \frac{z}{\sqrt{L^2+z^2}}\right]. \tag{2.83}$$

This expression represents the near-axis field of an open-ended solenoid. Our code integrates Eqs. (2.78)-(2.82) starting from the strong field side with an adjustable boundary condition at a large negative value of z. The code employs a shooting procedure to find the solution for which E_+ and B_+ vanish in the outgoing flow (at $z \rightarrow$

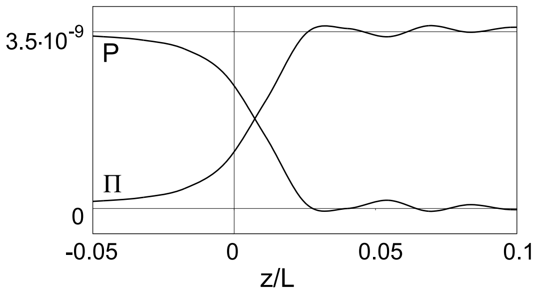

Figure 2.8: Conversion of the Poynting vector P into the ion power flux Π. The plot corresponds to the solution presented in Fig. 2.7. The quantities P and Π are normalized to $Lm_i^2c^2\omega^3/4\pi e^2$.

∞). This allows us to automatically determine the amplitude of the reflected wave in the case of nonlinear reflection. Each solution is characterized by three parameters: the particle flux j, the mean density $\bar{n}$ and the mean electric field amplitude $|\bar{E}|$ in the incident flow ($z \to -\infty$).

Figures 2.7 and 2.8 show a solution that represents a moderately nonlinear regime. The density plot in Fig. 2.7 already exhibits a steep gradient near the resonance but with a very minor reflection yet. The amount of reflection can be inferred from the oscillations of $|E|^2 \equiv E_x^2 + E_y^2$ shown in Fig. 2.9. These oscillations represent an interference between the incident and the reflected waves. The oscillations become more pronounced in the case of a stronger rf-field or slower ion flow. Related to the reflection are density and velocity modulations in the incoming flow. As seen from Fig. 2.9 (right), the decrease in the flow velocity can produce a larger reflection even when the rf-field is weaker than that shown in Fig. 2.9 (left).

2.6 Summary

We have presented a self-consistent nonlinear model for the deposition of rf-power in the ion cyclotron frequency range into a steady state plasma flow. This work can be viewed as a nonlinear version of the magnetic beach problem [22] for ion-cyclotron waves. We find that the absorption coefficient for the wave is 100% as long

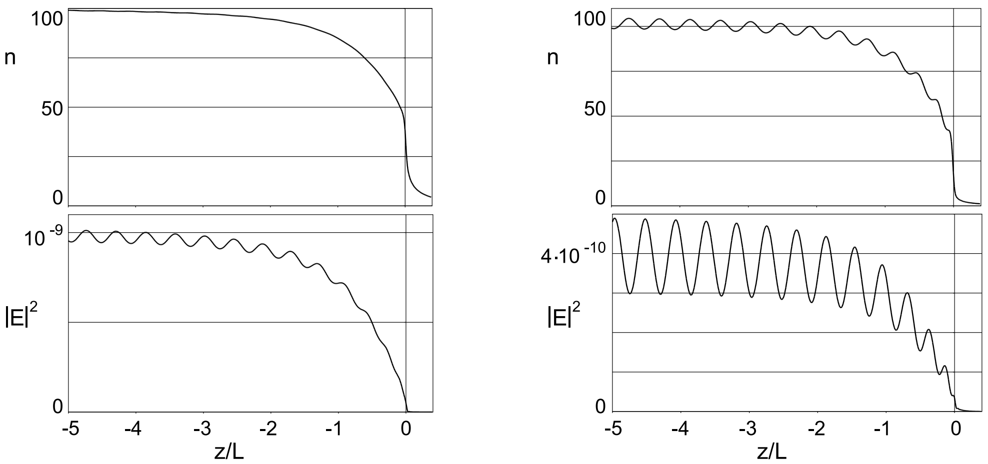

Figure 2.9: Modulation of the wave amplitude and ion density due to nonlinear reflection from the resonance. Left plots correspond to the solution presented in Fig. 2.7. Right plots correspond to the solution with $j = 1.5 \cdot 10^5 (m_i \omega c^2)/(4\pi L e^2)$, $\bar{n} = 100 \cdot m_i c^2 / 4\pi e^2 L^2$, and $|\bar{E}| = 2 \cdot 10^{-5} \cdot m_i L \omega^2 / e$. Quantities n and $|E|^2$ are normalized to $m_i L^2 \omega^2$ and $m_i^2 L^2 \omega^4 / e^2$ respectively.

as either linear theory or WKB approximation applies to the problem. Acceleration of the incoming ions due to the energy deposition from the wave adds nonlinear features to the absorption process. The longitudinal forces create a density gradient in the ion flow, which causes partial reflection of the incident rf-power. The reflection is most pronounced when the characteristic scale-length of the density drop becomes shorter than the wavelength. An interesting consequence of this nonlinear reflection is the spatial modulation of the incident flow. Simple one-dimensional fluid-type simulations, described in this chapter, confirm our theoretical picture of the near-resonance behavior and allow us to quantitatively model the entire process of wave energy conversion into the directed energy of the ion flow. We envisage two natural extensions of the presented work. First, our single-fluid model can be generalized to the case of several groups of ions with different parallel velocities. This should allow us to evaluate the role of the ion velocity spread in the incident flow. Second, for practical applications like VASIMR, the basic nonlinear effects discussed in this chapter need to be combined with two-dimensional calculations of the wave field. The need for such an extension becomes evident if one takes into account that the finite plasma radius should definitely affect the field structure in a realistic geometry.

Chapter 3

Radially Localized Helicon Modes in Nonuniform Plasma

3.1 Introduction

An importance of the radial density gradient in the helicon discharge was recognized in Ref. [7, 8] and examined in more detail in Ref. [9], based on numerical solutions of the wave equation. However, numerical solutions alone fail to elucidate the underlying physics and all the subtleties of the problem. The analytic approach described below fills this gap.

We will show that the radial nonuniformity of the plasma has a surprisingly strong effect on the structure of the helicon modes with *nonzero values* of the azimuthal mode number m. As a result, the corresponding mode frequency turns out to be *significantly lower* than what one would expect from the dispersion relation for a uniform plasma. This effect is most pronounced in the limit of a small longitudinal wavenumber k_z,

$$k_z \ll \min\left(\frac{\omega_{pe}}{c}; \frac{1}{a}\right), \tag{3.1}$$

where ω_{pe} is the electron plasma frequency and a is the characteristic radius of the plasma density profile. The new eigenmode is a helicon mode coupled to space charge effects from electron $\mathbf{E} \times \mathbf{B}$ drift in nonuniform plasma. It has distinct features of a surface wave.

It should be pointed out that this unusual eigenmode cannot be inferred from the early studies of helicons in a homogeneous plasma with a sharp density boundary [10, 11]; nor does this mode appear in axisymmetric problems of electron magnetohydrodynamics (EMHD) [12, 13]. Ironically, the sharp boundary assumption bans this mode: we find that the mode is sensitive to the structure of the density profile when the width of the boundary is smaller than c/ω_{pe}. Also, this mode is necessarily nonaxisymmetric, unlike solutions discussed in Refs. [12, 13].

We will consider an axisymmetric plasma cylinder in a uniform equilibrium magnetic field $\mathbf{B}_0$ directed along the axis of symmetry (z). The unperturbed plasma density, which is a function of radius r, is uniform in the azimuthal (ϕ) and axial (z) directions. Our starting point is the linear wave equation

$$\nabla(\nabla\mathbf{E}) - \nabla^2\mathbf{E} = -\frac{1}{c^2}\frac{\partial^2\mathbf{D}}{\partial t^2} - \frac{4\pi}{c^2}\frac{\partial\mathbf{j}}{\partial t}, \tag{3.2}$$

where $\mathbf{E}$ is the electric field, $\mathbf{D}$ is the electric displacement, and $\mathbf{j}$ is the antenna current density. We use Fourier expansion in t in order to present $\mathbf{E}$, $\mathbf{D}$, and $\mathbf{j}$ in the following form:

$$\mathbf{E} = \frac{1}{2}\sum_{\omega}\mathbf{E}(\omega)\mathrm{e}^{-i\omega t} + c.c., \tag{3.3}$$

$$\mathbf{D} = \frac{1}{2}\sum_{\omega}\mathbf{D}(\omega)\mathrm{e}^{-i\omega t} + c.c., \tag{3.4}$$

$$\mathbf{j} = \frac{1}{2}\sum_{\omega}\mathbf{j}(\omega)\mathrm{e}^{-i\omega t} + c.c., \tag{3.5}$$

where $\mathbf{E}(\omega)$, $\mathbf{D}(\omega)$, and $\mathbf{j}(\omega)$ are the Fourier images. This representation transforms Eq. (3.2) into:

$$\nabla\left[\nabla\mathbf{E}(\omega)\right] - \nabla^2\mathbf{E}(\omega) = \frac{\omega^2}{c^2}\mathbf{D}(\omega) + \frac{4\pi\omega i}{c^2}\mathbf{j}(\omega). \tag{3.6}$$

The electric displacement $\mathbf{D}(\omega)$ is related to the electric field $\mathbf{E}(\omega)$ by the cold plasma dielectric tensor $\varepsilon_{\alpha\beta}$, namely

$$D_\alpha(\omega) = \varepsilon_{\alpha\beta}E_\beta(\omega). \tag{3.7}$$

The cold plasma approximation implies that the longitudinal phase velocity ω/k_z is much greater than particle thermal velocity v_{th}. For the modes discussed in this chapter, we find that ω scales as k_z^2. Hence the restriction $\omega/k_z \gg v_{th}$ limits k_z from below. This restriction also assures that Landau damping is low for these modes.

The three components of Eq. (3.7) in the cylindrical coordinates (r, ϕ, z) have the form

$$D_r(\omega) = \varepsilon E_r(\omega) + igE_\phi(\omega), \tag{3.8}$$

$$D_\phi(\omega) = -igE_r(\omega) + \varepsilon E_\phi(\omega), \tag{3.9}$$

$$D_z(\omega) = \eta E_z(\omega), \tag{3.10}$$

with [37]

$$\varepsilon = 1 - \sum_\alpha \frac{\omega + i\nu_\alpha}{\omega} \frac{\omega_{p\alpha}^2}{(\omega + i\nu_\alpha)^2 - \omega_{c\alpha}^2}, \tag{3.11}$$

$$g = -\sum_\alpha \frac{\omega_{c\alpha}}{\omega} \frac{\omega_{p\alpha}^2}{(\omega + i\nu_\alpha)^2 - \omega_{c\alpha}^2}, \tag{3.12}$$

$$\eta = 1 - \sum_\alpha \frac{\omega_{p\alpha}^2}{\omega\,(\omega + i\nu_\alpha)}. \tag{3.13}$$

Here the subscript α labels particle species, namely electrons and ions. $\omega_{c\alpha} = q_\alpha B_0/m_\alpha c$ is the gyrofrequency, $\omega_{p\alpha} = \sqrt{4\pi n_\alpha q_\alpha^2/m_\alpha}$ is the plasma frequency, and ν_α is the collision frequency.

In what follows, the plasma is assumed to be sufficiently dense so that

$$\omega_{ce} \ll \omega_{pe}. \tag{3.14}$$

This condition ensures that the displacement current is negligibly small compared to the plasma current. Next, we assume that the wave frequency satisfies the condition

$$\sqrt{\omega_{ci}\omega_{ce}} \ll \omega \ll \omega_{ce}, \tag{3.15}$$

which allows us to neglect the ion current compared to the electron current. The electron collision frequency ν_e is assumed to be comparable or smaller than ω. Then the quantities ε, g, and η reduce to

$$\varepsilon = \frac{\omega_{pe}^2}{\omega_{ce}^2}\left(1 + \frac{i\nu_e}{\omega}\right), \qquad g = \frac{\omega_{pe}^2}{\omega\omega_{ce}}\left(1 + \frac{2i\nu_e\omega}{\omega_{ce}^2}\right), \qquad \eta = -\frac{\omega_{pe}^2}{\omega(\omega + i\nu_e)}, \tag{3.16}$$

with

$$\varepsilon \ll \quad g \ll \quad \eta. \tag{3.17}$$

Expressions (3.16) retain only the lowest order collisional contributions. As indicated by Eq. (3.1), we also assume that k_z is sufficiently small. This restriction allows us to treat the essential part of the problem analytically (see Section 3.3).

3.2 Eigenmode Equations

In this section, we derive eigenmode equations [Eqs. (3.30) and (3.31)] for a radially nonuniform plasma cylinder. In this derivation, we omit the antenna current that will be brought back in Sec. 3.4 to calculate the power deposition from the antenna.

We use Fourier expansion in z and ϕ to present the electric field $\mathbf{E}(\omega)$ in the following form:

$$\mathbf{E}(\omega) = \sum_{m,k_z} \left[\mathbf{e}_r E_r(\omega, k_z, m, r) + \mathbf{e}_\phi E_\phi(\omega, k_z, m, r) + \mathbf{e}_z E_z(\omega, k_z, m, r)\right] \mathrm{e}^{im\phi + ik_z z}. \tag{3.18}$$

Note that a similar representation for $\mathbf{j}(\omega)$,

$$\mathbf{j}(\omega) = \sum_{m,k_z} \left[\mathbf{e}_r j_r(\omega, k_z, m, r) + \mathbf{e}_\phi j_\phi(\omega, k_z, m, r) + \mathbf{e}_z j_z(\omega, k_z, m, r)\right] \mathrm{e}^{im\phi + ik_z z}, \tag{3.19}$$

will be used later in this chapter.

The wave equation (3.6) without the antenna current reduces to a set of equations for the Fourier amplitudes E_r, E_ϕ, and E_z. To simplify the equations, we will drop the arguments ω, m, and k_z of the amplitudes. For a single harmonic we obtain:

$$E_r\left(\frac{m^2}{r^2} + k_z^2\right) + \frac{im}{r}\left(\frac{\partial E_\phi}{\partial r} + \frac{E_\phi}{r}\right) + ik_z\frac{\partial E_z}{\partial r} = \frac{\omega^2}{c^2}(\varepsilon E_r + igE_\phi), \tag{3.20}$$

$$im\frac{\partial}{\partial r}\left(\frac{E_r}{r}\right) - \frac{\partial}{\partial r}\left(\frac{\partial E_\phi}{\partial r} + \frac{E_\phi}{r}\right) + k_z^2 E_\phi - \frac{mk_z}{r}E_z = \frac{\omega^2}{c^2}(\varepsilon E_\phi - igE_r), \tag{3.21}$$

$$\frac{ik_z}{r}\frac{\partial}{\partial r}(rE_r) - \frac{k_z m}{r}E_\phi - \frac{1}{r}\frac{\partial}{\partial r}\left(r\frac{\partial E_z}{\partial r}\right) + \frac{m^2}{r^2}E_z = \frac{\omega^2}{c^2}\eta E_z. \tag{3.22}$$

We will only discuss the nonaxisymmetric modes ($m \neq 0$) since the axisymmetric mode ($m = 0$) does not exhibit any unexpected features.

To further simplify the problem for $m \neq 0$ we note that assumptions (3.1) and (3.15) allow us to formally treat k_z and ω as small parameters in Eqs. (3.20) and (3.21). Since ω turns out to scale as k_z^2 [see Eqs. (3.36) and (3.40)], we put to lowest order $k_z = 0$ and $\omega = 0$ in Eqs. (3.20) and (3.21). In this limit, Eqs. (3.20) and (3.21) become degenerate. They both read:

$$\frac{im}{r}E_r = \frac{\partial E_\phi}{\partial r} + \frac{1}{r}E_\phi. \tag{3.23}$$

A convenient way to resolve the degeneracy is to replace Eq. (3.21) by the condition div$\mathbf{D} = 0$, which is exact and does not contain the lowest order terms. This condition has the form

$$\frac{1}{r}\frac{\partial}{\partial r}[r(\varepsilon E_r + igE_\phi)] + \frac{im}{r}[\varepsilon E_\phi - igE_r] + ik_z\eta E_z = 0. \tag{3.24}$$

Equations (3.22), (3.23), and (3.24) form a closed set that can be reduced to just two equations

$$\frac{1}{r}\frac{\partial}{\partial r}\left[r\frac{\partial E}{\partial r}\right] - \frac{m^2}{r^2}E = -\frac{\omega^2}{c^2}\eta E_z, \tag{3.25}$$

$$\frac{1}{r}\frac{\partial}{\partial r}\left[\varepsilon r\frac{\partial}{\partial r}(E_z - E)\right] - \frac{m}{r}\left[\frac{\partial g}{\partial r} + \frac{\varepsilon m}{r}\right](E_z - E) - k_z^2\eta E_z = 0, \tag{3.26}$$

where the new unknown function

$$E = E_z - \frac{k_z r}{m}E_\phi \tag{3.27}$$

measures the Fourier amplitude of the radial component of the perturbed magnetic field as

$$H_r = \frac{cm}{\omega r}E. \tag{3.28}$$

We now take into account that ε is much smaller than g for the modes we are interested in. The smallness of ε allows us to decouple Eqs. (3.25) and (3.26). Note that the ε-terms in Eq. (3.26) are negligible unless the radial scalelength of the function $E_z - E$ is much smaller than the radial scalelength of g (we assume m to be not a large number). Hence, for sufficiently smooth modes, we can replace Eq. (3.26) by an algebraic relationship,

$$E = E_z \left[1 + k_z^2 r \eta \left(m \frac{\partial g}{\partial r} \right)^{-1} \right], \tag{3.29}$$

which leads to

$$\frac{1}{r} \frac{\partial}{\partial r} \left[r \frac{\partial E}{\partial r} \right] - \frac{m^2}{r^2} E = - \frac{m}{k_z^2 r} \frac{\omega^2}{c^2} \frac{E \partial g / \partial r}{1 + (m \partial g / \partial r) / k_z^2 r \eta}. \tag{3.30}$$

The explicit conditions of validity for this equation will be given below [see Eqs.(3.38) and (3.47)] in connection with its solutions.

Another way to simplify Eqs. (3.25) and (3.26) is to consider modes that significantly involve the ε-terms in Eq. (3.26). For these modes, Eq. (3.25) indicates that E has to be much smaller than E_z because one needs very short radial scales to retain the ε-terms in Eq. (3.26). We can then neglect E in Eq. (3.26) to find

$$\frac{1}{r} \frac{\partial}{\partial r} \left[\varepsilon r \frac{\partial}{\partial r} E_z \right] - \frac{m}{r} \left[\frac{\partial g}{\partial r} + \frac{\varepsilon m}{r} \right] E_z - k_z^2 \eta E_z = 0. \tag{3.31}$$

This equation describes nearly electrostatic perturbations (the Gould-Trivelpiece modes) which are somewhat modified by plasma density gradient.

The density gradient is essential for a mode described by Eq. (3.30), while it does not have such a strong effect on the Gould-Trivelpiece mode. Indeed, an eigenmode described by Eq. (3.30) does not exist in uniform plasma if $m \neq 0$, as it follows directly from Eq. (3.30). Equation (3.30) resembles a one-dimensional Schrodinger equation for a particle in the external field, which becomes obvious if we introduce a new variable $s = \ln r$ and rewrite the equation in the following form:

$$\frac{\partial^2 E}{\partial s^2} + \left[(-m^2) - U(s) \right] E = 0. \tag{3.32}$$

The function U is given by:

$$U \equiv -\frac{mr}{k_z^2}\frac{\omega^2}{c^2}\frac{\partial g/\partial r}{1+(m\partial g/\partial r)/k_z^2 r\eta}, \tag{3.33}$$

which becomes a definition of $U(s)$ if one expresses r as $\exp(s)$. In the context of this analogy, one can say that quantity $(-m^2)$ represents particle energy, while $U(s)$ represents the potential energy. Plasma density gradient determines the profile of $U(s)$ [see Eq. (3.30)], with $U = 0$ where the gradient is zero. If the right-hand side of Eq. (3.30) is negative, then the density gradient forms a potential well. The eigenmode corresponds to a bound state with "energy" $(-m^2)$ in the potential well. We can use this quantum mechanical picture to describe eigenmodes for a given density profile. Consider a case when the density gradient term in the denominator of $U(s)$ can be neglected, so that the depth of the well is proportional to the frequency ω. If the frequency is too low, then the $(-m^2)$ energy level does not fit into the well. As the depth of the well increases with ω, the bound states appear and they meet the $(-m^2)$ energy level sequentially. The eigenmode with the lowest possible frequency corresponds to the ground state, so that the field of this mode does not have radial oscillations. Other bound states correspond to the modes with higher frequencies and higher radial wave numbers. Later in this chapter we will refer to this quantum mechanical picture when we discuss specific solutions of Eq. (3.30)).

3.3 Analytic Solutions

With some natural assumptions, Eq.(3.30) can be solved analytically for radially localized helicon modes. In order to do that, we consider two limiting cases $\omega_{pe}a/c \gg 1$ and $\omega_{pe}a/c \ll 1$ and we neglect collisions to find the mode frequency and the mode structure in the absence of dissipation.

The first condition ($\omega_{pe}a/c \gg 1$) actually means that the parallel electric field is negligibly small. Formally, this allows us to neglect the $\partial g/\partial r$ term in the denominator on the right-hand side of Eq. (3.30). We can then construct a surface-wave solution by choosing a step-like radial profile of the plasma density:

$$n = \begin{cases} n_- & \text{if } r < r_0 \\ n_+ & \text{if } r > r_0, \end{cases}$$

so that

$$\frac{\partial g}{\partial r} = (g(n_+) - g(n_-))\delta(r - r_0). \tag{3.34}$$

Note, however, that the width of the narrow transition layer δ_{layer} at $r = r_0$ still has to be large compared to the skin depth c/ω_{pe}. Outside the layer, the solution has the form

$$E = E_0 \begin{cases} (r/r_0)^{|m|} & \text{if } r < r_0 \\ (r/r_0)^{-|m|} & \text{if } r > r_0, \end{cases} \tag{3.35}$$

where E_0 is a constant. We have taken into account that the solution must be continuous at $r = r_0$. Integration of Eq. (3.30) through the transition layer with expression (3.34) for $\partial g/\partial r$ gives the following dispersion relation:

$$\omega = 2\frac{m}{|m|}\frac{\omega_{ce}k_z^2c^2}{\omega_{pe}^2(n_+) - \omega_{pe}^2(n_-)}. \tag{3.36}$$

We now recheck the validity of Eq.(3.30) for this mode or, equivalently, we verify that the ε-terms can be neglected in Eq.(3.26). We note that the characteristic scalelength of the function $E - E_z$ is a. However, its radial derivative changes on the δ_{layer} scale. Then the first term in Eq.(3.26) can be estimated as $\varepsilon(E_z - E)/a\delta_{layer}$ and $\partial g/\partial r$ term in the same equation can be estimated as $g(E_z - E)/a\delta_{layer}$. Hence the first term can be neglected in comparison with the $\partial g/\partial r$ term if

$$\varepsilon \ll g, \tag{3.37}$$

which is indeed the case for the modes with frequencies lower than ω_{ce}. An additional applicability condition comes from the restriction $\omega/k_z \gg v_{th}$, imposed by the cold plasma approximation. As previously mentioned, this condition limits k_z from below. Together with Eq.(3.1) it gives a range of longitudinal wave numbers k_z for which the mode exists and is weakly damped despite its relatively low longitudinal phase velocity. The resulting restriction is

$$\frac{v_{th.e}}{\omega_{ce}a}\left[\frac{\omega_{pe}a}{c}\right]^2 \ll k_z a \ll 1. \tag{3.38}$$

The second limiting case ($\omega_{pe}a/c \ll 1$) also gives an eigenmode associated with the density gradient. In this case, the mode is centered at the point $r = r_*$ where the function

$$f(r) = -\frac{1}{rn}\frac{dn}{dr} \tag{3.39}$$

has a maximum, and the mode frequency turns out to be very close to

$$\omega_* = -\omega_{ce}\frac{k_z^2}{mf(r_*)}, \tag{3.40}$$

which is the value that makes the denominator in Eq. (3.30) vanish at $r = r_*$. Therefore, we take

$$\omega = \omega_*(1 - \triangle^2), \tag{3.41}$$

where the value of the small parameter $\triangle$ is to be determined by the boundary condition for the outside solution similar to (3.35)

$$E = E_*\begin{cases} (r/r_*)^{|m|} & \text{if } r < r_* \\ (r/r_*)^{-|m|} & \text{if } r > r_*, \end{cases} \tag{3.42}$$

where E_* is a constant. The right-hand side of equation (3.30) is now sharply peaked around the point $r = r_*$, so that Eq. (3.30) can be simplified to

$$\frac{1}{r}\frac{\partial}{\partial r}\left[r\frac{\partial E}{\partial r}\right] - \frac{m^2}{r^2}E = -\frac{\omega_{pe}^2(r_*)}{c^2}E\left(\triangle^2 + \left|\frac{1}{2f}\frac{d^2 f}{dr^2}\right|(r-r_*)^2\right)^{-1}, \tag{3.43}$$

where f and d^2f/dr^2 should be evaluated at $r = r_*$. Except for the narrow vicinity of the point $r = r_*$, the right–hand side of this equation is negligibly small, which readily gives the dispersion relation via integrating Eq. (3.43) through the transition layer at $r = r_*$. The result is

$$\triangle^2 = \frac{\pi^2}{2m^2}\frac{\omega_{pe}^4(r_*)r_*^2}{c^4}\left|\frac{f}{d^2f/dr^2}\right|_{r=r_*} \ll 1. \tag{3.44}$$

This result can be easily generalized to the case of small but finite resistivity by taking into account electron collision frequency. It is sufficient to include ν_e only in the expression for η in Eq.(3.30) since the contribution from the imaginary part of g will be smaller by factor ω/ω_{ce}. The derivation of the corresponding dispersion relation repeats the one used to obtain Eq. (3.41), but Δ^2 now becomes a complex quantity given by

$$\Delta^2 = \frac{\pi^2}{2m^2}\frac{\omega_{pe}^4(r_*)r_*^2}{c^4}\left|\frac{f}{d^2f/dr^2}\right|_{r=r_*} + i\nu_e/\omega_*. \tag{3.45}$$

The derivation of Eq. (3.42) implies that $\nu_e \ll \omega_*$, a condition that "breaks down" for very steep density profiles. This bans the mode in the sharp boundary problem [10, 11].

We now specify the window of existence for the mode described by Eqs.(3.41)-(3.44). The corresponding derivation is similar to that of Eq.(3.38). As seen from Eq.(3.29), the function $|E_z(r)|$ for this mode is sharply peaked near the point $r = r_*$. It should also be noted that the ratio of $|E|$ to $|E_z|$ is roughly $\triangle^2 \ll 1$. The width of the peak is

$$\delta_{mode} = \triangle\sqrt{f\left/\frac{d^2f}{dr^2}\right.}. \tag{3.46}$$

In order to neglect the first term in Eq.(3.26), we need this term to be smaller than $\frac{m}{r}\frac{\partial g}{\partial r}E$, the smallest term retained in Eq.(3.29). Assuming that the characteristic scalelength of the density profile is δ, we get the following constraint

$$\frac{v_{th.e}}{\omega_{ce}a}\left[\frac{\omega_{pe}a}{c}\right]^2\frac{1}{\triangle} \ll k_z a \ll \triangle^2. \tag{3.47}$$

The left inequality in this equation assures low rate of the Landau damping. It should be noted that the smallness of $\triangle$ makes Eq.(3.47) somewhat more restrictive than Eq.(3.38). Nevertheless, this constraint can still be satisfied for sufficiently small values of $v_{th.e}$.

It is significant that, in both limiting cases ($\omega_{pe}\, a/c \gg 1$ and $\omega_{pe}\, a/c \ll 1$), the mode involves a perturbed “surface” current that is localized near the peak of the eigenfunction $E(r)$. It is due to this current that the radial derivative of $E(r)$ as well as the azimuthal component of the perturbed magnetic field are discontinuous in the outside solutions (3.35) and (3.42). The existence of this localized current distinguishes the above modes from those discussed in Refs. [10, 11].

In conclusion, we note that we found the eigenmodes which, in the context of the quantum mechanical analogy discussed in Sec. 3.2, correspond to the ground state. In both cases, the potential U is essentially a δ-function. A δ-well has only one bound state, that is the ground state, with energy depending on the “depth” of the well. Equations (3.36) and (3.40) specify the value of ω for which the depth of the well is such that the “energy” equals $(-m^2)$.

3.4 Resonant Power Absorption

In the previous section we have considered two limiting cases and found low frequency eigenmodes described by Eq. (3.30). In general, one can find eigenmodes of Eq. (3.30) only numerically, which we will do in this section. We will also compute power absorption by the plasma.

We use the following procedure to find the eigenmodes. We allow energy dissipation via collisions and we also bring back the antenna current, which drives the wave and supplies the power. The wave amplitude in this case is determined by the power balance condition. If the antenna frequency coincides with an eigenmode frequency, then the eigenmode is excited and a well pronounced peak of *resonant power absorption* must be observed at this frequency. One can thereby relate the eigenmodes to the absorption peaks.

As already pointed out, the power absorption by plasma is equal to power supplied by the antenna. Technically, it is easier to calculate the power at the antenna, which involves integration of $\mathbf{jE}$ over the antenna. We will consider an antenna made out of thin wire, so that we can disregard the wire width while performing the integration. The antenna power is a sum of partial contributions from the Fourier harmonics of the current. This immediately follows from Eqs. (3.3), (3.5), (3.18), and (3.19), which present Fourier expansions for $\mathbf{E}$ and $\mathbf{j}$.

In order to identify an eigenmode it is sufficient to retain only the corresponding Fourier component in $\mathbf{j}$. For this purpose the shape of the antenna is insignificant, however it is convenient to choose a radially localized antenna with radius R. Then the Fourier amplitudes j_r, j_ϕ, and j_z are given by:

$$\begin{aligned} j_r(\omega, k_z, m, r) &= 0, && (3.48) \\ j_\phi(\omega, k_z, m, r) &= -\left(\frac{k_z R}{m}\right) j_0 R\delta(r-R), && (3.49) \\ j_z(\omega, k_z, m, r) &= j_0 R\delta(r-R), && (3.50) \end{aligned}$$

where the constant j_0 is determined by the antenna geometry, and we have taken into account that j_ϕ and j_z are related to each other by the condition $\mathrm{div}\mathbf{j} = 0$. The coefficient j_0 for a helical antenna is calculated in Appendix A [see Eq. (A.7)]. It is straightforward to show now that the power deposition per harmonic is given by:

$$Q = \frac{\pi R^2}{2} j_0 \left[E_z^*(\omega, m, k_z, R) - \left(\frac{k_z R}{m}\right) E_\phi^*(\omega, k_z, m, R) \right] + c.c. \tag{3.51}$$

The Fourier amplitudes E_ϕ and E_z can be expressed in terms of E via Eqs. (3.27) and (3.29), which leads to the following expression for Q:

$$Q = \frac{\pi R^2}{2} \left[E^*(R) j_0 + E(R) j_0^* \right]. \tag{3.52}$$

The field E is described by Eq. (3.30), to which we now add the antenna current. Note that $\mathbf{j}(\omega)$ and $\mathbf{D}(\omega)$ enter wave equation (3.6) in the following combination: $\frac{\omega^2}{c^2}\mathbf{D}(\omega) + \frac{4\pi\omega i}{c^2}\mathbf{j}(\omega)$. The right-hand side of Eq. (3.30) represents $-\frac{\omega^2}{c^2} D_z(\omega)$.

Therefore, in order to describe the antenna, the term $-\frac{4\pi\omega i}{c^2} j_z(\omega, k_z, m, r)$ must be added to the right-hand side of Eq. (3.30):

$$\frac{1}{r}\frac{\partial}{\partial r}\left[r\frac{\partial E}{\partial r}\right] - \frac{m^2}{r^2}E = -\frac{m}{k_z^2 r}\frac{\omega^2}{c^2}\frac{E\partial g/\partial r}{1+(m\partial g/\partial r)/k_z^2 r\eta} - \frac{4\pi i\omega}{c^2} j_0 R\delta(r-R). \quad (3.53)$$

Here we used expression (3.50) for $j_z(\omega, k_z, m, r)$. Since the antenna current is zero everywhere except at $r = R$, then Eq. (3.53) is equivalent to Eq. (3.30) accompanied by the field matching conditions at $r = R$:

$$\begin{aligned} \left.\frac{\partial E}{\partial r}\right|_{R+0} - \left.\frac{\partial E}{\partial r}\right|_{R-0} &= -\frac{4\pi i\omega}{c^2} j_0 R, && (3.54) \\ E|_{R+0} - E|_{R-0} &= 0. && (3.55) \end{aligned}$$

These conditions are obtained by integrating Eq. (3.53) through a thin layer at $r = R$. We thus need to solve Eq. (3.30) for $r < R$ and for $r > R$ and then match the two solutions to satisfy Eqs. (3.54) and (3.55).

We conclude this section by presenting the power absorption spectrum $Q(\omega)$ for the helical antenna. The structure of the spectrum depends parametrically on $\omega_{pe}a/c$, since $\omega_{pe}a/c$ determines the type of existing eigenmodes in the plasma (see Sec. 3.3). In our calculations we present the plasma density in the form $n(r) = n_* G(r)$, where $G(r)$ is a function with a maximum value of 1. Then variation of n_* for the same $G(r)$ allows us to investigate regimes of dense ($\omega_{pe}a/c \gg 1$) and rarified ($\omega_{pe}a/c \ll 1$) plasma, as well as an intermediate regime ($\omega_{pe}a/c \sim 1$).

The routine used to compute Q is described in Appendix B. We define $G(r)$ by Eq. (B.1). It is convenient to normalize ω by introducing a dimensionless quantity Ω defined as:

$$\Omega \equiv -\frac{m^2\omega}{k_z^2 R^2 \omega_{ce}}. \quad (3.56)$$

We similarly normalize ν_e introducing a dimensionless quantity ν_0:

$$\nu_0 \equiv -\frac{m^2\nu_e}{k_z^2 R^2 \omega_{ce}}. \quad (3.57)$$

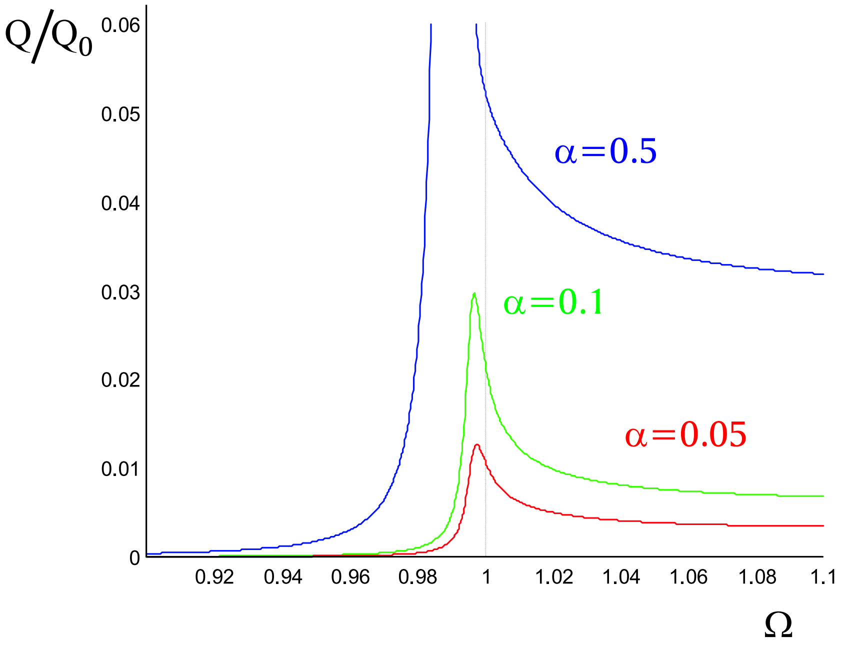

Figure 3.1: Plasma power absorption in the rarified plasma for the harmonic with $m = 1$.

Note that for $G(r)$ specified by Eq. (B.1), the value of Ω is 1 if ω equals to $\omega_*(m = 1)$ defined by Eq. (3.40). This means that the absorption peak for the $m = 1$ mode described by Eqs. (3.41) and (3.44) must be very close to $\Omega = 1$. In what follows, we use a dimensionless parameter α,

$$\alpha \equiv \left(\frac{\omega_{pe}(n_*)R}{c} \right)^2 , \tag{3.58}$$

to characterize the dependence of Q on $\omega_{pe}a/c$. The power absorption in Figs. 3.1, 3.2, 3.3, and 3.4 is normalized to

$$Q_0 \equiv \frac{(2\pi R)^2}{l^2 + (2\pi R)^2} \frac{I_0^2 \omega_{ce}}{2c^2}, \tag{3.59}$$

where I_0 is the maximum amplitude of the antenna current and l is a helix period [see Appendix A].

We start with the case of rarified plasma, i.e. the case when α is small. The plasma power absorption spectrums for $\alpha = 0.05$, $\alpha = 0.1$, and $\alpha = 0.5$ are shown in

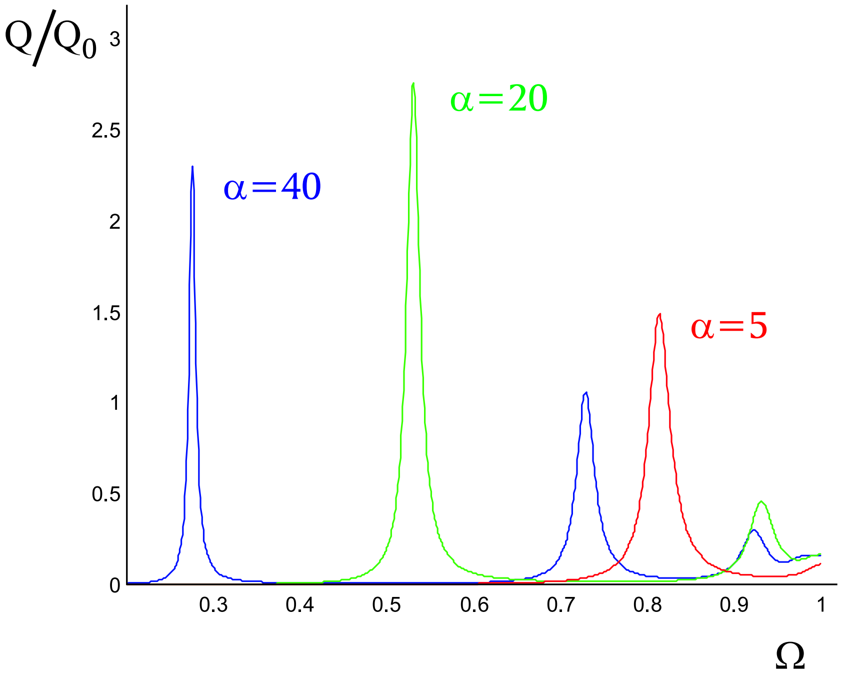

Figure 3.2: Plasma power absorption in the intermediate regime for the harmonic with $m = 1$.

Fig. 3.1. The peaks in absorption for $\alpha = 0.05$ and $\alpha = 0.1$ are associated with the mode described by Eqs. (3.41) and (3.44). As predicted by Eq. (3.41), the peaks are slightly shifted away from $\Omega = 1$ towards smaller values of Ω, with the magnitude of the shift increasing with plasma density. For all three spectrums the collision frequency is constant ($\nu_0 = 0.0025$). Despite the fact that ν_e is fixed, the hight of the absorption peaks increases with the increase of plasma density.

The hight of the absorption peaks reaches its maximum in the intermediate regime, as shown in Fig. 3.2. For all three spectrum curves, the collision frequency is constant and its value is the same ($\nu_0 = 0.02$). Several peaks in Q for a given α indicate the existence of multiple radial eigenmodes. In the context of the quantum mechanical analogy discussed in Sec. 3.2, these eigenmodes correspond to different bound states in the potential well.

Larger values of α correspond to the dense plasma regime. In this case, the

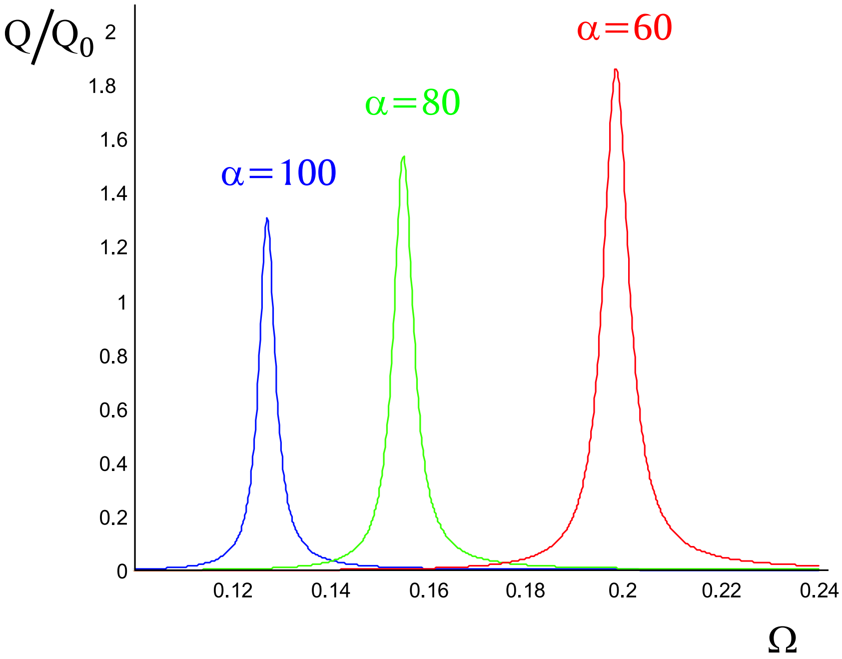

Figure 3.3: Plasma power absorption in the dense plasma for the harmonic with $m = 1$. There are additional absorption peaks with lower amplitudes at higher values of Ω.

peak plasma power absorption decreases with plasma density (see Fig. 3.3). We took $\nu_0 = 0.02$ for all the runs. The power absorption peaks in Fig. 3.3 represent a mode with the lowest possible frequency for a given α, which is analogous to the mode described by Eq. (3.36). In agreement with Eq. (3.36), the frequency of the mode in Fig. 3.3 scales roughly as $1/\alpha$.

Finally, we compare peak power absorption for two harmonics with different azimuthal wave numbers. Figure 3.4 presents power absorption spectra for $m = 1$ and $m = 2$. The values of $\alpha = 20$ and normalized collision frequency $\nu_0 = 0.02$ are the same in both cases. The mode with $m = 1$ couples to the antenna better than the mode with $m = 2$, since the field drops towards the antenna slower for $m = 1$ than for $m = 2$ [see Eq. (3.35)]. This explains the higher level of plasma power absorption for $m = 1$.

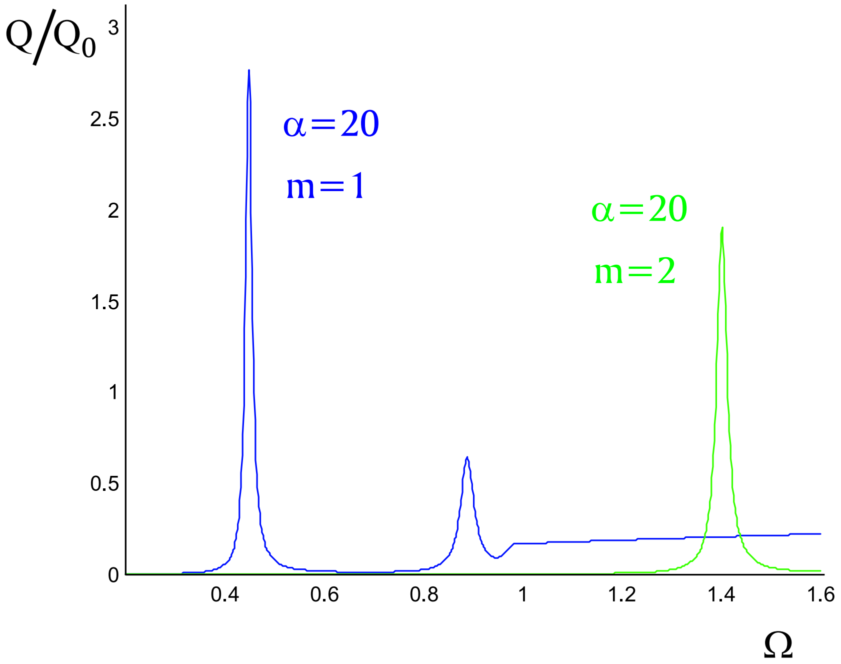

Figure 3.4: Plasma power absorption for the harmonics with $m = 1$ and $m = 2$ for the same plasma density profile.

3.5 Concluding Discussion

Although the modes described by Eqs. (3.30), (3.36), and (3.41) are radially localized modes with distinct surface-wave features, their coupling to the antenna current in helicon plasma sources can be sufficiently strong, especially for $|m| = 1$, a typical mode number for such devices. Note that these modes are asymmetric with respect to the change of sign of m or $\mathbf{B}_0$ separately. However, the mode frequency does not change when the signs of m and $\mathbf{B}_0$ change simultaneously. The asymmetry, which results from the Hall effect in nonuniform plasma, may cause significant changes in the operation of helicon sources with the change of the magnetic field sign. A related phenomenon is the co-counter asymmetry in fast wave heating and current drive (see Ref. [14]).

It should be possible to clearly identify the described modes in a well diagnosed experiment similar to the one reported in Refs. [15, 16], where helicon modes were observed in a homogeneous plasma. This will of course require a plasma with controllable radial density gradient.

It follows from the structure of Eq. (3.30) that an externally driven solution for $E(r)$ is regular at the points where the denominator on the right-hand side of this equation vanishes. A straightforward analysis shows that the function $E(r)$ remains finite at these points. However, with finite value of E, Eq. (3.29) exhibits a singularity in the parallel electric field, which in turn suggests a resonant-type absorption of the rf power near the singularity. It is plausible that such an absorption is responsible for unusually high efficiency of the helicon sources, especially at frequencies below the typical helicon frequency for a uniform plasma. It should be emphasized that this absorption mechanism is qualitatively different from the one discussed in Refs. [9, 17], where the enhanced absorption was attributed to linear coupling between the helicon and the Gould-Trivelpiece modes. In our case, the absorption results from the surface-type helicon mode alone, which is actually decoupled from the Gould-Trivelpiece mode described by Eq. (3.31). The particularly low frequency of the localized modes translates into their low phase velocity, which should facilitate Landau damping of these modes. Although we assumed that Landau damping is low for the discussed modes, it still will be much greater than that for the conventional helicons due to the significant difference in the phase velocity. Therefore, these new modes may provide an enhanced power deposition into the helicon discharge.

Chapter 4

Self-consistent Modelling of Helicon Plasma Sources

4.1 Introduction

This chapter presents a first-principle theory for helicon plasma sources in light gases with a self-consistent treatment of the *particle balance*, *power balance*, and *rf-field structure*. The theory addresses the mystery of high efficiency of the helicon sources at frequencies below the typical helicon frequency. The theory deals primarily with basic physics aspects, so that some of the issues discussed below are not unique to helicon sources. For example, the problem of finding ion conductivity in the presence of charge-exchange and elastic ion-neutral collisions from Sec. 4.5 can be viewed as a stand-alone problem of general interest.

In what follows, we will consider a schematic layout shown in Fig. 4.1. We will assume that the plasma is created via rf-discharge inside an axisymmetric dielectric tube placed in a uniform axial magnetic field (B_0). The tube length (L) is much greater than the radius (a). One end of the tube is sealed by an emissive metal plate with an opening for gas injection. The other end is open into a vacuum to allow free plasma flow out of the source.

We will limit our consideration to the case of rarified gas with the particle mean free path larger than the tube radius. A Knudsen-type gas flow will then establish itself in the tube in the absence of plasma. The gas density in this flow is uniform over the tube cross-section and decreases linearly from its maximum value at the end-plate to nearly zero at the open end. We will assume that the gas is monatomic

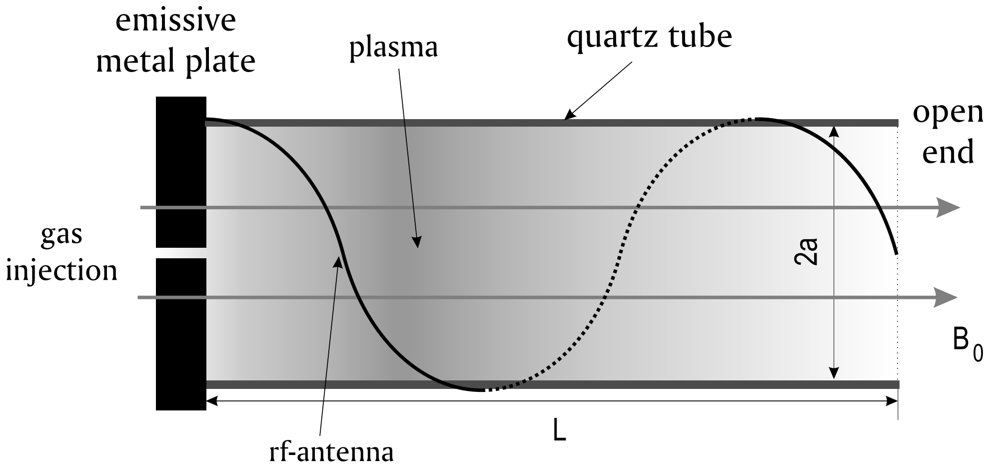

Figure 4.1: Schematic layout of magnetized plasma source.

and that the degree of ionization is small in the rf-discharge. The latter will allow us to neglect any plasma effect on *the gas density profile.* We will however be able to describe an increase in *the gas pressure* associated with fast charge-exchange neutrals (see Sec. 4.9).

A model of helicon plasma source should incorporate three major components, which are *particle balance*, *power balance*, and *rf-field structure.* A natural separation of scales in the helicon source among the particle confinement time τ_p, the energy confinement time τ_E, and the wave period $2\pi/\omega$ (ω is the wave frequency),

$$\tau_p \gg \tau_E \gg 2\pi/\omega, \tag{4.1}$$

allows one to first consider all three constituents separately and then integrate them into a self-consistent model. The rf-field structure inside the helicon source has been analyzed in Chapter 2 and this chapter completes the analysis with the particle and power balance pieces.

The *particle balance* problem is essentially a kinetic problem of ion transport. The ion motion in the discharge is controlled by: (1) ambipolar electric field resulting from quasineutrality; (2) equilibrium magnetic field; (3) ion collisions with atoms. As the ion density is small compared to the gas density, we neglect ion-ion collisions compared to ion-atom collisions. The ion density profile is generally nonuniform in both longitudinal and radial directions since the ions are confined radially by the magnetic field. As a result, the ambipolar electric field, associated with the ion density gradient, has both longitudinal and radial components.

The *rf-power* in the helicon source is absorbed by the plasma electrons and thus electron physics is the main ingredient of the *power balance* problem. The electron distribution is Maxwellian, provided that the energy confinement time τ_E exceeds the time between electron-electron collisions, i.e.

$$\tau_E \nu_{ee} \gg 1, \tag{4.2}$$

where ν_{ee} is the electron-electron collision frequency. The electron temperature is determined by an energy balance condition involving electron heating by rf-field, electron heat conduction, and energy losses on atom excitation.

We assume that the rf-power deposition is associated with the excitation of the radially localized helicon waves [29] by the external rf-antenna. We will calculate the rf-field structure using the corresponding wave equation derived in Chapter 2, but with a self-consistent plasma density profile. Simultaneous solution of the power balance problem, particle balance problem, and the wave equation allows us to find the steady-state density and temperature profiles, as well as the rf-field structure. The described self-consistent model also enables us to discuss the stability of the discharge.

The rest of the chapter is organized as follows. Section 4.2 presents a qualitative discussion of ion transport and simple estimates for the longitudinal and radial particle fluxes and the corresponding confinement-times. Section 4.3 presents a qualitative picture of the power balance and an estimate of the energy confinement time and characteristic electron heating times. Section 4.4 qualitatively discusses the steady-state regime and the way a stable equilibrium can be established in the discharge, based on a "zero-dimensional" model. Section 4.5 presents a derivation of the gyro-averaged ion distribution function in presence of an ambipolar electric field and ion-atom charge-exchange and elastic collisions. This solution allows us to quantitatively evaluate ion fluxes. In Sec. 4.6, a first-principle theoretical model for helicon discharge with a self-consistent treatment of the particle balance, power balance, and rf-field structure is presented. In Sec. 4.7, the density profiles in steady-state plasma flows are calculated. Here, the limiting cases of longitudinal and radial losses are considered. Also, the conditions under which a steady-state is allowed are formulated. Section 4.8 presents a one-dimensional numerical model for a helicon discharge with predominantly radial ion flow based on the theoretical model developed in Sec. 4.6. Finally, in Sec. 4.9, the limitations of the model and some implications of the results are discussed.

4.2 Qualitative Estimates of the Ion Transport

Ion transport in the discharge is controlled by equilibrium magnetic field, ambipolar electric field, and ion-atom collisions. The equilibrium magnetic field is typically strong enough to magnetize the ions, so that the following two conditions are satisfied:

$$\rho_{Li} \ll a, \tag{4.3a}$$

$$\nu_{ia} \ll \omega_{ci}, \tag{4.3b}$$

where ρ_{Li} is the ion gyro-radius, a is the plasma radius, ν_{ia} is the ion-atom collision frequency, and ω_{ci} is the ion gyro-frequency. The longitudinal and radial ion transport are significantly different under these conditions.

The charge-exchange and elastic collisions are the dominant ion-atom collision processes for ion energies up to few eV [26, 32]. In terms of energy and momentum conservation, charge-exchange collisions are essentially equivalent to head-on elastic collisions. Both the charge-exchange cross-section (σ_{cx}) and the elastic cross-section (σ_{el}) are nearly constant in the energy range of interest and they are of the same order of magnitude [26, 32]. We will assume that the gas temperature is much lower than the characteristic ion energy. In this case, the ions lose a significant part of their kinetic energy in each collision. The ion-atom collision frequency is given by

$$\nu_{ia} = n_0 v(\sigma_{cx} + \sigma_{el}), \tag{4.4}$$

where n_0 is the gas density and v is ion velocity. The characteristic velocity in Eq. (4.4) can be estimated as the ion velocity gain in the ambipolar electric field $\mathbf{E}^a$ between two collisions. The velocity gain in the direction of the magnetic field ($v_\parallel$) is roughly

$$v_\parallel \approx \frac{|e|E^a_\parallel}{m_i \nu}. \tag{4.5}$$

The transverse velocity gain for magnetized ions ($v_\perp$) is of the order of the $\mathbf{E}\times\mathbf{B}$-drift velocity ($u_E$):

$$v_\perp \approx u_E \equiv \frac{|e|E^a_r}{m_i \omega_{ci}}. \tag{4.6}$$

Assuming that the longitudinal and radial scale-lengths of the plasma density profile are L and a, respectively; we estimate $E^a_\parallel$ and E^a_r as

$$E^a_\parallel \approx \frac{T_e}{|e|L}, \tag{4.7a}$$

$$E^a_r \approx \frac{T_e}{|e|a}, \tag{4.7b}$$

where T_e is the bulk electron temperature. We now combine Eqs. (4.4)-(4.7) into

$$\nu_{ia} = n_0(\sigma_{cx} + \sigma_{el})\sqrt{v_\parallel^2 + v_\perp^2} \approx n_0(\sigma_{cx} + \sigma_{el}) C_s \sqrt{\frac{C_s^2}{\nu_{ia}^2 L^2} + \frac{C_s^2}{\omega_{ci}^2 a^2}}, \tag{4.8}$$

where $C_s \equiv \sqrt{T_e/m_i}$ is the ion sound velocity. This estimate for ν_{ia} can be approximated by the expression

$$\nu_{ia} \approx \xi(\xi + 1)\frac{a\omega_{ci}}{L}, \tag{4.9}$$

with

$$\xi \equiv \frac{C_s}{a\omega_{ci}}\sqrt{n_0 L(\sigma_{cx}+\sigma_{el})}. \tag{4.10}$$

We will now show that the parameter ξ characterizes the ratio between the radial and longitudinal ion fluxes. The mechanism of radial transport is shown schematically in Fig. 4.2. An initially slow ion is accelerated by the radial ambipolar electric field until its velocity becomes comparable to the drift velocity u_E. Between collisions, the ion drifts in the azimuthal direction and oscillates radially with the radial orbit excursion of the order of $\rho_{Li} \approx u_E/\omega_{ci}$. Every collision replaces the accelerated ion by a slow ion. This effectively shifts the ion orbit in the direction of the ambipolar electric field by ρ_{Li}. The average radial flow velocity, therefore, can be estimated as

$$u_\perp \approx \nu_{ia}\rho_{Li} \approx \frac{|e|E_r^a}{m_i\nu_{ia}}\frac{\nu_{ia}^2}{\omega_{ci}^2}. \tag{4.11}$$

The ensuing expressions for the total radial flux ($\psi_\perp$) and the radial confinement time ($\tau_\perp$) are

$$\psi_\perp \approx n u_\perp a L \approx \xi(\xi+1) n a^2 C_s \frac{C_s}{a\omega_{ci}}, \tag{4.12a}$$

$$\tau_\perp \approx a/u_\perp \approx \frac{L}{\xi(\xi+1)C_s}\frac{a\omega_{ci}}{C_s}. \tag{4.12b}$$

Here we assume that the conducting end-plate allows a sufficient current to flow across the field lines to neutralize the ion space-charge as the ions move radially. Otherwise, the velocity of radial plasma flux would be limited by electrons [27] due to low electron conductivity across the field lines. This would also change the estimate (4.7b) for the radial electric field.

The longitudinal ion flux ($\psi_\parallel$) and the longitudinal confinement time ($\tau_\parallel$) are readily estimated from Eqs. (4.5), (4.7a), and (4.9):

$$\psi_\parallel \approx n v_\parallel a^2 \approx \frac{n a^2 C_s}{\xi(\xi+1)}\frac{C_s}{a\omega_{ci}}, \tag{4.13a}$$

$$\tau_\parallel \equiv \frac{L}{v_\parallel} \approx \xi(\xi+1)\frac{L}{C_s}\frac{a\omega_{ci}}{C_s}. \tag{4.13b}$$

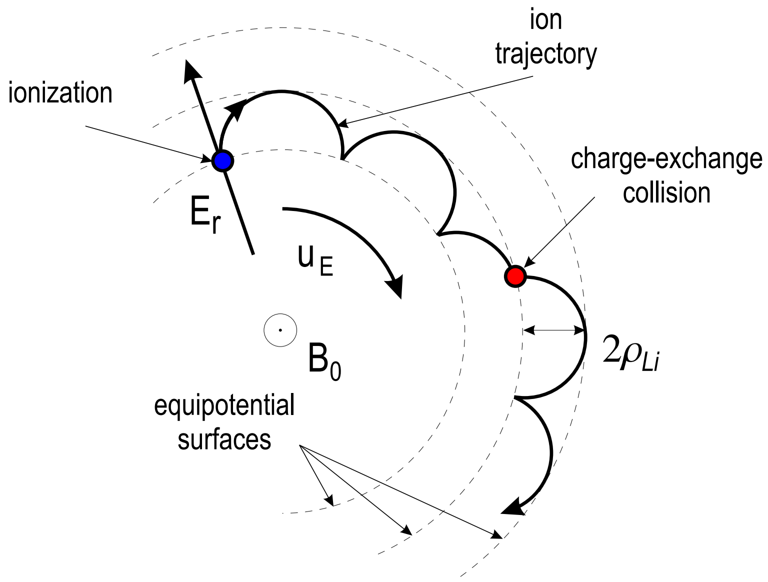

Figure 4.2: Ion transport across the magnetic field.

It follows from Eqs. (4.12) and (4.13) that the ratio between the total longitudinal and radial ion fluxes is given by

$$\frac{\psi_\perp}{\psi_\parallel} = \frac{\tau_\parallel}{\tau_\perp} = \xi^2(\xi+1)^2. \tag{4.14}$$

We thus conclude that the longitudinal transport prevails when ξ is much smaller than unity, whereas the case $\xi \gg 1$ corresponds to predominantly radial transport.

4.3 Qualitative Picture of the Power Balance

The *power balance* in helicon plasma sources is established by the plasma electrons. The mechanism is shown schematically in Fig. 4.3. The power is supplied by the external rf-antenna generating the rf-field and this power is absorbed by the plasma electrons. The main power loss mechanism is the line-radiation. Plasma electrons lose their energy exciting the background gas atoms in inelastic collisions. Then the excited atoms emit photons that leave the plasma carrying away the energy.

The process of electron heating resembles diffusion in the velocity space as the electrons oscillate in the rf-field. In order to qualitatively illustrate the underlying

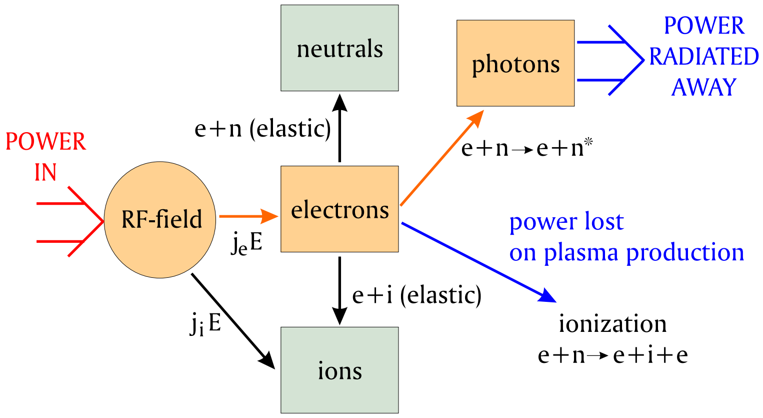

Figure 4.3: Schematic picture of the power redistribution in a helicon source. In equilibrium, the deposited power is balanced by the line-radiation. Single red arrows stand for the key channel of the power transformation.

mechanism, we consider one-dimensional electron oscillations along the magnetic field lines in the presence of the elastic collisions with ions and neutrals. The electron-electron (e-e) collisions will be neglected at this point since they conserve the total momentum of the electron population. However, the e-e collisions are important for establishing the electron energy distribution and their role will be considered later in this section. Every elastic collision with an ion or neutral changes the sign of V_z not changing the absolute value (the energy transfer to the ions and neutrals can be neglected if the right-most inequality in Eq. (4.20) is satisfied). The evolution of V_z due to the collisions is shown in Fig. 4.4. We assume that $\omega \gg (\nu_{ei}+\nu_{en})$, where ν_{ei} and ν_{en} are the electron-ion and electron-neutral collision frequencies respectively. Then the electron velocity averaged over the wave period, $\langle V_z \rangle$, is almost constant between the collisions. Every collision changes $\langle V_z \rangle$ roughly by $|\tilde{V}_z|$, where $\tilde{V}_z \approx eE_z/m_e\omega$ is the amplitude of the velocity oscillations along the magnetic field lines in the rf-field with amplitude E_z and frequency ω. Since the collisions are not correlated with the field oscillations, the evolution of $\langle V_z \rangle$ is similar to a one-dimensional random walk with $\langle V_z \rangle$ corresponding to the displacement, $|\tilde{V}_z|$ corresponding to the step size, and $1/(\nu_{ei} + \nu_{en})$ corresponding to the time interval between the steps. The diffusion

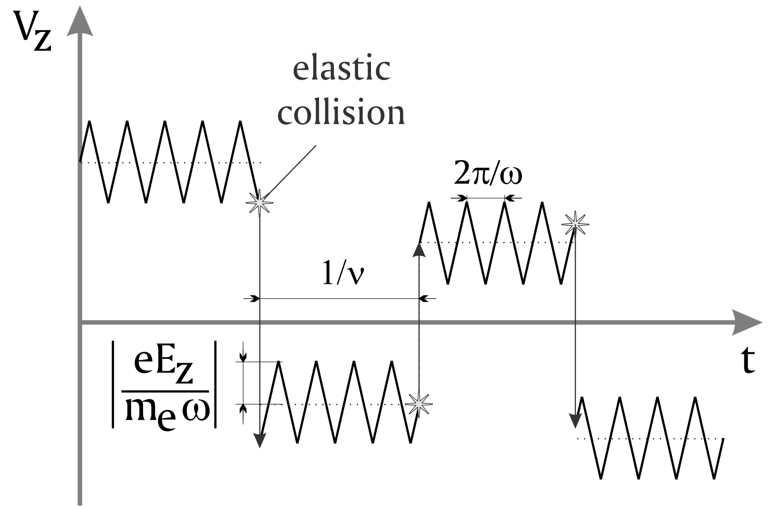

Figure 4.4: Mechanism of electron heating by the rf-field with amplitude E_z and frequency ω due to elastic collisions. The velocity oscillations are produced by the rf-field. The elastic collisions change only the sign of V_z. Dashed lines show the electron velocity between the collisions averaged over the wave period.

coefficient describing the rf-heating in the velocity space can be estimated as:

$$D_{\|} \approx (\nu_{en} + \nu_{ei}) \left(\frac{eE_z}{m_e \omega} \right)^2 . \tag{4.15}$$

The mechanism of the electron heating by the rf-field transverse to the magnetic field lines is similar. The electrons are magnetized ($\omega \ll \omega_{ce}$), so that the amplitude of the velocity oscillations $\tilde{V}_\perp$ across the field lines in the rf-field with amplitude $E_\perp$ is estimated as $\tilde{V}_\perp \approx eE_\perp / m_e \omega_{ce}$. Then the corresponding diffusion coefficient is given by:

$$D_\perp \approx (\nu_{en} + \nu_{ei}) \left(\frac{eE_\perp}{m_e \omega_{ce}} \right)^2 . \tag{4.16}$$

However, the coefficient $D_{\|}$ is much larger than $D_\perp$ for the radially localized helicon waves and, as a result, the rf-heating by the transverse components of the wave field is not important. In order to demonstrate this, we first note that both transverse components of the wave field E_r and E_ϕ are of the same magnitude [see Eq. (3.23)], which we denote as $E_\perp$. Assuming that the plasma density changes on a spatial scale comparable to the tube radius a, we obtain from Eqs. (3.27) and (3.29), which relate

E_r and E_ϕ to E_z, the following estimate:

$$E_\perp \approx \frac{\eta}{g} k_z a E_z. \tag{4.17}$$

Then using expressions (3.16) for g and η and neglecting the small collision terms, we find that

$$\frac{E_\perp}{\omega_{ce}} \approx (k_z a) \frac{E_z}{\omega}. \tag{4.18}$$

Note that the longitudinal wave number k_z is assumed to be sufficiently small for the radially localized helicon waves [see Eq. (3.1)]: $k_z a \ll 1$. It then immediately follows from Eqs. (4.15) and (4.16) that

$$\frac{D_\perp}{D_\parallel} \approx k_z a \ll 1. \tag{4.19}$$

The elastic e-i and e-n collisions make the electron velocity distribution isotropic on a time scale $1/(\nu_{ei} + \nu_{en})$, so that the rf-heating by a transverse or longitudinal field produces an isotropic electron distribution. Therefore, the electron heating by the rf-field with transverse and longitudinal components can be considered as diffusion with diffusion coefficient $(D_\parallel + D_\perp)$ in the velocity space. However, as indicated by Eq. (4.19), the rf-heating by $E_\perp$ is much slower than the heating by E_z and thus it can be neglected.

We now formulate the applicability condition for the “diffusive” picture of the electron heating. We denote the characteristic electron energy as T_e. In every elastic collision, the electron energy changes roughly by $m_e \tilde{V}_z^2/2$. On one hand, this energy must be much larger than the energy transferred during the impact from the electron to the ion or neutral. Since the ions and neutrals are much colder than the electrons, the transferred energy can be estimated as $m_e T_e / m_i$. On the other hand, the electron heating has the diffusive character in the velocity space if $m_e \tilde{V}_z^2/2$ is much smaller than T_e. Then the applicability condition takes the form:

$$1 \gg \frac{m_e}{2T_e} \left(\frac{eE_z}{m_e \omega} \right)^2 \gg \frac{m_e}{m_i}, \tag{4.20}$$

where we took into account that $\tilde{V}_z \approx eE_z/m_e\omega$. Finally, we note that even though we assumed above that the collision frequencies ν_{ei} and ν_{en} are much smaller than the wave frequency, the "diffusive" picture of the electron heating is valid as long as condition,

$$\omega \gtrsim (\nu_{en} + \nu_{ei}), \tag{4.21}$$

is satisfied.

The electron energy distribution is formed not only by the electron-neutral (e-n) and electron-ion (e-i) elastic collisions, but also by the electron-electron collisions. The elastic e-i and e-n collisions establish the equilibrium distribution on a time scale that can be estimated as a characteristic electron heating time from zero energy up to T_e:

$$\tau_H \approx \frac{T_e}{m_e D_\parallel}. \tag{4.22}$$

The e-e collisions establish the equilibrium distribution on a time scale roughly estimated as $1/\nu_{ee}$. If the condition,

$$\tau_H \nu_{ee} \gg 1, \tag{4.23}$$

is satisfied, then the electron distribution is Maxwellian with temperature T_e. For a wide range of parameters the condition (4.23) is satisfied in helicon sources and we will assume the plasma electrons to be Maxwellian for the rest of this chapter. Note that left inequality in Eq. (4.20) insures that the oscillating part of the electron distribution associated with the rf-field is a small correction to the Maxwellian distribution.

We can now estimate the electron energy confinement time τ_E under the assumption that the electrons lose their energy exciting the background gas atoms. Only electrons with energy above the excitation threshold energy ε_{exc} can excite the atoms via collisions. Their density is given by $n \exp(-\varepsilon_{exc}/T_e)$. The characteristic time needed for an electron moving through the background gas with velocity

$\sqrt{\varepsilon_{exc}/m_e}$ to produce an excited atom is $\left[\sigma_{exc} n_0 \sqrt{\varepsilon_{exc}/m_e}\right]^{-1}$, where σ_{exc} is the excitation cross-section. Therefore, plasma electrons lose energy (per unit volume) at the rate

$$\varepsilon_{exc} n \mathrm{e}^{-\varepsilon_{exc}/T_e} \left[\sigma_{exc} n_0 \sqrt{\frac{\varepsilon_{exc}}{m_e}}\right]. \tag{4.24}$$

Since the total electron energy per unit volume is nT_e, then the energy confinement time can be estimated as:

$$\tau_E \approx \frac{T_e}{\varepsilon_{exc}} \mathrm{e}^{\varepsilon_{exc}/T_e} \left[\sigma_{exc} n_0 \sqrt{\frac{\varepsilon_{exc}}{m_e}}\right]^{-1}. \tag{4.25}$$

In equilibrium, electron energy losses are balanced by the rf-heating, which implies that

$$\tau_H = \tau_E.$$

This condition determines the equilibrium electron temperature.

In a similar fashion we can estimate the time required for Maxwellian electrons to produce a plasma with density n by ionizing the background gas:

$$\tau_{ion} \approx \mathrm{e}^{\varepsilon_{ion}/T_e} \left[\sigma_{ion} n_0 \sqrt{\frac{\varepsilon_{ion}}{m_e}}\right]^{-1}. \tag{4.26}$$

Here σ_{ion} is the ionization cross-section and ε_{ion} is the ionization threshold energy. In the equilibrium, plasma production is balanced by plasma losses, so that

$$\tau_{ion} = \tau_p, \tag{4.27}$$

where τ_p is the particle confinement time.

In helicon plasma sources, the particle confinement time significantly exceeds the energy confinement time:

$$\tau_p \gg \tau_E. \tag{4.28}$$

In terms of electron temperature this implies that

$$T_e \ll \varepsilon_{exc}. \tag{4.29}$$

Indeed, if $T_e \ll \varepsilon_{exc}$, then it follows directly from Eqs. (4.25) - (4.27) that

$$\frac{\tau_p}{\tau_E} \approx \left(\frac{\varepsilon_{ion}}{\varepsilon_{exc}}\right)^{3/2} \frac{\varepsilon_{exc}}{T_e} \exp\left(\frac{\varepsilon_{ion} - \varepsilon_{exc}}{T_e}\right) \gg 1. \tag{4.30}$$

Here the cross-sections σ_{ion} and σ_{exc} were approximated as:

$$\sigma_{ion} \approx \frac{\pi e^4}{\varepsilon_{ion}^2}, \;\; \sigma_{exc} \approx \frac{\pi e^4}{\varepsilon_{exc}^2}. \tag{4.31}$$

To conclude this section, we review the key conditions that guarantee the validity of the power balance picture discussed above and illustrated in Fig. 4.3. We have assumed that the rf-power is mainly absorbed by the electrons and not ions. The condition (3.15) implies that the ion response to the rf-field is weak compared to the electron response. If, in addition to this, the ion collision frequency is not much higher than $(\nu_{ei} + \nu_{en})$, then the power absorption by the ions is insignificant. The power losses on ionization are smaller than the power losses on excitation [see Eq. (4.24)] if the following condition is satisfied:

$$\sqrt{\frac{\varepsilon_{exc}}{\varepsilon_{ion}}} \exp\left[-\frac{\varepsilon_{ion} - \varepsilon_{exc}}{T_e}\right] < 1. \tag{4.32}$$

The electrons lose their energy ionizing the atoms (per unit volume) at the rate

$$\varepsilon_{ion} n \mathrm{e}^{-\varepsilon_{ion}/T_e} \left[\sigma_{ion} n_0 \sqrt{\frac{\varepsilon_{ion}}{m_e}}\right]. \tag{4.33}$$

The power losses due to the electron transport, roughly estimated as nT_e/τ_p, are negligible compared to the power losses on excitation (nT_e/τ_E) as a direct consequence of the condition (4.28). The power dissipated by the electrons during elastic collisions with ions and neutrals is much smaller than the rf-power absorbed by the electrons due to the right-most inequality in Eq. (4.20). Therefore, the rf-heating can be balanced only by the energy losses on excitation.

4.4 Qualitative Picture of the Steady-state Regime

This section presents a qualitative discussion of the steady-state regime and the way it can be established. The picture developed here will be used to formulate a one-dimensional model for a source with predominantly radial plasma flow.

In the axisymmetric case, the density profile $n(r, z, t)$ fully describes the system at each moment. The evolution of an initial density profile is described by the continuity equation, which involves the electron temperature. The corresponding electron temperature profile $T_e(r, z, t)$ is in turn determined from the steady-state power balance equation. In this section, we consider a simpler "zero-dimensional" model [28]. This means that we assume that the state of the system at each moment can be described by a characteristic plasma density n, which is just a single number, and that there is a characteristic electron temperature T_e corresponding to it. Then the possible states of the system are given in (T_e, n)-plane by a curve $T_e(n)$ determined by the power balance condition. The power balance is established on a time scale smaller than the characteristic time of the density evolution, so that the power deposited by the antenna is equal to the power lost via the line-radiation even for an instantaneous non-equilibrium density profile. It is significant that the curve $T_e(n)$ is not monotonic due to the eigenmode excitation as shown schematically in Fig. 4.5 by the solid curve.

In order to show how this curve can be calculated, we consider the following set of plasma density profiles: $n(r) = n_* G(r)$, where $G(r)$ is the same dimensionless function for all the profiles. Each of the density profiles is characterized by a single parameter n_*. The power deposited by the antenna, Q, depends on two parameters ω and n_*. In Sec. 3.4, we kept n_* fixed and performed a scan in ω to calculate the absorption curves $Q(\omega)$ for fixed values of n_* and antenna current I_0. Now we are interested in functional dependence of the power deposition on n_* with antenna

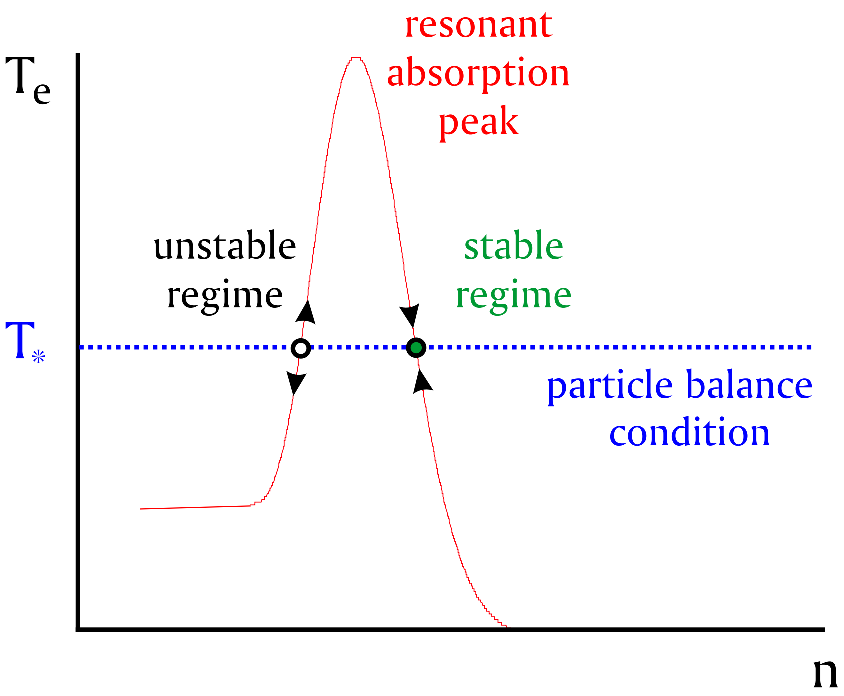

Figure 4.5: Discharge stability diagram. Solid curve $T_e(n)$ represents possible states of the system. Dashed line represents the equilibrium temperature T_* determined from the particle balance condition. The intersection points are the system equilibria. The higher density equilibrium is stable (green circle). The lower density equilibrium is unstable (white circle).

current and antenna frequency fixed. It is clear that $Q(n_*)$ must also have peaks of the resonant power absorption corresponding to the excitation of plasma eigenmodes. The power balance condition establishes a one-to-one correspondence between T_e and Q, which readily gives a resonant-type temperature dependence $T_e(n_*)$. It was shown in Sec. 3.4 that mode with the lowest frequency has the highest power absorption peak. If we limit our consideration just to this single mode, then the curve $T_e(n_*)$ will look as shown schematically in Fig. 4.5.

It follows from the solution of the continuity equation with constant T_e in Sec. 4.7, that the value of the electron temperature in a steady-state discharge is well defined and it does not depend on the value of the plasma density. For example, in the case of predominantly longitudinal plasma transport, T_e is specified by the condition (4.103) and it depends on the background gas density n_0. In the case of predominantly radial plasma transport, T_e is specified by the condition (4.111) and it depends on the equilibrium magnetic field B_0. It is important that the plasma density does not explicitly enter the conditions, so that the equilibrium temperature is independent of the density.

In Fig. 4.5 illustrating the "zero-dimensional" model, the dashed line represents the temperature T_* corresponding to the steady-state density profile and it is determined from the particle balance condition. The points of intersection of the solid curve and dashed line are the self-consistently established equilibria. While the value of T_* does not depend on the antenna current I_0, the rf-power deposition by the antenna is proportional to I_0^2 and the height of the $T_e(n)$-curve increase with I_0. Then there is a critical value of the antenna current, I_{cr}, below which no self-consistent equilibrium can be established (remember that we are considering the highest absorption peak). For I_0 exceeding I_{cr}, there are two points of intersection as shown in Fig. 4.5, i.e. two possible states of equilibrium. However, only the higher density equilibrium (green circle in Fig. 4.5) is stable, while the lower density equilibrium is unstable (white circle in Fig. 4.5).

In order to demonstrate this, consider the higher density equilibrium first. In the vicinity of the equilibrium point, the curve $T_e(n_*)$ found via the power balance condition has a negative slope $\partial T_e/\partial n_* < 0$. Therefore, if the system is in the state shifted towards the higher values of the plasma density with respect to the equilibrium point, then $T_e < T_*$. The density evolves according to the continuity equation. In the previous section, we found that the density decays if $T_e < T_*$, so that the system will move towards the equilibrium along the curve $T_e(n_*)$. If the system is in the state shifted towards the lower values of the plasma density with respect to the equilibrium point, then $T_e > T_*$ and the density grows (see subsections 4.7.1 and

4.7.2), so that the system again will move towards the equilibrium along the curve $T_e(n_*)$. This behavior is shown by arrows in Fig. 4.5. In a similar fashion one can show that the lower density equilibrium is unstable because $T_e(n_*)$ has a positive slope ($\partial T_e/\partial n_* > 0$) in the vicinity of the equilibrium point.

It follows from this discussion that the steady-state discharge operation regime corresponds to the higher density equilibrium. It is important to point out that typical antenna currents in helicon sources are in the range of I_{cr}, so that the steady-state can be achieved only due to the excitation of eigenmodes (the height of the curve $T_e(n)$ away from the resonant absorption peak is too low compared to T_*).

4.5 Ion Distribution Function and Ion Fluxes

We start from the kinetic equation for the ion distribution function f, which reads:

$$\frac{\partial f}{\partial t} + \mathbf{v}\frac{\partial f}{\partial \mathbf{r}} + \frac{|e|}{m_i}\left(\mathbf{E}^a + \frac{1}{c}[\mathbf{v}\times\mathbf{B}_0]\right)\frac{\partial f}{\partial \mathbf{v}} = St(f) + \delta(\mathbf{v})nn_0\left\langle\sigma_{ion}v\right\rangle_e, \tag{4.34}$$

where $\mathbf{E}^a$ is the ambipolar electric field and

$$\begin{aligned} St(f) \;\equiv\;& n_0\sigma_{cx}\left(\delta(\mathbf{v})\int v' f d^3\mathbf{v}' - vf\right) \\ &+ n_0\sigma_{el}\left(\frac{1}{\pi}\int \delta(v^2 - \mathbf{v}\cdot\mathbf{v}')fd^3\mathbf{v}' - vf\right). \end{aligned} \tag{4.35}$$

The collision operator $St(f)$ includes the charge-exchange (cx) and elastic (el) collisions. The term $\delta(\mathbf{v})nn_0\left\langle\sigma_{ion}v\right\rangle_e$ describes gas ionization by electron impact at the rate $\left\langle\sigma_{ion}v\right\rangle_e$. The charge-exchange process "takes the ions away" at a rate $\sigma_{cx}v$ and returns them to the ion distribution at zero velocity. Elastic collisions "take the ions away" at a rate $\sigma_{el}v$ and return them isotropically distributed in the center of mass reference frame. As already pointed out in Sec. 4.2, we can treat the cross-sections σ_{cx} and σ_{el} as constants since they are insensitive to the ion energy in the relevant energy range of up to few eV.

In order to solve Eq. (4.34), we will assume the following ordering

$$\omega_{ci} \gg n_0(\sigma_{cx} + \sigma_{el})v \gg n_0 \left\langle \sigma_{ion} v \right\rangle_e \sim 1/\tau, \tag{4.36}$$

where τ is the characteristic discharge time. We also assume that

$$\rho_{Li} \ll a, \qquad\qquad \lambda \equiv \frac{1}{n_0(\sigma_{cx} + \sigma_{el})} \ll L. \tag{4.37}$$

These assumptions allow us to neglect, to lowest order, the spatial and time derivatives of f in Eq. (4.34) as well as the “ionization” term in the collision operator (4.35). As a result, Eq. (4.34) reduces to

$$\begin{aligned} \frac{|e|}{m_i}\left(\mathbf{E}^a + \frac{1}{c}[\mathbf{v} \times \mathbf{B}_0]\right)\frac{\partial f}{\partial \mathbf{v}} &= n_0\sigma_{cx}\left(\delta(\mathbf{v})\int v' f d^3\mathbf{v}' - vf\right) \\ &+ n_0\sigma_{el}\left(\frac{1}{\pi}\int \delta(v^2 - \mathbf{v}\cdot\mathbf{v}')fd^3\mathbf{v}' - vf\right). \end{aligned} \tag{4.38}$$

It should be noted that this equation automatically conserves the number of particles since both its left-hand side and its right-hand side vanish after integration over the velocity space. The distribution function f is normalized by the relation:

$$\int f d^3\mathbf{v} = n, \tag{4.39}$$

where n is the plasma density. The particle balance condition, obtained by velocity integration of Eq. (4.34), gives a continuity equation for n:

$$\frac{\partial n}{\partial t} + \frac{1}{r}\frac{\partial}{\partial r}(rj_r) + \frac{\partial j_z}{\partial z} = nn_0 \left\langle \sigma_{ion} v \right\rangle_e, \tag{4.40}$$

where

$$j_r = \int f v_r d^3\mathbf{v}, \tag{4.41a}$$

$$j_z = \int f v_z d^3\mathbf{v}, \tag{4.41b}$$

and (r, φ, z) are cylindrical coordinates with the z-axis pointing in the direction of the magnetic field $\mathbf{B}_0$.

It should be noted that the radial ion flux j_r is related to the ion-neutral friction force by the momentum balance condition. We will see that this relationship simplifies the calculation of j_r considerably. The momentum balance condition has the form

$$\begin{aligned} -\frac{|e|}{m_i}\left(n\mathbf{E}^a + \frac{1}{c}[\mathbf{j}\times\mathbf{B}_0]\right) &= -n_0(\sigma_{cx}+\sigma_{el})\int \mathbf{v}vf(\mathbf{v})d^3\mathbf{v} \\ &+ \frac{n_0\sigma_{el}}{\pi}\int \mathbf{v}d^3\mathbf{v}\int \delta(v^2-\mathbf{v}\cdot\mathbf{v}')f(\mathbf{v}')d^3\mathbf{v}', \quad (4.42) \end{aligned}$$

that can be obtained by integrating both sides of Eq. (4.38) over the velocity space with a multiplier $\mathbf{v}$. The φ-component of Eq. (4.42) gives

$$j_r = -\frac{n_0(\sigma_{cx}+\sigma_{el})}{\omega_{ci}}\int v_\varphi vf(\mathbf{v})d^3\mathbf{v} + \frac{n_0\sigma_{el}}{\pi\omega_{ci}}\int K_\varphi(\mathbf{v}')f(\mathbf{v}')d^3\mathbf{v}', \quad (4.43)$$

where

$$\mathbf{K}(\mathbf{v}') \equiv \int \delta(v^2-\mathbf{v}\cdot\mathbf{v}')\mathbf{v}d^3\mathbf{v}. \quad (4.44)$$

We note that the vector $\mathbf{K}$ is necessarily parallel to $\mathbf{v}'$, the only preferred direction in Eq. (4.44). We can therefore put

$$\mathbf{K} = \alpha\mathbf{v}', \quad (4.45)$$

with

$$\alpha = \frac{1}{v'^2}\int \delta(v^2-\mathbf{v}\cdot\mathbf{v}')\mathbf{v}\cdot\mathbf{v}'d^3\mathbf{v}. \quad (4.46)$$

It is convenient to use spherical coordinates with the symmetry axis along $\mathbf{v}'$ to perform integration in Eq. (4.46):

$$\alpha = \frac{2\pi}{v'}\int_0^\infty v^3dv\int_0^\pi \delta(v^2-vv'\cos\theta)\cos\theta\sin\theta d\theta = \frac{2\pi}{v'^3}\int_0^{v'} v^3dv = \frac{\pi v'}{2}. \quad (4.47)$$

Equations (4.43)-(4.46) combine into the following expression for j_r that we will later use instead of Eq. (4.41a):

$$j_r = -\frac{n_0(2\sigma_{cx}+\sigma_{el})}{2\omega_{ci}}\int v_\varphi vfd^3\mathbf{v}. \quad (4.48)$$

We now return to Eq. (4.38) and transform it to a reference frame that moves with the $\mathbf{E}\times\mathbf{B}$-drift velocity

$$\mathbf{u}_E \equiv \mathbf{e}_\varphi u_E = -\mathbf{e}_\varphi \frac{|e|E_r^a}{m_i\omega_{ci}}. \tag{4.49}$$

This transformation conveniently eliminates the term $E_r^a \partial f/\partial v_r$ from the left-hand side of Eq. (4.38). We normalize the velocity to $|u_E|$, so that

$$\begin{aligned} v_r &= |u_E| V_\perp \cos\psi, && (4.50)\\ v_\varphi &= |u_E| V_\perp \sin\psi + u_E, && (4.51)\\ v_z &= \frac{E_\parallel^a}{|E_\parallel^a|}|u_E| V_z, && (4.52) \end{aligned}$$

where $(V_\perp, \psi, V_z)$ are dimensionless cylindrical velocity-space variables. In these new variables, Eq. (4.38) takes the form

$$\begin{aligned} &- \frac{1}{\xi^2}\frac{\omega_{ci}}{|\omega_{ci}|}\frac{|E_r^a|}{|E_\parallel^a|}\frac{\partial f}{\partial \psi} = -\frac{1}{\xi^2}\frac{\partial f}{\partial V_z} - \left(1 + V^2 + 2\frac{u_E}{|u_E|}V_\perp \sin\psi\right)^{1/2} f \\ &+ \frac{\sigma_{el}}{\pi(\sigma_{cx}+\sigma_{el})}\int V_\perp' dV_\perp' d\psi' dV_z' f(\mathbf{V}') \\ &\times \delta\left[V_\perp^2 + V_z^2 + \frac{u_E}{|u_E|}(V_\perp \sin\psi - V_\perp' \sin\psi') - V_z V_z' - V_\perp V_\perp' \cos(\psi - \psi')\right] \\ &+ \frac{\sigma_{cx}}{\sigma_{cx}+\sigma_{el}}\delta(V_\perp\cos\psi)\delta\left(V_\perp \sin\psi + \frac{u_E}{|u_E|}\right)\delta(V_z) \\ &\times \int\left(1 + V_\perp'^2 + V_z'^2 + 2\frac{u_E}{|u_E|}V_\perp'\sin\psi'\right)^{1/2} f(\mathbf{V}')V_\perp' dV_\perp' d\psi' dV_z', \end{aligned} \tag{4.53}$$

where

$$\xi \equiv \left[n_0(\sigma_{cx}+\sigma_{el})\frac{m_i u_E^2}{|eE_\parallel^a|}\right]^{1/2}. \tag{4.54}$$

Note that this definition of ξ agrees with that of Eq. (4.10) if we use estimates for $E_\parallel^a$ and E_r^a given by Eq. (4.7).

In accordance with the ordering given by Eq. (4.36), we represent f as:

$$f = f_0 + f_1, \tag{4.55}$$

where f_0 is the gyro-averaged distribution function and f_1 is a small ψ-dependent correction that is higher order in $1/\omega_{ci}$. We note that we would need f_1 to calculate j_r from Eq. (4.41a). However, f_0 is actually sufficient to calculate both j_z and j_r if we use Eq. (4.41b) for j_z and Eq. (4.48) instead of (4.41a) for j_r. We then obtain

$$\begin{aligned} j_z &= 2\pi u_E^4 \frac{E_\parallel^a}{|E_\parallel^a|} \int V_z f_0(V_\perp; V_z) V_\perp dV_\perp dV_z, && (4.56) \\ j_r &= u_E^4 \xi^2 \frac{|E_\parallel^a|}{E_r^a} \frac{2\sigma_{cx} + \sigma_{el}}{2(\sigma_{cx} + \sigma_{el})} \int f_0(V_\perp; V_z) V_\perp dV_\perp dV_z \\ &\times \int_0^{2\pi} (1 + V_\perp \sin\psi) \left(1 + V_\perp^2 + V_z^2 + 2V_\perp \sin\psi\right)^{1/2} d\psi. && (4.57) \end{aligned}$$

In order to find f_0, we average Eq. (4.53) over ψ, which eliminates the dominant term $\omega_{ci}\partial f/\partial\psi$. We then replace f by f_0 in the remaining terms to obtain an equation for f_0:

$$\begin{aligned} - & \frac{1}{\xi^2}\frac{\partial f_0}{\partial V_z} - W_1(V_\perp; V_z) f_0 + \frac{\sigma_{el}}{\pi(\sigma_{cx} + \sigma_{el})} \int W_2(V_\perp; V_z; V_\perp'; V_z') f_0(V_\perp'; V_z') V_\perp' dV_\perp' dV_z' \\ + & \frac{\sigma_{cx}}{\sigma_{cx} + \sigma_{el}} \delta(V_\perp - 1)\delta(V_z) \int W_1(V_\perp'; V_z') f_0(V_\perp'; V_z') V_\perp' dV_\perp' dV_z' = 0, \qquad (4.58) \end{aligned}$$

where

$$\begin{aligned} & W_1(V_\perp; V_z) \equiv \int_0^{2\pi} \left(1 + V_\perp^2 + V_z^2 + 2V_\perp \sin\psi\right)^{1/2} \frac{d\psi}{2\pi}, && (4.59) \\ & W_2(V_\perp; V_z; V_\perp'; V_z') \equiv \int_0^{2\pi} \frac{d\psi}{2\pi} && (4.60) \\ & \times \int_0^{2\pi} \delta\left[V_\perp^2 + V_z^2 + V_\perp \sin\psi - V_\perp' \sin\psi' - V_z V_z' - V_\perp V_\perp' \cos(\psi - \psi')\right] d\psi'. \end{aligned}$$

This equation suggests that f_0 must have the following structure:

$$f_0 = \frac{n}{2\pi|u_E|^3}\left[\delta(V_\perp - 1)G(V_z) + H(V_\perp, V_z)\right], \qquad (4.61)$$

where H is a smooth function of $V_\perp$. Indeed, we need a δ-function piece in f_0 to balance the corresponding term in Eq. (4.58). On the other hand, a smooth part of the distribution (H) is needed to balance the term with W_2 in Eq. (4.58). This term is a smooth function of $V_\perp$ even for a peaked f_0 since it involves integration of f_0 over the entire velocity space. In terms of G and H, the normalization condition (4.39) translates into

$$\int G dV_z + \int H V_\perp dV_\perp dV_z = 1. \tag{4.62}$$

The two independent balance conditions for the peaked and smooth terms in Eq. (4.58) give a set of two coupled equations for G and H:

$$\begin{aligned}
&\frac{1}{\xi^2}\frac{\partial G}{\partial V_z} + W_1(1;V_z)G - \frac{\sigma_{cx}}{\sigma_{cx}+\sigma_{el}}\delta(V_z)\int W_1(1;V_z')G(V_z')dV_z' \\
&= \frac{\sigma_{cx}}{\sigma_{cx}+\sigma_{el}}\delta(V_z)\int W_1(V_\perp';V_z')H(V_\perp';V_z')V_\perp' dV_\perp' dV_z',
\end{aligned} \tag{4.63}$$

$$\begin{aligned}
&\frac{1}{\xi^2}\frac{\partial H}{\partial V_z} + W_1(V_\perp;V_z)H - \frac{\sigma_{el}}{\pi(\sigma_{cx}+\sigma_{el})}\int W_2(V_\perp;V_z;V_\perp';V_z')H(V_\perp';V_z')V_\perp' dV_\perp' dV_z' \\
&= \frac{\sigma_{el}}{\pi(\sigma_{cx}+\sigma_{el})}\int W_2(V_\perp;V_z;1;V_z')G(V_z')dV_z'.
\end{aligned} \tag{4.64}$$

Equation (4.63) together with the normalization condition (4.39) allows us to readily express G in terms of H:

$$\begin{aligned}
G(V_z) &= \exp\left[-\xi^2\int_0^{V_z} W_1(1;V_z')dV_z'\right]\Theta(V_z)\left(1-\int H(V_\perp,V_z)V_\perp dV_\perp dV_z\right) \\
&\times \left(\int_0^\infty \exp\left[-\xi^2\int_0^{V_z} W_1(1;V_z')dV_z'\right]dV_z\right)^{-1},
\end{aligned} \tag{4.65}$$

where Θ is a step function. This expression allows us to reduce Eq. (4.64) to an equation for $H(V_\perp;V_z)$ alone. We note that, in the absence of elastic scattering ($\sigma_{el} = 0$), Eq. (4.64) has a simple solution $H = 0$. Then Eqs. (4.61) and (4.65) with $H = 0$ give an analytic expression for the ion distribution. In the presence of both, charge-exchange and elastic collisions, Eqs. (4.64) and (4.65) have to be solved numerically. We plan to perform these calculations and describe them elsewhere. However, the dependence of j_r and j_z on plasma parameters in the most representative limiting cases can be obtained even without solving these equations. The shape of the distribution function enters j_r and j_z only via form-factor multipliers [see coefficients α_z and α_r defined by Eqs.(4.71) and (4.75)].

Distribution function and ion flux for predominantly longitudinal transport ($\xi \ll 1$)

In order to treat this limiting case, we use the following rescaling transformation:

$$g \equiv G/\xi, \qquad h \equiv H/\xi^3, \tag{4.66}$$

$$s_z \equiv \xi V_z, \qquad s_\perp \equiv \xi V_\perp. \tag{4.67}$$

We then put $\xi = 0$ in the transformed Eqs. (4.64) and (4.65) to obtain:

$$g(s_z) \;=\; \exp\left[-\frac{s_z^2}{2}\right]\Theta\left(s_z\right)\sqrt{\frac{2}{\pi}}\left(1-\int h(s'_\perp, s'_z)s'_\perp ds'_\perp ds'_z\right), \tag{4.68}$$

$$\begin{aligned}&\frac{\partial h}{\partial s_z} + h\sqrt{s_\perp^2+s_z^2} - \frac{2\sigma_{el}}{\pi(\sigma_{cx}+\sigma_{el})}\int \frac{h(s'_\perp; s'_z)s'_\perp ds'_\perp ds'_z}{\sqrt{s_\perp^2 s_\perp'^2 - \left[s_\perp^2+s_z^2-s_z s'_z\right]^2}} \\ &= \frac{2\sigma_{el}}{(\sigma_{cx}+\sigma_{el})|s_z|}\exp\left[-\frac{(s_\perp^2+s_z^2)^2}{2s_z^2}\right]\Theta\left(s_z\right)\sqrt{\frac{2}{\pi}}\left(1-\int h(s_\perp, s_z)s_\perp ds_\perp ds_z\right).\end{aligned} \tag{4.69}$$

It is important that the only parameter in these equations is σ_{el}/σ_{cx}, which makes both $g(s_z)$ and $h(s_\perp; s_z)$ universal functions for a given ratio σ_{el}/σ_{cx}. As σ_{el}/σ_{cx} is typically an order of unity quantity, the characteristic values for $s_\perp$, s_z, g, and h in Eqs. (4.68) and (4.69) are also order of unity.

The parallel ion flux defined by Eq. (4.56) can now be presented in the form:

$$j_z = \alpha_z \frac{n|u_E|}{\xi}\frac{E_\parallel^a}{|E_\parallel^a|} = \alpha_z n\left[\frac{|eE_\parallel|}{m_i n_0(\sigma_{cx}+\sigma_{el})}\right]^{1/2}\frac{E_\parallel^a}{|E_\parallel^a|}, \tag{4.70}$$

with

$$\alpha_z \equiv \sqrt{\frac{2}{\pi}}\left(1-\int h s_\perp ds_\perp ds_z + \sqrt{\frac{\pi}{2}}\int h s_z s_\perp ds_\perp ds_z\right). \tag{4.71}$$

The radial ion flux is negligible at $\xi \ll 1$ since it is smaller than j_z by a factor ξ^2.

Distribution function and ion flux for predominantly radial transport ($\xi \gg 1$)

In this limiting case, the terms $\partial G/\partial V_z$ and $\partial H/\partial V_z$ are negligible in Eqs. (4.63) and (4.64). It then follows from Eqs. (4.63) and (4.62) that

$$G(V_z) = \delta(V_z)\left(1 - \int H(V_\perp', V_z')V_\perp' dV_\perp' dV_z'\right). \tag{4.72}$$

Substitution of this expression into Eq. (4.64) gives a universal equation for $H(V_\perp; V_z)$:

$$\begin{aligned} & W_1(V_\perp; V_z)H - \frac{\sigma_{el}}{\pi(\sigma_{cx}+\sigma_{el})}\int W_2(V_\perp; V_z; V_\perp'; V_z')H(V_\perp'; V_z')V_\perp' dV_\perp' dV_z' \\ & = \frac{\sigma_{el}W_2(V_\perp; V_z; 1; 0)}{\pi(\sigma_{cx}+\sigma_{el})}\left(1 - \int H(V_\perp', V_z')V_\perp' dV_\perp' dV_z'\right). \end{aligned} \tag{4.73}$$

The characteristic values of H, $V_\perp$, and V_z are all order of unity in this equation.

Taking into account (4.57) and (4.72), we find that the radial ion flux is given by

$$j_r = \alpha_r n |u_E| \xi^2 \frac{|E_\parallel^a|}{E_r^a} = \alpha_r n n_0 (\sigma_{cx}+\sigma_{el})\frac{u_E^2}{|\omega_{ci}|}\frac{E_r^a}{|E_r^a|}, \tag{4.74}$$

with

$$\begin{aligned} \alpha_r \equiv & \frac{8}{3\pi}\frac{2\sigma_{cx}+\sigma_{el}}{(\sigma_{cx}+\sigma_{el})}\left[1 - \int HV_\perp dV_\perp dV_z \right. \\ + & \left. \frac{3}{32}\int HV_\perp dV_\perp dV_z \int_0^{2\pi}(1+V_\perp\sin\psi)\left(1+V_\perp^2+V_z^2+2V_\perp\sin\psi\right)^{1/2} d\psi\right]. \end{aligned} \tag{4.75}$$

We note that $H = 0$ and $\alpha_r = 16/3\pi$ in the absence of elastic scattering ($\sigma_{el} = 0$). The longitudinal ion flux is formally zero for the distribution function (4.72). In reality, j_z is, of course, finite, but it is suppressed by a large factor ξ^4 compared to j_r.

4.6 Formulation of the Self-consistent Model

In order to describe the operation of a helicon plasma source, one has to solve self-consistently the particle balance problem, the power balance problem, and the wave equation. There is a natural time scale separation in helicon sources:

$$\tau_p \gg \tau_E \gg 2\pi/\omega. \tag{4.76}$$

This implies that a steady-state regime is established on a time scale comparable to τ_p when the density profile comes into equilibrium. The condition (4.76) indicates that the evolution of the electron temperature profile and the evolution of the rf-field structure are adiabatic. At each moment, the temperature profile corresponds to the thermal equilibrium.

The evolution of the plasma density profile is described by the continuity equation (4.40). The radial and longitudinal ion fluxes j_r and j_z are given by Eqs. (4.56) and (4.57), where f_0 is the gyro-averaged ion distribution function satisfying Eq. (4.58). The ambipolar electric field $\mathbf{E}^a$, which determines the ion fluxes (4.56) and (4.57), and the ionization rate by electron impact $\langle\sigma_{ion}v\rangle_e$, which enters the continuity equation (4.40), are related to the electron temperature T_e and plasma density n. In equilibrium, the electron pressure gradient is balanced by the ambipolar electric field. This immediately allows us to express the ambipolar electric field in terms of T_e and n:

$$\mathbf{E}^a = -\frac{1}{n|e|}\nabla(nT_e). \tag{4.77}$$

The main contribution to $\langle\sigma_{ion}v\rangle_e$ comes from the electrons with energy ε close to the ionization threshold energy ε_{ion}; i.e. ε exceeds ε_{ion}, but both values are comparable. At this range of energies, the ionization cross-section σ_{ion} as a function of ε can be approximated as

$$\sigma_{ion}(\varepsilon) \approx \frac{\pi e^4}{\varepsilon_{ion}\varepsilon^2}\left(\varepsilon - \varepsilon_{ion}\right) \tag{4.78}$$

for $\varepsilon \geq \varepsilon_{ion}$ and $\sigma_{ion}(\varepsilon) = 0$ for $\varepsilon < \varepsilon_{ion}$. For a Maxwellian electron distribution,

$$f_e(\mathbf{v}) \approx \frac{n}{(2\pi T_e/m_e)^{3/2}}\exp\left[-\frac{m_e v^2}{2T_e}\right], \tag{4.79}$$

we find that

$$\langle\sigma_{ion}v\rangle_e \equiv \frac{1}{n}\int \sigma_{ion}vf_e d\mathbf{v} \approx 2\sqrt{\frac{2\pi T_e}{m_e}}\frac{e^4}{\varepsilon_{ion}^2}\exp\left[-\frac{\varepsilon_{ion}}{T_e}\right]. \tag{4.80}$$

Using a similar approximation for the excitation cross-section σ_{exc}, we find that for a Maxwellian electron distribution the power lost via line-radiation, which is equal to the power lost by the plasma electrons on atom excitation, is given by

$$\begin{aligned} P_{rad} &= n_0 n\left\langle\sigma_{exc}v\frac{m_e v^2}{2}\right\rangle_e = n_0\int\frac{m_e v^2}{2}\sigma_{exc}vf_e d\mathbf{v} \\ &\approx 2\sqrt{2\pi}m_e n_0 n\left(\frac{T_e}{m_e}\right)^{3/2}\frac{e^4}{T_e\varepsilon_{exc}}\exp\left[-\frac{\varepsilon_{exc}}{T_e}\right]. \end{aligned} \tag{4.81}$$

The power balance condition determines the electron temperature. In thermal equilibrium, the rf-power absorbed by the electrons equals the power lost via line-radiation. In order to find the rf-power absorption, we present the rf-electric field in the following form:

$$\mathbf{E} = \frac{1}{2}\sum_{\omega}\mathbf{E}(\omega)\mathrm{e}^{-i\omega t} + c.c., \tag{4.82}$$

where

$$\mathbf{E}(\omega) = \sum_m\left[\mathbf{e}_r E_r(\omega,r,m,z) + \mathbf{e}_\phi E_\phi(\omega,r,m,z) + \mathbf{e}_z E_z(\omega,r,m,z)\right]\mathrm{e}^{im\phi}. \tag{4.83}$$

We will drop all the arguments of the Fourier amplitudes E_r, E_ϕ, and E_z in order to simplify the equations. For a single harmonic the rf-power absorption is given by:

$$-\frac{i\omega}{16\pi}\left(\varepsilon_{\alpha\beta}-\varepsilon^*_{\beta\alpha}\right)E^*_\alpha E_\beta, \tag{4.84}$$

so that the total rf-power absorption is given by the following sum of the contributions from all the harmonics:

$$-\sum_{\omega,\ m}\frac{i\omega}{16\pi}\left(\varepsilon_{\alpha\beta}-\varepsilon^*_{\beta\alpha}\right)E^*_\alpha E_\beta, \tag{4.85}$$

where $\varepsilon_{\alpha\beta}$ is the plasma dielectric tensor. Finally, the power balance condition takes the form:

$$2\sqrt{2\pi} m_e n_0 n \left(\frac{T_e}{m_e}\right)^{3/2} \frac{e^4}{T_e \varepsilon_{exc}} \exp\left[-\frac{\varepsilon_{exc}}{T_e}\right] =$$
$$= -\sum_{\omega,\ m} \frac{i\omega}{16\pi} \left(\varepsilon_{\alpha\beta} - \varepsilon^*_{\beta\alpha}\right) E^*_\alpha E_\beta. \tag{4.86}$$

The electric field in Eq. (4.86) is determined by the wave equation (3.6):

$$\nabla\left[\nabla \mathbf{E}(\omega)\right] - \nabla^2 \mathbf{E}(\omega) = \frac{\omega^2}{c^2}\mathbf{D}(\omega) + \frac{4\pi\omega i}{c^2}\mathbf{j}(\omega). \tag{4.87}$$

Here $\mathbf{j}(\omega)$ is the Fourier amplitude of the antenna current [see Eq.(3.5)] and $\mathbf{D}(\omega)$ is the Fourier amplitude of the electric displacement [see Eq.(3.4)], which is related to $\mathbf{E}(\omega)$ by the cold plasma dielectric tensor $\varepsilon_{\alpha\beta}$:

$$D_\alpha(\omega) = \varepsilon_{\alpha\beta} E_\beta(\omega). \tag{4.88}$$

The components of Eq. (4.88) and the corresponding components of the dielectric tensor are presented in Chapter 2 [see Eqs. (3.8)-(3.13)]. The wave equation must be solved for a given antenna current with corresponding boundary conditions.

The closed set of equations (4.40), (4.86), and (4.87) describes helicon discharge in the regime when the plasma effect on the background gas can be neglected. Our ultimate goal is to solve these equations numerically in the regimes relevant to VASIMR. This is being done in collaboration with ASPL (Dr. A.Ilin) and ORNL (Dr. M.Carter). Most of the computational effort is associated with the finding rf-field structure and an EMIR code developed at ORNL appears to be a relevant field solver.

As a step towards full-scale calculations, we will consider two idealized problems that do not require the same extend of numerical computations. However, they still allow us to capture some of the key physics features of the discharge operation.

These two simple cases can also be used in order to test the more comprehensive code. In Section 4.7, we consider a case when electron temperature is constant throughout the discharge, so that the particle balance problem becomes effectively decoupled from the power balance and rf-field structure pieces. We find the amount of gas (in case of the longitudinal plasma flow) and the ionization rate (in case of the radial plasma flow) necessary for steady-state discharge operation. In Section 4.8, we analyze a regime with predominantly radial plasma flow. In this case, the problem of describing the source operation effectively becomes one-dimensional. Using our 1D code, designed specifically for this regime, we find a steady-state regime and calculate the corresponding plasma density profile, electron temperature profile, and rf-field structure.

4.7 Plasma Density Profiles

In this section, we use the results of Sec. 4.5 to analyze plasma density profiles under the assumptions that the gas ionization rate $\langle \sigma_{ion} v \rangle_e$ and the electron temperature T_e are constant throughout the discharge. We can then rewrite the ambipolar electric field in the form:

$$\mathbf{E}^a = -\frac{T_e}{|e|}\frac{1}{n}\frac{\partial n}{\partial \mathbf{r}}. \tag{4.89}$$

In order to find the plasma density profile, we need to solve the continuity equation (4.40) in which the fluxes are self-consistently expressed in terms of $n(\mathbf{r}, t)$ via Eqs. (4.56), (4.57), and (4.89). We will use the "absorbing" boundary conditions at the end-plate and at the side walls:

$$n(a, z) = 0, \tag{4.90}$$

$$n(r, 0) = 0. \tag{4.91}$$

In addition, we put

$$n(r, L) = 0 \tag{4.92}$$

since the plasma density in the outgoing collisionless flow is much smaller than the density inside the source where the flow is collisional.

It should be noted that Eq. (4.40) for $n(\mathbf{r}, t)$ is invariant with respect to a rescaling transformation $n \to \alpha n$, despite the fact that this equation is nonlinear. Therefore, Eq. (4.40) determines just a functional dependence of n on $\mathbf{r}$ and t, but not the absolute value of the plasma density. In order to find the absolute value of n, we must solve the particle and power balance equations together.

The rescaling symmetry of Eq. (4.40) allows us to seek $n(\mathbf{r}, t)$ in the form

$$n(\mathbf{r}, t) = n(\mathbf{r})\mathrm{e}^{\gamma t}, \tag{4.93}$$

where γ is a constant. This expression indicates that, depending on our input parameters T_e and $\langle \sigma_{ion} v \rangle_e$, we may have not just a steady-state solution with $\gamma = 0$, but also growing ($\gamma > 0$) or decaying ($\gamma < 0$) density profiles. Clearly, solutions with $\gamma > 0$ describe an avalanche-type ionization that occurs when the losses due to plasma transport are insignificant. In reality, the exponential growth of plasma density will eventually seize due to the input power limitations.

In order to capture the key features of the plasma density profile in a technically simple way, we will analyze Eq. (4.40) in the two complimentary limiting cases: $\xi \ll 1$ and $\xi \gg 1$. In these cases Eq. (4.40) becomes effectively one-dimensional. As indicated above, the case $\xi \ll 1$ corresponds to predominantly longitudinal transport and the case $\xi \gg 1$ corresponds to predominantly radial transport. Taken together, these two solutions give sufficient qualitative understanding of all possible flows including the intermediate regime $\xi \sim 1$.

4.7.1 Longitudinal Transport

It is allowable to neglect j_r in Eq. (4.40) in the limit $\xi \ll 1$, which simplifies Eq. (4.40) to:

$$\gamma n + \frac{\partial j_z}{\partial z} = n_0 n \left\langle \sigma_{ion} v \right\rangle_e , \tag{4.94}$$

where we use the representation (4.93) for n. In this equation, the longitudinal flux j_z is related to the density profile $n(z)$ by Eqs. (4.70) and (4.89), which give:

$$j_z \;\; = \;\; -\alpha_z n C_s \left(n n_0 (\sigma_{cx} + \sigma_{el}) \left| \frac{\partial n}{\partial z} \right| \right)^{-1/2} \frac{\partial n}{\partial z}. \tag{4.95}$$

We first consider a steady-state profile for which $\gamma = 0$, so that Eq. (4.94) takes the form:

$$-\frac{\partial \eta / \partial \zeta}{|\partial \eta / \partial \zeta|} \frac{\partial}{\partial \zeta} \left(\sqrt{\eta \left| \frac{\partial \eta}{\partial \zeta} \right|} \right) = \eta, \tag{4.96}$$

where η and ζ are dimensionless variables defined by:

$$\eta \;\; \equiv \;\; \frac{n}{max(n)}, \tag{4.97a}$$

$$\zeta \;\; \equiv \;\; \left(\frac{\left\langle \sigma_{ion} v \right\rangle_e^2}{\alpha_z^2 C_s^2} (\sigma_{cx} + \sigma_{el}) \right)^{1/3} \int_0^z n_0 dz. \tag{4.97b}$$

We use a substitution

$$\frac{\partial \eta}{\partial z} = \Phi(\eta), \tag{4.98}$$

where $\Phi(\eta)$ is a new unknown function, to transform the second-order equation (4.96) to a first-order equation for Φ:

$$-|\Phi| \frac{\partial}{\partial \eta} \sqrt{\eta |\Phi|} = \eta. \tag{4.99}$$

A straightforward integration of this equation gives:

$$|\Phi(\eta)| = \frac{(1-\eta^3)^{2/3}}{\eta}, \tag{4.100}$$

where the integration constant has been determined from Eq. (4.97a), which requires that $\eta = 1$ at the point where $\Phi(\eta) = 0$.

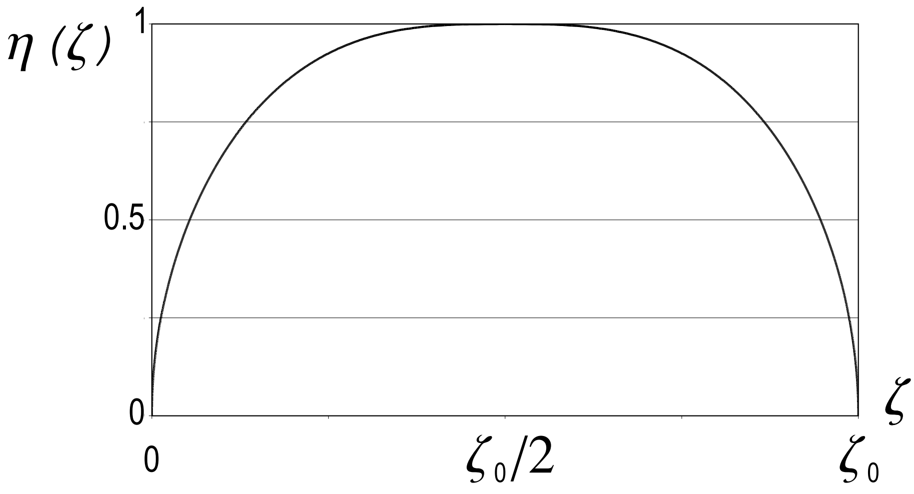

Figure 4.6: Normalized longitudinal profile of the plasma density [plot of the solution given by Eqs. (4.101)].

Equations (4.98) and (4.100) allow us to construct a density profile that satisfies the boundary condition at the end-plate ($\eta(0) = 0$) and has $\eta = 0$ at some distance ζ_0 away from the end-plate. This solution is implicitly given by the following integrals:

$$\zeta(\eta) = \int_0^\eta \frac{xdx}{(1-x^3)^{2/3}} \qquad \text{for} \qquad 0 < \zeta < \zeta_0/2, \tag{4.101a}$$

$$\zeta(\eta) = \zeta_0/2 + \int_\eta^1 \frac{xdx}{(1-x^3)^{2/3}} \qquad \text{for} \qquad \zeta_0/2 < \zeta < \zeta_0, \tag{4.101b}$$

where

$$\zeta_0 \equiv 2\int_0^1 \frac{xdx}{(1-x^3)^{2/3}} = \frac{4\pi}{3\sqrt{3}}. \tag{4.102}$$

The plot of $\eta(\zeta)$ for this solution is shown in Fig. 4.6. Note that $\eta(\zeta)$ is a symmetric function. The corresponding density profile $n(z)$ is shown in Fig. 4.7. In contrast with $\eta(\zeta)$, the function $n(z)$ is not symmetric. The symmetry of the density profile breaks because of the gas density gradient along the tube.

It is important that ζ_0 is not a free parameter since it is fixed by Eq. (4.102). Equations (4.102) and (4.97b) show that the open-end boundary condition (4.92)

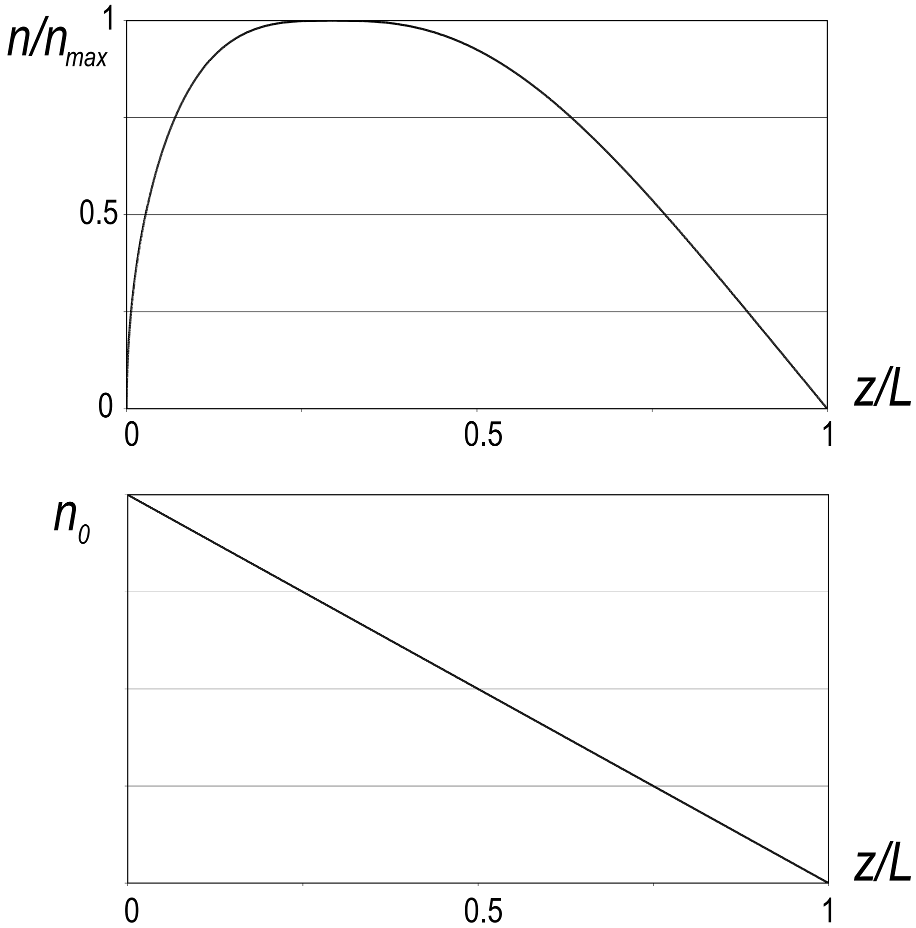

Figure 4.7: Asymmetry in the longitudinal plasma density profile (upper plot) due to the gas density gradient in Knudsen flow (lower plot).

requires a fixed amount of gas to establish the steady-state regime. Namely,

$$\int_0^L n_0 dz = \frac{4\pi}{3\sqrt{3}} \left(\frac{\langle \sigma_{ion} v \rangle_e^2}{\alpha_z^2 C_s^2} (\sigma_{cx} + \sigma_{el}) \right)^{-1/3} . \tag{4.103}$$

If the gas content is too high, so that

$$\int_0^L n_0 dz > \frac{4\pi}{3\sqrt{3}} \left(\frac{\langle \sigma_{ion} v \rangle_e^2}{\alpha_z^2 C_s^2} (\sigma_{cx} + \sigma_{el}) \right)^{-1/3} , \tag{4.104}$$

then the ionization cannot be balanced by the ion transport, which formally means that a positive γ is required to satisfy the boundary conditions for Eq. (4.94). As a result, the plasma density grows in time under condition (4.104). Following the same

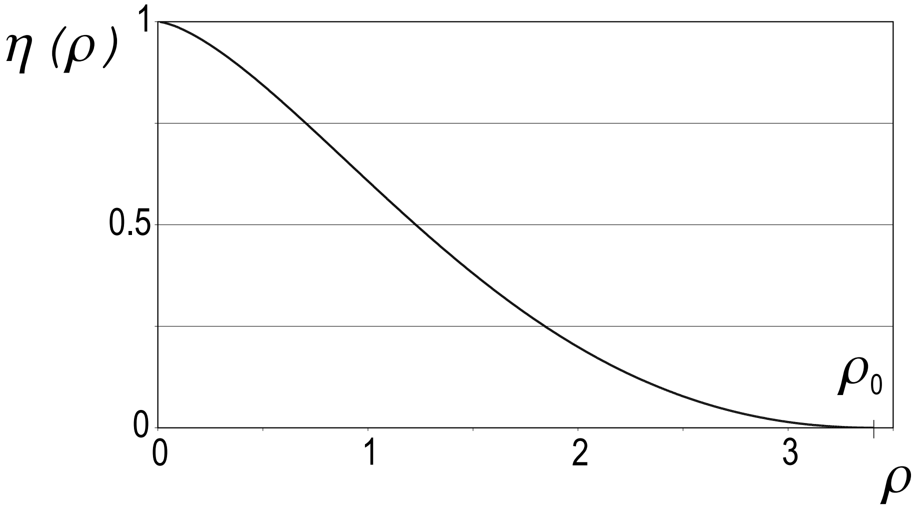

Figure 4.8: Normalized radial profile of the plasma density [plot of the numerical solution of Eq. (4.107)].

logic, we conclude that the plasma density should decay if the gas content is too low to satisfy Eq. (4.103).

4.7.2 Radial Transport

In the case of predominantly radial transport ($\xi \gg 1$) the continuity equation reads

$$\gamma n + \frac{1}{r}\frac{\partial}{\partial r}\left(j_r r\right) = n_0 n \left\langle \sigma_{ion} v \right\rangle_e , \tag{4.105}$$

where we again use representation (4.93). The relation between the radial flux and the density profile follows readily from Eqs. (4.74) and (4.89), which give:

$$j_r = -\alpha_r n C_s \frac{n_0 C_s^3 (\sigma_{cx} + \sigma_{el})}{n^2 |\omega_{ci}|^3} \frac{\partial n}{\partial r} \left| \frac{\partial n}{\partial r} \right| . \tag{4.106}$$

Similar to subsection 4.7.1, we first construct a steady state solution of Eq. (4.105). We note that the density profile must be monotonic in steady-state regime, so that $\partial n/\partial r < 0$ and $j_r > 0$ in this solution. Indeed, any hollow profile would create an inward plasma flux towards the axis, which is not permissible in a steady-state.

Since the radial flux is a positive definite, we put $\partial n/\partial r = -|\partial n/\partial r|$ to transform Eq. (4.105) with $\gamma = 0$ to

$$\frac{1}{\rho}\frac{\partial}{\partial\rho}\left(\frac{\rho}{\eta}\left[\frac{\partial\eta}{\partial\rho}\right]^2\right) = \eta. \tag{4.107}$$

Here, the dimensionless variables η and ρ are related to n and r by

$$\eta \equiv \frac{n}{n|_{r=0}} \tag{4.108a}$$

$$\rho \equiv \frac{|\omega_{ci}|}{C_s}\left(\frac{\langle\sigma_{ion}v\rangle_e}{\alpha_r(\sigma_{cx}+\sigma_{el})C_s}\right)^{1/3} r. \tag{4.108b}$$

As the radial flux must vanish at $r \rightarrow 0$, we require

$$\frac{\partial\eta}{\partial\rho} = 0 \qquad \text{for} \qquad \rho = 0. \tag{4.109}$$

In addition to this, Eq. (4.108a) requires that

$$\eta = 1 \qquad \text{for} \qquad \rho = 0. \tag{4.110}$$

Equations (4.109) and (4.110) uniquely determine the solution of Eq. (4.107), which is presented in Fig. 4.8. The function $\eta(\rho)$ takes on zero value at $\rho = \rho_0 \approx 3.403$. In order to obtain a steady-state solution, condition $\eta(\rho_0) = 0$ must be compatible with the boundary condition (4.90), which determines the required ionization rate $\langle\sigma_{ion}v\rangle_e$:

$$\langle\sigma_{ion}v\rangle_e = \alpha_r C_s(\sigma_{cx}+\sigma_{el})\left(\frac{\rho_0}{a}\frac{C_s}{|\omega_{ci}|}\right)^3. \tag{4.111}$$

It is noteworthy, that in contrast with the case of longitudinal transport, Eq. (4.111) is independent of the gas density.

If the ionization rate differs from that given by Eq. (4.111), then a nonzero value of γ is needed to construct a solution. Note that $\langle\sigma_{ion}v\rangle_e$ and γ enter Eq. (4.105) in a combination $\langle\sigma_{ion}v\rangle_e - \gamma/n_0$. Therefore, we can readily satisfy the wall boundary condition (4.90) by putting

$$\gamma = n_0\langle\sigma_{ion}v\rangle_e - \alpha_r C_s n_0(\sigma_{cx}+\sigma_{el})\left(\frac{\rho_0}{a}\frac{C_s}{|\omega_{ci}|}\right)^3. \tag{4.112}$$

It is interesting that the normalized density profile shown in Fig. 4.8 is independent of γ if we redefine ρ as

$$\rho \equiv \frac{|\omega_{ci}|}{C_s}\left(\frac{\langle\sigma_{ion}v\rangle_e - \gamma/n_0}{\alpha_r(\sigma_{cx}+\sigma_{el})C_s}\right)^{1/3} r. \qquad (4.113)$$

In agreement with intuitive expectations, we find that the plasma density builds up exponentially ($\gamma > 0$) when the ionization rate exceeds the "steady-state" value (4.111) and decays ($\gamma < 0$) when the ionization is too slow to satisfy Eq. (4.111).

4.8 Source with Predominantly Radial Transport (numerical model)

This section presents an example of how the power balance, particle balance, and rf-field structure pieces can be combined into a self-consistent picture. We consider a source with predominantly radial transport because in this case the problem of describing its operation becomes effectively one-dimensional and thus simpler. Although this regime of the source operation is not suitable for the VASIMR, this model can be relevant to the existing helicon plasma source experiment at ASPL. In some cases, when the magnetic field is not sufficiently strong to suppress the radial transport in this relatively long source, the radial plasma flow plays an important role in formation of the plasma density profile [see discussion at the end of Sec. 4.2 and Eq. (4.10)].

We consider a configuration similar to the one discussed in Chapter 3: axisymmetric plasma cylinder in a uniform equilibrium magnetic field $\mathbf{B}_0$ directed along the axis of symmetry (z). The plasma density, which is a function of radius r, is uniform in the azimuthal (ϕ) and axial (z) directions. The density dependence on z is neglected because it is not essential when the radial transport dominates. The background gas density is uniform in all directions.

We assume that the rf-power deposition into the plasma is associated with a radially localized helicon mode. It was explained in Chapter 3 that the mode with $m = 1$ couples better to the external antenna than the modes with higher azimuthal wave numbers. Therefore, we will only consider a single harmonic of the rf-field depending on t, z, and ϕ as $\exp(-i\omega t + ik_z z + im\phi)$, with $m = 1$.

The rf-field is generated by the radially localized helical antenna with radius R located inside the plasma. We used a similar set-up in Sec. 3.4 calculating the resonant power absorption by the plasma. This will allow us to use the already developed in Section 3.4 and Appendix B method for calculating the rf-field. The helical wire antenna is described in Appendix A. For this antenna, the wave numbers k_z and m are related by Eq. (A.8).

The plasma density evolution is given by the continuity equation:

$$\frac{\partial n}{\partial t} = -\frac{1}{r}\frac{\partial}{\partial r}(rj_r) + nn_0 \left\langle \sigma_{ion} v \right\rangle_e , \tag{4.114}$$

where the ionization rate $\left\langle \sigma_{ion} v \right\rangle_e$ is given by Eq. (4.80). In the limiting case of the predominantly radial plasma flow, the expression for j_r has been found in Sec. 4.5 [see Eq. (4.74)]:

$$j_r = \alpha_r n n_0 (\sigma_{cx} + \sigma_{el}) \frac{e^2 |E_r^a| E_r^a}{m_i^2 |\omega_{ci}|^3} = -\frac{\alpha_r n_0 (\sigma_{cx} + \sigma_{el})}{n m_i^2 |\omega_{ci}|^3} \frac{\partial (nT_e)}{\partial r} \left| \frac{\partial (nT_e)}{\partial r} \right| . \tag{4.115}$$

Here we used the expression given by Eq. (4.77) for the ambipolar electric field, where the form-factor α_r is defined by Eq. (4.75). In what follows, we will limit our consideration to the case when $\sigma_{el} \ll \sigma_{cx}$ that was discussed at the end of Sec. 4.5. In this case, the ion distribution function has a simple form and α_r can be easily calculated:

$$\alpha_r = \frac{16}{3\pi}.$$

The rf-field structure is described by the wave equation derived for the radially localized helicon modes in Chapter 3 [see Eq. (3.53)]:

$$\frac{1}{r}\frac{\partial}{\partial r}\left[r\frac{\partial E}{\partial r}\right] - \frac{m^2}{r^2}E = -\frac{m}{k_z^2 r}\frac{\omega^2}{c^2}\frac{E\partial g/\partial r}{1 + (m\partial g/\partial r)/k_z^2 r\eta} - \frac{4\pi i\omega}{c^2} j_0 R\delta(r - R), \tag{4.116}$$

where the function E is related to the longitudinal component of the rf-field by [see Eq. (3.29)]:

$$E = E_z \left[1 + k_z^2 r\eta \left(m\frac{\partial g}{\partial r} \right)^{-1} \right]. \tag{4.117}$$

The constant j_0 for the helical antenna is calculated in Appendix A and it is given by:

$$j_0 = \frac{I_0}{2\pi R^2} \frac{l}{\sqrt{l^2 + (2\pi R)^2}}, \tag{4.118}$$

where I_0 is the maximum amplitude of the antenna current and l is a helix period. The components g and η of the dielectric tensor have the following form [see Eq. (3.16)]:

$$g = \frac{\omega_{pe}^2}{\omega\omega_{ce}} \left(1 + \frac{2i\nu_e\omega}{\omega_{ce}^2} \right), \qquad \eta = -\frac{\omega_{pe}^2}{\omega(\omega + i\nu_e)}, \tag{4.119}$$

where the collisions frequency ν_e is defined as a sum of the electron-ion and electron-neutral collision frequencies (ν_{ei} and ν_{en}):

$$\nu_e \equiv \nu_{ei} + \nu_{en}. \tag{4.120}$$

The general form of the power balance equation [Eq. (4.86)] was derived in the previous section. As already mentioned in Sec. 4.3, the rf-power deposition is associated mainly with the longitudinal component of the rf-field. Taking this into account and neglecting the contributions from all the harmonics except $m = 1$, we find that Eq. (4.86) now reduces to

$$n_0 \sqrt{\frac{T_e}{2\pi m_e}} \frac{m_e e^2}{\varepsilon_{exc}} \exp\left[-\frac{\varepsilon_{exc}}{T_e} \right] = \frac{\nu_e}{\omega^2 + \nu_e^2} \frac{|E_z|^2}{8\pi}. \tag{4.121}$$

Here we also used expression (4.119) for η.

The system of Eqs. (4.114), (4.116), and (4.121) describes a self-consistent evolution of the plasma density profile. In order to solve this system, one would have to use the "absorbing" boundary condition for the density [see Eq. (4.90)]: $n(a) = 0$. Solving the wave equation, one has to match the rf-field at the tube to the outside solution, which is not known. However, we are looking for the regime when a radially localized mode is excited. This mode is localized inside the plasma, so that the rf-field structure inside the plasma is not sensitive to the exact form of the outside solution. Then in order to make the process of calculating the rf-field technically easier, we can match the inside solution at the tube to the uniform plasma solution, which is known: $E \propto r^{-|m|}$. We will also assume that the antenna radius R is equal to the tube radius a. For this set-up, the algorithm of calculating the rf-field inside the plasma is described in Appendix B.

The plasma density profile is also insensitive to the boundary condition as long as the density value at the boundary (n_b) is much smaller than the characteristic value of n. However, the calculation of the density evolution, which involves the calculation of j_r, becomes technically more complicated when boundary condition $n(a) = 0$ is used. Therefore, we use in our calculations boundary condition $n(a) = n_b$ instead of $n(a) = 0$, with $n_b \neq 0$ and much smaller than the characteristic plasma density.

We start the calculation with initial plasma density and electron temperature profiles. First, we calculate from Eq. (4.116) the rf-field corresponding to the initial density profile using the algorithm described in Appendix B. Note that the temperature is needed in order to calculate the electron-ion collision frequency. After the field is found, we compute the plasma rf-power absorption and use it to find a new temperature profile from the power balance condition (4.121). Using the new temperature and old plasma density, we calculate the right-hand side of Eq. (4.114). We choose a finite but small time-step $\delta\tau$ and then calculate $n(r, \delta\tau)$ as a sum of $n(r, 0)$ and a product of the computed right-hand side and $\delta\tau$. Taking $n(r, \delta\tau)$ and the calculated temperature as new initial profiles, we use the same procedure to calculate $n(r, 2\delta\tau)$ and new temperature. We continue this procedure calculating the density evolution. The time-step $\delta\tau$ must be much smaller than the characteristic time of the plasma density profile evolution τ_p. We assume that the system reached an equilibrium if

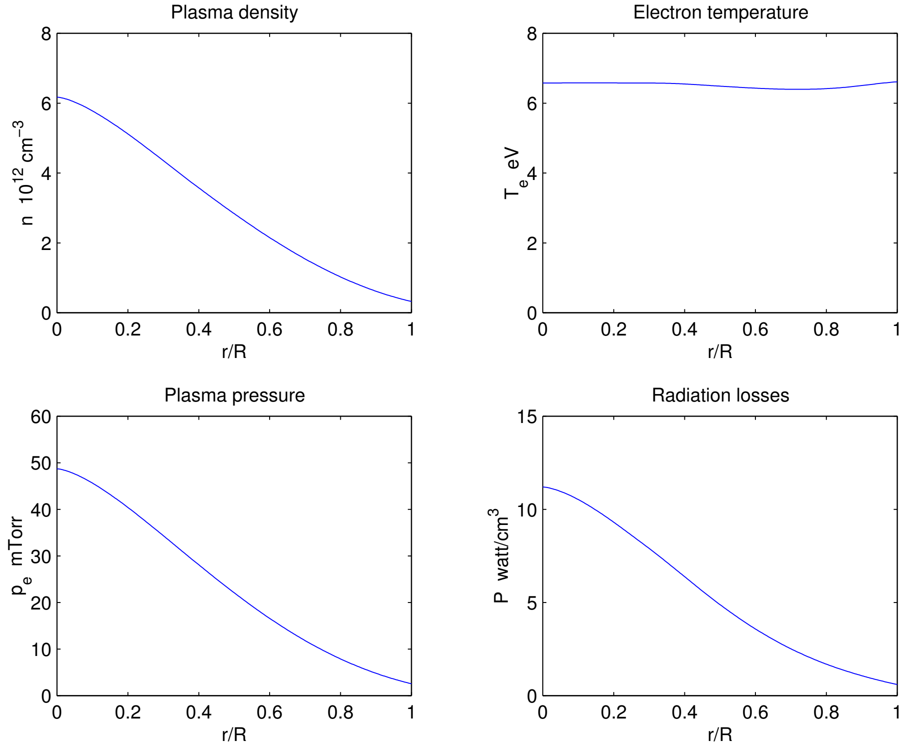

Figure 4.9: Equilibrium plasma density (top-left) and electron temperature (top-right) profiles and corresponding to them electron pressure (bottom-left) and radiation losses (bottom-right) in steady-state He discharge.

over a time period comparable to τ_p the change in density profile is small at each point along the radius.

As an initial plasma density profile we choose $n(r)$ calculated from a steady-state continuity equation with constant T_e. The value of T_e is chosen so that $n(0)/n(a) \gg 1$. The continuity equation determines just a functional dependence of n on r, but not the absolute value of the plasma density. The absolute value of n must be chosen so that the integral power balance condition is roughly satisfied, which ensures that T_e after the first time-step will be comparable to the initial value. This is crucial for the convergence of our procedure. In the previous section we showed that the integral power balance can be achieved only if a radially localized helicon mode is excited, which limits the range of acceptable absolute values of n to a very narrow window [see Fig. 4.5] for the given values of B_0, n_0, I_0, a, l, and ω. It turns out

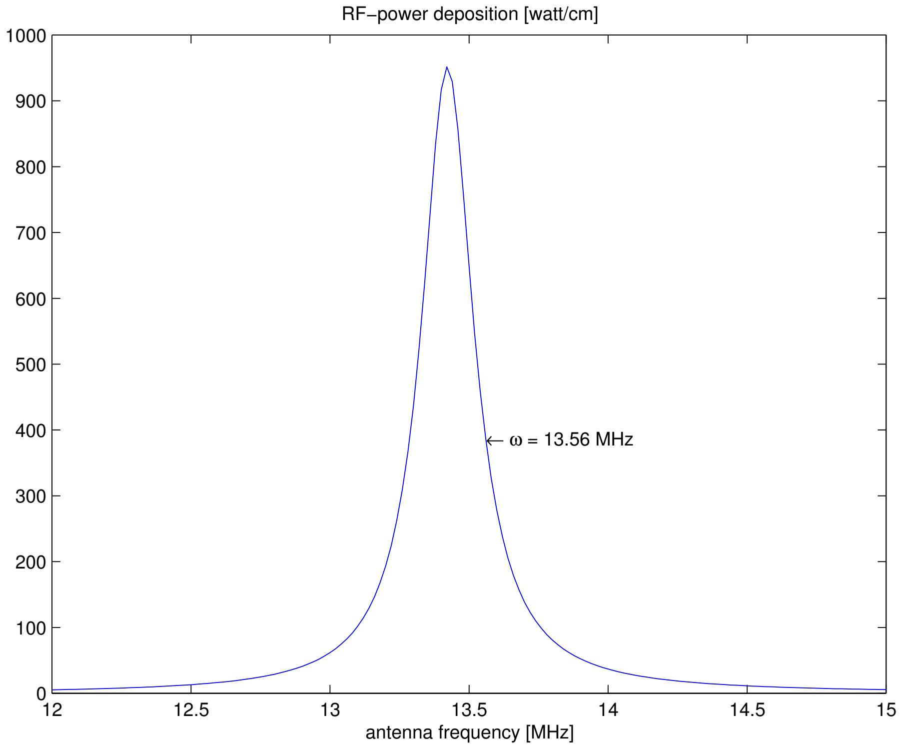

Figure 4.10: Rf-power deposited by the antenna as a function of the antenna frequency ω calculated using the equilibrium density profile shown in Fig. 4.9.

that for the considered initial density profile the mode exists only if n satisfies the condition $\omega_{pe}a/c \gg 1$. It is important to choose the value close to the higher density equilibrium [see Sec. 4.4]. In our calculations we use the above criteria to pick the initial absolute value of the plasma density. Therefore, we start with a state that is already close to the stable equilibrium, which ensures a relatively good convergence.

Now we note that that the equilibrium plasma density profile defined by Eqs. (4.114), (4.116), and (4.121) has a singularity at $r \to 0$. Indeed, for the radially localized modes described by Eqs. (4.116) and (4.117), E and E_z vanish at the axis. Then the electron temperature found from Eq. (4.121) also goes to zero at the axis. Since the ambipolar electric field for an axisymmetric plasma column vanishes at the axis, then the electron pressure (nT_e) is almost constant at the small values of r. This immediately indicates that n has a singularity at $r \to 0$. However, this

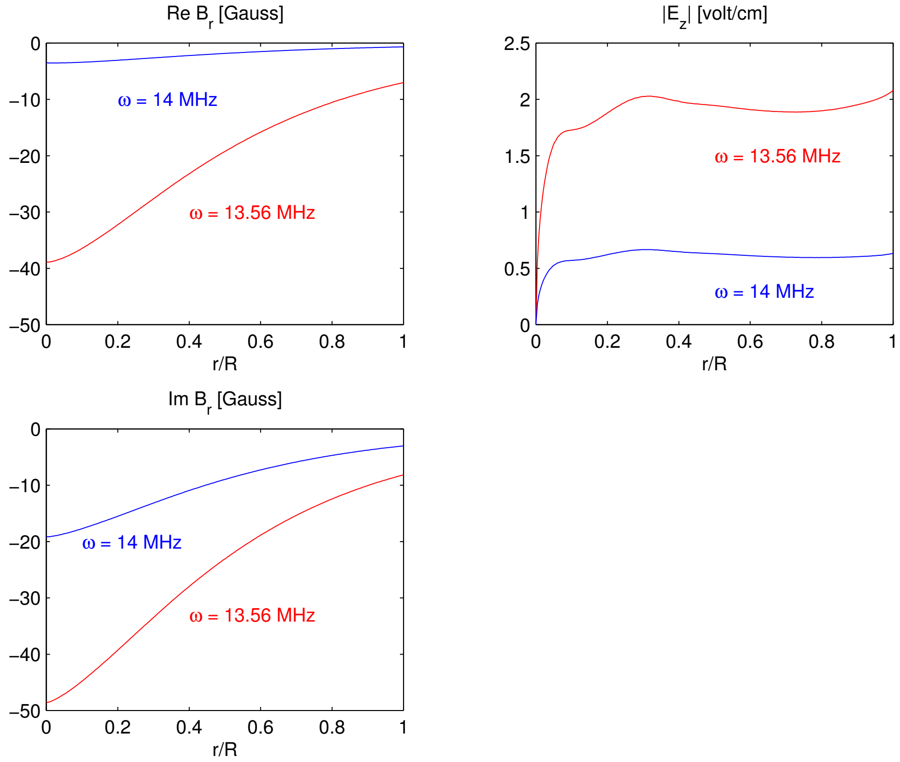

Figure 4.11: Rf-fields calculated for two different antenna frequencies $\omega = 13.56$ MHz and $\omega = 14$ MHz using the equilibrium density profile shown in Fig. 4.9.

singularity appears only because the electron heat conduction was not included into the power balance equation. We consider the regime when $\omega_{pe}a/c \gg 1$, since only then the mode can exist. It follows form Eqs. (4.116) and (4.117) that in this regime E_z changes slowly with radius for $a \geq r \gtrsim c/\omega_{pe}$ and it drops rapidly to zero near the axis ($r \lesssim c/\omega_{pe} \ll a$) [for example, see Fig. 4.11]. The electron temperature T_e determined from Eq. (4.121) has the same behavior and the width of the area where plasma density exhibits the singularity can be estimated as c/ω_{pe}. We remove the singularity by spatial temperature averaging, which is equivalent to the heat conduction. The averaging interval is chosen to be comparable to c/ω_{pe}, so that the singularity is eliminated but the rest of the temperature profile remains almost unchanged as a result of the averaging.

Following the procedure described above, we found a steady-state discharge in helium[1] for a source with the following parameters: $a = 6$ cm, $l = 64.3$ cm, $\omega = 13.56$ MHz, $n_0 = 3.3 \times 10^{14}$ cm^{-3}, $B_0 = 3$ kG, $I_0 = 25$ A. The equilibrium plasma density and electron temperature profiles are shown in Fig. 4.9. The temperature profile has been averaged using the averaging interval with the width 0.6 cm. It is noteworthy that the characteristic values of the calculated plasma density ($n \sim 10^{12}$ cm^{-3}) and electron temperature ($T_e \sim 6$ eV) are in the same range as typical experimental values. Figure 4.9 also presents the radial profiles of the electron pressure and radiation energy losses. For the equilibrium density profile, we performed an ω-scan which result is shown in Fig. 4.10. It follows from Fig. 4.10 that the equilibrium is located on the slope of the resonant absorption peak. Figure 4.11 demonstrates that in the equilibrium the rf-field in the plasma is enhanced due to the eigenmode excitation. In Fig. 4.11 we compare the field amplitudes calculated for $\omega = 13.56$ MHz and $\omega = 14$ MHz using the same equilibrium density profile. The field amplitudes are smaller for $\omega = 14$ MHz since this frequency is further from the eigenmode frequency than the antenna frequency $\omega = 13.56$ MHz used in the calculations (see Fig. 4.10).

4.9 Discussion

This section contains a few remarks concerning limitations of our model and possible experimental implications of our results.

Our solution of the ion kinetic equation shows that the ion distribution function (4.61) is strongly peaked at $v_r^2 + v_\varphi^2 = u_E^2$ ($V_\perp = 1$) when charge-exchange collisions with cold neutral gas are the dominant ion collisions. It is noteworthy that the peak in the ion distribution function survives even in the regime when there are elastic ion-atom collisions in addition to charge-exchange collisions. We observe that elastic collisions do not broaden the peak, but rather reduce its amplitude and add a

---

[1] For He, the excitation threshold energy is $\varepsilon_{exc} = 20.61$ eV and the ionization threshold energy is $\varepsilon_{ion} = 24.59$ eV.

"halo" component to the ion distribution. The reasons for peak broadening are the background gas temperature and ion-ion collisions. These factors become important only at a relatively high plasma density n. Otherwise, the background gas remains cold (although a population of energetic atoms may still arise [see below]). The role of ion-ion collisions should obviously increase with n since the corresponding collision frequency is proportional to n, whereas the ion-atom collision frequency is independent of n. At a sufficiently high plasma density, the ion-ion collisions will make the ion distribution Maxwellian with some temperature T_i and directed velocity $\mathbf{V}_i$. Despite the fact that this distribution differs form the one given by Eq. (4.61), the estimates for the ion fluxes presented in Sec. 4.2 will not change and the dependence of j_r and j_z on plasma parameters will remain the same in the limiting cases $\xi \ll 1$ and $\xi \gg 1$, except for the values of the form-factors α_r and α_z. It appears that the regime with relatively high plasma density is the one that is relevant to recent experiments [33–35]. The distribution function in Ref. [33–35] is reported to be of a Maxwellian-type suggesting that ion-ion collisions play an important role in its formation.

As we already mentioned in Sec. 4.1, we neglected the plasma effect on the background gas profile in our analysis. This assumption again implies that the plasma density is not too high. We will now estimate the corresponding density limit for our model. In the absence of plasma, the Knudsen gas flux (q_0) through the system can be estimated as

$$q_0 \approx n_0 C_0 \frac{a}{L^2}, \tag{4.122}$$

where C_0 is the sound speed in the injected cold gas. The ion-atom collisions convert some of the cold atoms into fast atoms at the rate

$$q_{hot} \approx \nu n, \tag{4.123}$$

where ν is the ion-atom collision frequency. It is clear that the criterion for neglecting cold gas depletion is $q_{hot} \ll q_0$. Using the estimate for ν given by Eq. (4.9), we present this criterion in the form:

$$n \ll \frac{n_0 C_0}{\xi(\xi+1)L\omega_{ci}}. \tag{4.124}$$

We now note that, in a steady-state regime

$$q_{hot} \approx \frac{n_{hot}}{\tau_{hot}}, \tag{4.125}$$

where n_{hot} is the density of fast neutrals and τ_{hot} is their confinement-time. Similarly, the gas flux can be written as

$$q_0 \approx \frac{n_0}{\tau_0}, \tag{4.126}$$

where τ_0 is the confinement-time of a cold atom. It should also be noted that τ_{hot} is always smaller than τ_0 in the Knudsen flow. Therefore, the condition $q_{hot} \ll q_0$ guarantees that

$$n_{hot} \ll n_0. \tag{4.127}$$

However, despite their low density, the fast neutrals can still have larger pressure than the cold gas. The characteristic energy of a fast neutral is comparable to that of a plasma ion ($m_i v^2/2$). We can then estimate the fast neutral pressure as

$$P_{hot} \approx n_{hot}\frac{m_i v^2}{2} \approx n\nu\tau_{hot}\frac{m_i v^2}{2}. \tag{4.128}$$

If the atom collisions with the walls are elastic (with random scattering from the the wall), then the time atom stays in the quartz tube can be estimated as L^2/av. If the collisions lead to energy loss, then the corresponding energy life-time is roughly $a/\varepsilon v$, where ε is the energy loss fraction in a single collision. It is clear that τ_{hot} is the shortest of these two times, i.e. we can put

$$\tau_{hot} \approx \frac{a/v}{\varepsilon + a^2/L^2}. \tag{4.129}$$

We now combine Eqs. (4.128), (4.129), and (4.9) to obtain

$$P_{hot} \approx P_{pl}(\xi+1)^2\frac{a/L}{\varepsilon + a^2/L^2}, \tag{4.130}$$

where $P_{pl} = nT_e$ is the plasma pressure. This estimate can explain the observed gas pressure increase due to plasma production in helicon plasma sources. An example of the corresponding experimental data is presented in Fig. 4.12, which clearly shows a substantial pressure increase that is much too big to be explained by the wall temperature increase. In this experiment, the background gas is He with a peak density $n_0 = 6 \cdot 10^{14}$ cm^{-3} and the plasma density measured in the outgoing flow is $n_{out} = 10^{12}$ cm^{-3}. The electron temperature is in the range of 5 eV. The characteristic value of plasma density inside the source is higher that n_{out} since the plasma density drops towards the open end (see Fig. 4.7). Taking $n \approx 10^{13}$ cm^{-3}, we find that the plasma pressure is roughly $P_{pl} \approx 60$ mTorr. In order to estimate parameter ξ [see Eq. (4.10)] we take $a \approx 5$ cm, $L \approx 100$ cm, $B_0 \approx 10^3$ G. The collision cross-sections in He are $\sigma_{el} \approx \sigma_{cx} \approx 2 \cdot 10^{-15}\ cm^{-2}$. The resulting value of ξ is 1.3. The fast neutral pressure observed in experiment is 150 mTorr (see Fig. 4.12). Equation (4.130) matches this value at $\varepsilon = 0.11$. Since the atom mass (m_i) in light gases is much smaller than the mass of the wall atoms (m_w), the energy transfer from the atoms to the wall is suppressed by roughly a factor of m_i/m_w, so that $\varepsilon \sim m_i/m_w$. For He atoms colliding with quartz tube walls this indicates that the fast neutral pressure is a good candidate to explain the substantial pressure increase. It is however difficult to be more conclusive at this point since Eq. (4.130) is a very rough estimate.

Another conceivable application of our results is a transition from peaked to hollow plasma density profiles observed in the helicon sources [36]. As discussed in Sec. 4.7.2, the radial density profile is always peaked at the axis if the radial transport dominates. On the other hand, the radial density profile is that of the ionization source if the transport is predominantly longitudinal. Therefore, the profile should be hollow if the ionization rate is peaked off-axis and the transport is predominantly longitudinal. The choice between the two regimes depends on the value of the dimensionless parameter $\xi^2(\xi+1)^2$ [see Eq. (4.14)] that increases with the increase of

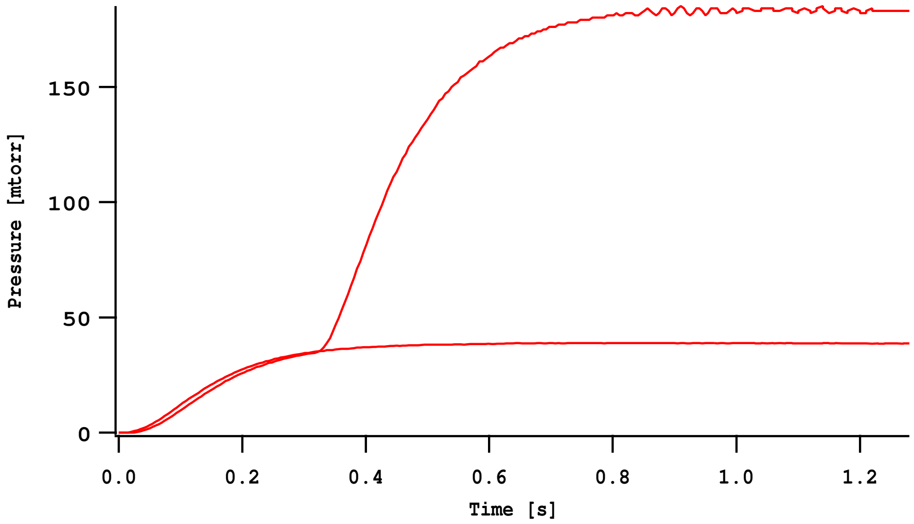

Figure 4.12: Increase in the neutral gas (He) pressure near the end-plate due to plasma production. Lower curve: time evolution of gas pressure without plasma. Upper curve: time evolution of gas pressure with plasma. The discharge starts at $t = 300$ms. (courtesy of J.Squire and VASIMR team).

n_0. Note that the transition reported in Ref. [36] was achieved primarily by reducing neutral gas pressure. This suggests that the observed effect may be partly associated with a transition from predominantly radial to predominantly longitudinal transport.

Chapter 5

Summary

This work has been motivated by the VASIMR project. The VASIMR device consists of three main components: the low energy plasma source, the ion cyclotron-resonance heating (ICRH) section, and the magnetic nozzle. The theoretical plasma physics aspects of helicon plasma sources and ICRH have been considered, with a primary focus on problems of general interest that have possible applications beyond VASIMR. The specific problems solved in this work should be ultimately incorporated into an integrated model that describes all elements of VASIMR self-consistently. The key physics results of the dissertation are listed below:

- A first-principle theory has been developed for single-pass ion cyclotron resonance absorption in the presence of a directed ion flow through the resonance. This problem presents a nonlinear generalization of the classical magnetic beach problem.

1) Full absorption is predicted for the incident wave when either linear theory or WKB approximation applies.

2) Nonlinear buildup of a steep density gradient at the resonance is predicted for slow incoming plasma flow. This modification of the plasma density leads to partial reflection of the incident wave when the width of the density drop is shorter than the wave-length.

3) A theory-based 1D code is developed to model self-consistently the rf-wave propagation and the ion motion through the cyclotron resonance.

4) The developed near-resonance theory can be incorporated into full-scale simulations of the rf-field in realistic geometry.

- New (radially localized) helicon modes in nonuniform plasma have been found. Similarly to electromagnetic waves in coaxial wave guide, these modes are characterized by unusually low frequency. These modes are likely to be responsible for the high efficiency of helicon sources at low frequencies.

- A kinetic problem of ion transport is solved in the regime when ion motion is controlled by an ambipolar electric field, uniform equilibrium magnetic field, and ion-neutral collisions.

1) The analysis explains the surprisingly large gas pressure increase due to plasma production. The effect is attributed to fast charge-exchange neutrals. The analysis also relates the transition from peaked to hollow plasma density profiles to the transition from radial to longitudinal ion flow.

2) Density profiles in the plasma source are calculated for a given temperature and a given gas ionization rate. The calculations specify the range of background gas densities and power inputs for which the source can operate in a stable steady-state regime.

- A first-principle theory for helicon discharge has been developed with a self-consistent treatment of the particle balance, power balance, and rf-field structure.

- A theory-based 1D numerical model has been developed for a helicon discharge with predominantly radial ion flow.

Appendices

Appendix A

Helical Antenna

We consider a helical wire antenna with a helix period l and radius R. The antenna current is $I_0 \cos(\omega t)$ (see Fig. A.1). The wire is parameterized in cylindrical coordinates (r, ϕ, z) the following way:

$$r = R, \tag{A.1}$$

$$\phi = 2\pi z/l. \tag{A.2}$$

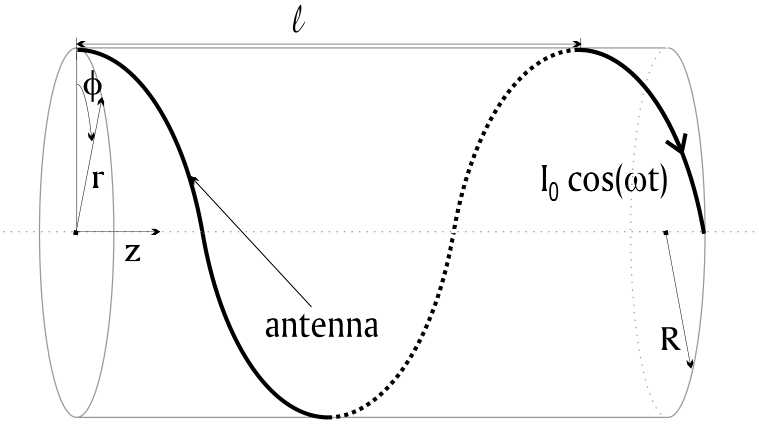

Figure A.1: Helical wire antenna with current $I_0 \cos(\omega t)$, helix period l, and radius R. It is parameterized by Eqs. (A.1) and (A.2).

The radial antenna current is zero, while the azimuthal and longitudinal components of the current density are given by:

$$j_\phi(r, \phi, z, t) = \frac{2\pi I_0 \cos(\omega t)}{\sqrt{l^2 + (2\pi R)^2}} \delta(r - R)\delta(\phi - 2\pi z/L), \tag{A.3}$$

$$j_z(r, \phi, z, t) = \frac{I_0 \cos(\omega t)}{\sqrt{l^2 + (2\pi R)^2}} \frac{l}{R} \delta(r - R)\delta(\phi - 2\pi z/l). \tag{A.4}$$

Expanding j_ϕ and j_z in Fourier series with respect to ϕ, one can present Eqs.(A.3) and (A.4) in the following form:

$$j_\phi(r,\phi,z,t) = -\frac{1}{2}\sum_{m=-\infty}^{+\infty}\left(\frac{k_z R}{m}\right) j_0 R\delta(r-R)\mathrm{e}^{im\phi+ik_z z-i\omega t} + c.c., \tag{A.5}$$

$$j_z(r,\phi,z,t) = \frac{1}{2}\sum_{m=-\infty}^{+\infty} j_0 R\delta(r-R)\mathrm{e}^{im\phi+ik_z z-i\omega t} + c.c., \tag{A.6}$$

where

$$j_0 \equiv \frac{I_0}{2\pi R^2}\frac{l}{\sqrt{l^2+(2\pi R)^2}}, \tag{A.7}$$

$$k_z = -\frac{2\pi m}{l}. \tag{A.8}$$

Note that k_z and m are not independent, i.e. for every m the value of k_z is specified by Eq. (A.8).

Appendix B

Procedure for Calculating Wave Field Structure and Power Deposition

In our calculations, we use plasma density profiles that have the form $n(r) = n_*G(r)$, where $G(r)$ is given by:

$$\begin{aligned} & && 1,\ r < r_1 \\ G(r) &= && \frac{1-h}{2}\cos\left(\pi\frac{r-r_1}{r_2-r_1}\right) + \frac{1+h}{2},\ r_1 \le r \le r_2 \\ & && h,\ r_2 < r, \end{aligned} \tag{B.1}$$

with $r_1 = 0.1R$, $r_2 = 0.9R$, and $h = 0.795$. In order to solve Eq. (3.53) numerically, we present it in a dimensionless form:

$$\frac{1}{x}\frac{\partial}{\partial x}\left[x\frac{\partial F}{\partial x}\right] - \frac{m^2}{x^2}F + \alpha f_0 G F \frac{1 - f_0 + i(\nu_e/\omega)f_0}{(1-f_0)^2 + f_0^2(\nu_e/\omega)^2} = -i\delta(1-x), \tag{B.2}$$

where

$$x \equiv r/R, \tag{B.3}$$

$$F \equiv \frac{c^2 E}{4\pi\omega j_0 R^2}, \tag{B.4}$$

$$\alpha \equiv \left(\frac{\omega_{pe}(n_*)R}{c}\right)^2, \tag{B.5}$$

$$f_0 \equiv -\frac{1}{m}\frac{\Omega}{xG}\frac{\partial G}{\partial x}, \tag{B.6}$$

$$\Omega \equiv -\frac{m^2\omega}{k_z^2 R^2 \omega_{ce}}. \tag{B.7}$$

The solution of Eq. (B.2) can be written as $F = A_1 F_1(x)$ for $0 \le x < 1$, where A_1 is a constant. For $x \le x_1 \equiv r_1/R$, $F_1 = x^{|m|}$ as it follows directly from Eqs. (B.2) and

(B.1). Straightforward numerical integration of Eq. (B.2) without the right-hand side from $x = x_1$ to $x = 1$ gives $F_1(x)$ for $x_1 \leq x < 1$. Solution of Eq. (B.2) for $x > 1$ is proportional to $x^{-|m|}$, and can be written as $F(x) = A_2 x^{-|m|}$, where A_2 is a constant. Wave field is continuous at $x = 1$, so that $A_2 = A_1 F_1(1)$. The matching condition (3.54) at $x = 1$ now allows us to find A_1:

$$A_1 = \left. \frac{i}{|m| F_1 + \partial F_1 / \partial x} \right|_{x=1} . \tag{B.8}$$

So, in order to find a solution of Eq. (B.2) one has to follow the following routine. The first step is to find F_1 numerically integrating Eq. (B.2) without the right-hand side from $x = x_1$ to $x = 1$ with the following boundary conditions at $x = x_1$: $F_1(x_1) = x_1^{|m|}$ and $\partial F_1(x_1)/\partial x = |m| x_1^{|m|-1}$. Then one finds A_1 using Eq. (B.8) and consequently computes the solution $F(x) = A_1 F_1(x)$ for $0 \leq x \leq 1$. The last step is to find $A_2 = A_1 F_1(1)$, which immediately gives the solution for $x > 1$: $F(x) = A_2 x^{-|m|}$.

Note that if $F_1(x)$ is known, then the power deposition Q can be immediately calculated via Eqs. (3.52) and (B.4) and taking into account that $F(1) = A_1 F_1(1)$.

Bibliography

[1] F.R.Chang Diaz, "VASIMR Engine", *The Scientific American* 283, 72-79 (2000).

[2] F.R. Chang Diaz, J.P. Squire, A.V. Ilin, G.E. McCaskill, T.X. Nguyen, D.S. Winter, A.J. Petro, G.W. Goebel, L. Cassady, K.A. Stokke, C.E. Dexter, M.D. Carter, F.W. Baity, G.C. Barber, R.H. Goulding, D.O. Sparks, S.W. Schwenterly, R.D. Bengtson, B.N. Breizman, V.T. Jacobson, R.Z. Sagdeev, K. Karavasilis, S.V. Novakovski, A.A. Chan, T.W. Glover,"The Development of VASIMR Engine", in Proceedings of the International Conference on Electromagnetics in Advanced Applications (ICEAA'99, Torino, Italy, Sep. 13-17, 1999), IEEE, 99-102 (1999).

[3] F.R.Chang Diaz, M.M.Hsu, T.F.Yang, "Rapid Mars Transit With Exhaust-Modulated Plasma Proplsion", *NASA Technical Paper* (National Aeronautics and Space Administration, Washington DC), 3539 (1995).

[4] M.Martinez-Sanchez, J.E.Pollard, "Spacecraft Electric Propulsion - An Overview", *Journal of Propulsion and Power*, **14**, 688-699 (1998).

[5] R.W.Boswell, Phys. Lett. **33A**, 457 (1970).

[6] R.W.Boswell, Plasma Phys. Control Fusion **26**, 1147 (1984).

[7] H.A. Blevin, P.J. Christiansen, Aust. J. Phys. **19**, 501 (1966).

[8] E.Z. Gusakov, M.A. Irzak, and A.D. Piliya, JETP Lett. **65**, 25 (1997).

[9] D.Arnush, F.F.Chen, Phys. Plasmas **5**, 1239 (1998).

[10] J.P. Klozenberg, B. McNamara, and P.C. Thonemann, J. Fluid Mech. **21**, 545 (1965).

[11] R.N. Sudan, A. Cavaliere, and M.N. Rosenbluth, Phys. Rev. **158**, 387 (1967).

[12] A.S. Kingsep, Yu.V. Mohkov, and K.V. Chukbar, Sov. J. Plasma Phys. **10**, 495 (1984).

[13] A.S. Kingsep, K.V. Chukbar, and V.V. Yan'kov, in *Reviews of Plasma Physics*, edited by B.B. Kadomtsev, (Consultants Bureau, New York, 1990) Vol. 16.

[14] E.F. Jaeger, et al., Nuclear Fusion **38**, 1 (1998).

[15] J.M. Urrutia, R.L. Stenzel, and C.L. Rousculp, Phys. Plasmas **2**, 1100 (1995).

[16] R.L. Stenzel, J.M. Urrutia, and C.L. Rousculp, Phys. Plasmas **2**, 1114 (1995).

[17] K.P.Shamrai, V.B.Taranov, Plasma Sources Sci. Technol. **5**, 474 (1996).

[18] E. Canobbio, Nucl. Fusion, **9**, 27 (1969).

[19] M. Brambilla, Nucl. Fusion, **9**, 343 (1969).

[20] A.F. Kuckes, Plasma Physics, **10**, 367 (1968).

[21] A.V. Timofeev, A.K. Nekrasov, Nucl. Fusion, **10**, 377 (1970).

[22] T.H.Stix, "Waves in Plasmas" p.342 (AIP New York 1992).

[23] T.H.Stix, "Waves in Plasmas" p.354 (AIP New York 1992).

[24] A.J.Perry, D.Vender, and R.W.Boswell, J. Vac. Sci. Technol. B **9**, 310 (1991).

[25] H.Kitagawa, A.Tsunoda, H.Shindo, and Y.Horiike, Plasma Sources Sci. Technol. **2**, 11 (1993).

[26] M.A.Liberman and A.J.Lichtenberg, “Principles of Plasma Discharges and Materials” (Wiley, New York, 1994).

[27] F.F.Chen, J. Vac. Sci. Technol. A **10**, 1389 (1992).

[28] K.P.Shamrai, Plasma Sources Sci. Technol. **7**, 499 (1998).

[29] B.N.Breizman and A.V.Arefiev, Phys. Rev. Lett. **84**, 3863 (2000).

[30] B.N.Breizman and A.V.Arefiev, Phys. Plasmas **3**, 907 (2001).

[31] B.N.Breizman and A.V.Arefiev, Phys. Plasmas **9**, 1015 (2002).

[32] R.K.Janev, W.D.Langer, K.Evans, Jr. and D.E.Post, Jr., “Elementary Processes in Hydrogen-Helium Plasmas” (Springer-Verlag, Berlin, Heidelberg, 1987).

[33] E.E.Scime, P.A.Keiter, M.W.Zintl, M.M.Balkey, J.L.Kline, and M.E.Koepke, Plasma Sources Sci. Technol. **7**, 186 (1998).

[34] T.Nakano, K.P.Giapis, R.A.Gottscho, T.C.Lee, and N.Sadeghi, J. Vac. Sci. Technol. B **11**, 2046 (1993).

[35] N.Sadeghi, M.van de Grift, D.Vender, G.M.W.Kroesen, and F.J.de Hoog, Appl. Phys. Lett. **70**, 835 (1997).

[36] S.Yun, S.Cho, G.Tynan, and H.Chang, Phys. Plasmas **8**, 358 (2001).

[37] V.L. Ginzburg, “Propagation of Electromagnetic Waves in Plasma” p. 158 (Gordon and Breach, New York, 1961).

[38] B.N.Breizman and A.V.Arefiev, Bull. Am. Phys. Soc. **44**, 70 (1999).

[39] A.V.Arefiev and B.N.Breizman, Bull. Am. Phys. Soc. **44**, 132 (1999).

[40] A.V.Arefiev and B.N.Breizman, Bull. Am. Phys. Soc. **45**, 333 (2000).

[41] A.V.Arefiev and B.N.Breizman, Bull. Am. Phys. Soc. **46**, 62 (2001).

[42] B.N.Breizman and A.V.Arefiev, Bull. Am. Phys. Soc. **46**, 62 (2001).

Vita

Alexey Arefiev was born in Alma-Ata, Kazakhstan on 12 January 1977, the son of Dr.Vladimir Arefiev and Valentina Arefieva. He received a Bachelor of Science degree in Physics from the Novosibirsk State University in 1998. In January 1999 Alexey was accepted to the University of Texas at Austin and started graduate studies.

Permanent address: 1900 Burton Dr. Apt. 159
Austin, Texas 78741

This dissertation was typeset with LaTeX[†] by the author.

[†] LaTeX is a document preparation system developed by Leslie Lamport as a special version of Donald Knuth's TeX Program.